Final Report On
(NAS8-36651)

MECHANISMS OF ROLLING CONTACT SPALLING

Prepared for

George C. Marshall Space Flight Center
Alabama, 35812

By

A. M. Kumar, S. M. Kulkarni, V. Bhargava,
G. T. Hahn and C. A. Rubin

CENTER FOR MATERIALS TRIBOLOGY
P. O. Box 1592, Station B
Vanderbilt University
Nashville, TN 37235

May 30, 1987

TABLE OF CONTENTS

ABSTRACT

This report describes the results of a 15-month study aimed at analyzing the mechanical-material-interactions responsible for rolling contact spalling of the 440C steel, high pressure oxygen turbopump (HPOTP) bearings. A coupled temperature-displacement finite element analysis of the effects of frictional heating under the contact is presented. The contact is modelled as a stationary, heat generating, 2-dimensional indent in an elastic-perfectly-plastic half-space with heat fluxes up to $8.6 \cdot 10^4$ KW/m^2 comparable to those generated in the bearing. Local temperatures in excess of 1000°C are treated. The calculations reveal high levels of residual tension after the contact is unloaded and cools. Efforts to promote Mode II/Mode III fatigue crack growth under cyclic torsion in hardened 440C steel are described. Spalls produced on 440C steel by a 3 ball/rod rolling contact testing machine were studied with scanning microscopy. The classical, V-shaped spalls form with a loose flap that breaks off periodically. Surface initiation and subsurface initiation of the spalls is encountered in uncoated and copper coated samples, respectively.

The shapes of the cyclic, stress-strain hysteresis loops displayed by hardened 440C steel in cyclic torsion at room temperature are defined for the plastic strain amplitudes encountered in rolling/sliding contact. The loop shapes and behavior are well represented by the elastic-linear-kinematic hardening-plastic (ELKP), idealization. Finally, elasto-plastic finite element analyses of repeated, 2-dimensional rolling-plus-sliding contact embodying the ELKP-properties of 440C is presented. The analyses treat Hertzian pressures in the range p_o = 2.5 GPa, to p_o = 3.64 GPa and full slip with a friction coefficient μ = 0.2 in the absence of local heating. The rim distortion, cyclic plastic strains, residual stresses, and plastic energy dissipation are evaluated and compared with results for pure rolling and perfect plasticity.

1. INTRODUCTION

The service life of the HPOTP (high pressure oxygen turbopump) bearings is limited by premature spalling of the bearing races and balls. These bearings operate at 28,000 rpm and nominal load of 7100 N, and are intended to survive for 27,000s with lubrication provided by MoS_2 films and liquid oxygen cooling[1-3]. These conditions can produce high heat generation rates in the range 60 KW to 130 KW[2] with inadequate lubrication and loss of clearances. Consistant with this, evidence of bearing surface temperatures reaching 500°C-1000°C have been reported[2,4]. While the predicted life of the bearings is 360,000s with full film lubrication, severe spalling and prominent wear are reported after 1090s at full power[1]. The spalls are largely surface initiated, proceed in both balls and races, and propagate inwards at relatively small angles. Subsurface damage in inner races is more severe than observed on the surface.

Efforts to improve the performance of the HPOTP bearings will benefit from analyses of the thermal and mechanical contact stresses and the attending plastic deformation and spalling generated under operating conditions. Such analyses have been intractible in the past, but are now within reach. The present authors have developed elasto-plastic finite element analyses of repeated rolling and sliding contact embodying realistic constitutive relations[5-10]. They have also extended fracture mechanics methods to the rolling contact spalling problem[11-13]. This report describes the results of a 15-month study aimed at applying these capabilities to the HPTOP bearing problem.

2. SUMMARY

2.1 Objectives

The general objective of the research was to analyze the mechanical-material interactions responsible for rolling contact spalling with the aim of identifying ways of improving the performance of 440C steel HPOTP bearings.

2.2 Tasks

Task 1. Frictional Heating. Previous analyses of the frictional heating of the HPOTP bearing were reviewed. A coupled temperature-displacement, elastic-plastic finite element analysis of the effects of frictional heating under the contact was performed. The contact is modeled as a stationary, heat generating, 2-dimensional indent in an elastic-perfectly-plastic half-space, with heat fluxes as high as $8.6 \cdot 10^4$ KW/m^2 which correspond with the heat generation by the HPOTP bearing, and a film coefficient selected to produce temperatures in excess of 1000°C. The calculations reveal that the local heating produces high levels of residual tension: $\sigma^R_x \approx 350$ MPa, $\sigma^R_z \approx 1200$ MPa, after the contact is unloaded and cooled. The superposition of compression by the translating contact can then produce a fluctuating tension and a potential Mode I crack driving force that can promote crack initiation and crack growth.

Task 2. Spall Initiation and Cyclic Crack Growth. Efforts have been made to promote Mode II/Mode III fatigue crack growth in torsion test samples as a first step in evaluating the Mode II and Mode III cyclic crack growth resistance (i.e., da/dN vs ΔK_{II} curve). Test bars of the hardened 440C steel with circumferential defects were subjected to cyclic torsion with progressively increasing stress amplitudes. In all cases, cracks emerging from the defects extended in directions that produce Mode I loading. This is attributed to a

low Mode I resistance relative to those for Mode II and Mode III growth. This problem requires further work.

Spalls and wear tracks produced with a 3 ball/rod rolling contact testing machine were studied with scanning microscopy. Both the uncoated and copper coated hardened 440C steel rods displayed the classical V-shaped spalls. The spalls form with a loose flap that breaks off periodically. It appears that the spalls in the uncoated samples initiate at the running surface, at surface imperfections, while the spalls in the coated samples initiate below the surface. It is not clear whether the copper coated samples possessed better quality surfaces to begin with or whether the copper coating rendered the surface defects less harmful.

Task 3. Cyclic Flow Properties of 440C Steel. The shapes of the cyclic, stress-strain hysteresis loops displayed by hardened, HRC-59, 440C steel in cyclic torsion have been measured at room temperature and a frequency of 0.5 Hz. The constant plastic strain amplitude tests reproduced the strain amplitudes, $0.0005 < \Delta\gamma^P/2 < 0.002$, encountered in rolling/sliding contact. The loop shapes and behavior are well represented by a 3 parameter, elastic-linear-kinematic hardening-plastic (ELKP) idealization. The torsion tests show that the hardened 440C steel undergoes substantial cyclic hardening before fracturing after $N \simeq 300$ to 600 cycles. The near end of life values of the ELKP-material parameters of 440C steel: $\sigma_K = 606$ MPa, and $M = 188$ GPa, are similar to those obtained for other hardened bearing steels and are useful approximations of the properties that govern mechanical response to repeated rolling-sliding contact at room temperature.

Task 4. Elasto-Plastic Finite Element Analyses of Rolling-Plus-Sliding Contact. Elasto-plastic finite element anlayses of repeated, 2-dimensional

rolling-plus-sliding contact have been performed for the ELKP-properties of 440C steel evaluated by Task 3. The calculations treat rolling with full slip, Hertzian pressures in the range p_o = 2.5 GPA to p_o = 3.64 GPA, a tangential-to-normal-force-ratio T/N = 0.2 and a coefficient of friction μ = 0.2. The rim distortion, the cyclic plastic strains, the residual stresses, and the plastically dissipated energies are evaluated. The results show that the contacts produce peak cyclic strains and residual stresses in the range: $0.00025 \leq \Delta\bar{\varepsilon}^P/2 \leq 0.001$, and -20 MPa $\leq \sigma^R \leq -35$ MPa that are similar to the values calculated for pure rolling but much smaller than the strains and stresses calculated for rolling-plus-sliding with elastic-perfectly-plastic material behavior. The analysis locates the peak plastic strain activity at a relative depth of y/w = 0.65 (2w is the contact width) where spall initiation has been observed. In the cases treated, energy dissipated as heat by plastic deformation is from 3% to 15% of the energy dissipated at the surface by friction.

3. CYCLIC FLOW PROPERTIES OF 440C STEEL

3.1 Introduction

There is evidence from many sources that rolling contact failure -- the formation of spalls and shells -- is closely connected with cyclic plastic deformation[5]. Such failures begin to occur close to the "shakedown" value of the Hertzian relative peak contact pressure beyond which repeated contacts produce continuing cyclic plasticity*. The material's resistance to cyclic

---

*The shakedown value of the relative peak pressure, p_o/k (where k is the shear yeild strength) depends on the shape of the contact ellipse and the normal-force-to-shear-traction-ratio P/N. For pure rolling, the shakedown values are p_o/k = 4 and p_o/k = 4.7 for line and circular contacts respectively. For rolling with full sliding with a friction coefficient μ = 0.2 = T/N, p_o/k = 3.2 for line contacts, or p_o = 1.9 GPa for a bearing steel (k ≃ 600 MPa).

plasticity is therefore one of several critical material properties that determine the rim's contact pressure capacity and life*.

The resistance to cyclic flow is determined by both the value of k and the characteristics of the material's stress-strain hysteresis loop[6,7]. Earlier analyses of the cyclic deformation of the rim were performed for the isotropic, elastic-perfectly-plastic (EPP) material behavior[8,9] illustrated in Figure 1(A). In this case, material subjected to repeated contacts above shakedown experiences the non-fully-reversed strain cycle shown schematically in Figure 1(B). More recently, Bhargava, Hahn and Rubin and their coworkers[6,7] have measured the hysteresis loops of 42100 bearing steel and a 1070 rail steel for the range of plastic strain amplitudes encountered in rolling contact above shakedown. They find that the cyclic behavior of these steels is anything but elastic-perfectly-plastic but tends to be kinematic[10]. They employ the bilinear, 3 parameter, elastic-linear-kinematic hardening plastic (ELKP) representation of the hysteresis loop shown in Figure 2. Finite element calculations reveal that the ELKP material experiences fully reversed strain cycles with a mean stress above shakedown [see Figure 1(C)] with much smaller strain amplitudes.

The characteristics of the hysteresis loop of hardened 440C steel have not previously been measured. Such measurements for the strain amplitudes relevant to rolling contact at room temperature are described in this section. The measurements define the ELKP-parameters of 440C steel. Elasto-plastic finite element analyses of rolling and sliding, that employ these parameters, are described in Section 6.

---

*The other properties that are important are the features of second phase particles that act as local stress raisers, the stability of the microstructure, and the resistance to crack initiation

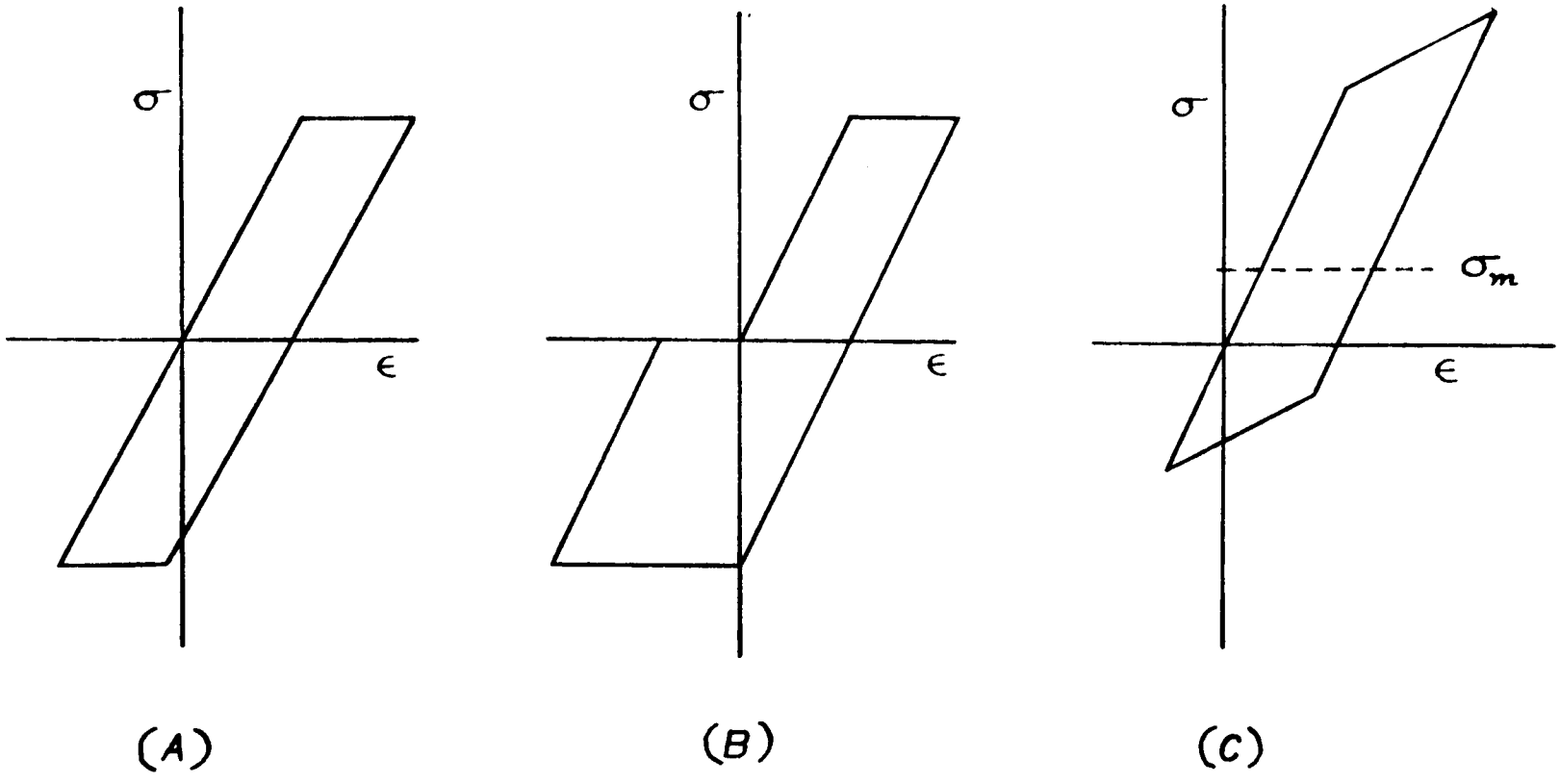

Figure 1. Schematic representation of stress-strain hysteresis loops: (A) elastic-perfectly-plastic and fully reversed; (B) elastic-perfectly-plastic and non-fully reversed; and (C) elastic-kinematic hardening plastic and fully reversed.

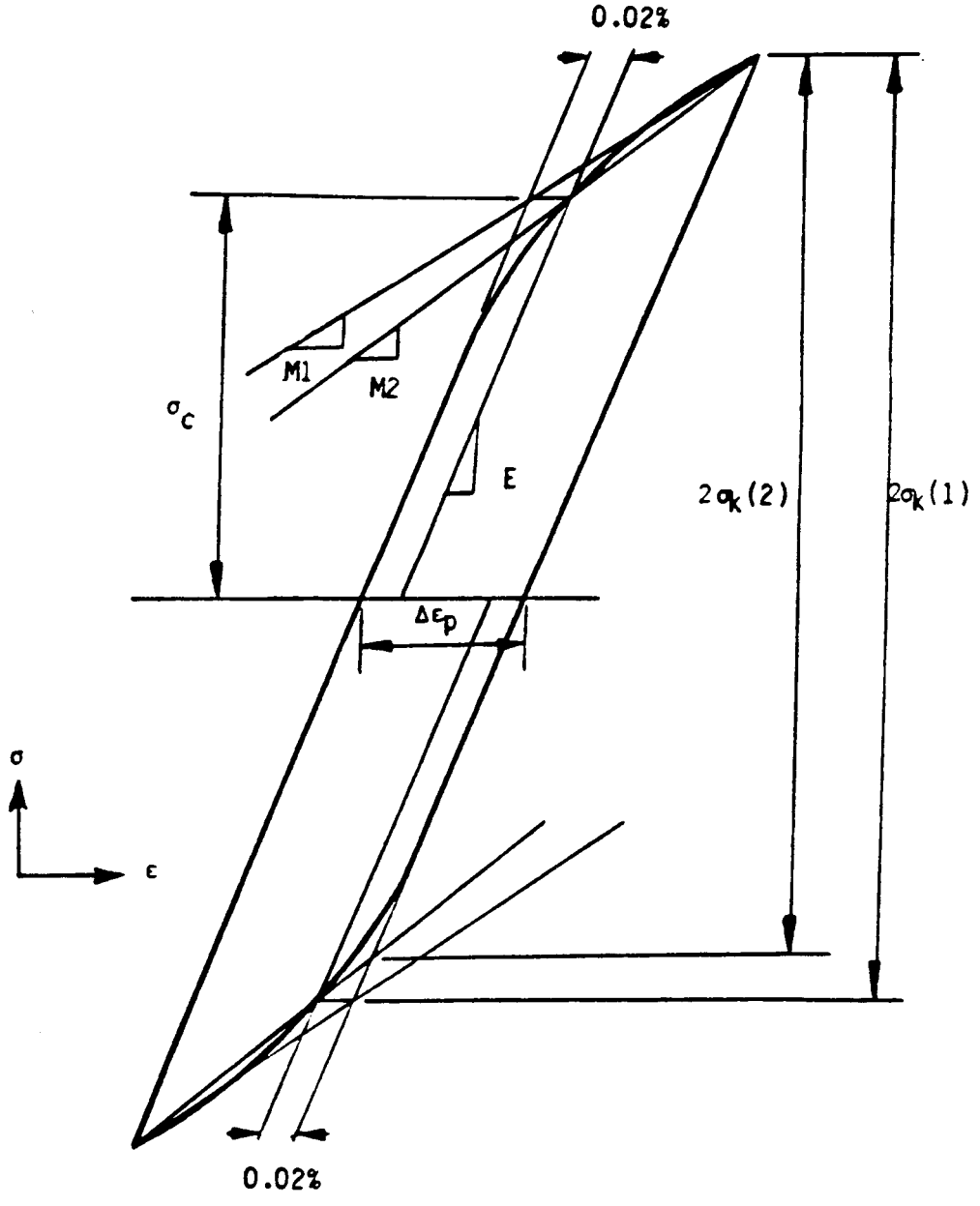

Figure 2. Schematic representation of an elastic-linear-kinematic-plastic (ELKP) hysteresis loop, indicating the terminology.

3.2 Experimental Procedures

Cyclic torsion tests have been conducted on type 440C steel which is a hardenable grade of martensitic stainless steel containing about 1% C and 18% Cr.

After machining, the specimens were given the following heat treatment:

a. Austenitize for 1 hour at 1930°F.

b. Quench in liquid nitrogen.

c. Temper at 325°F for 1 hour.

d. Air cool at 70°F.

e. Cold soak in liquid nitrogen for 30 min.

f. Temper at 325°F for 1 hour.

This produced a hardness of HRC-59. Typical microstructure of the steel after heat treatment is shown in Figures 3 and 4. The monotonic, equivalent stress-equivalent strain curve derived from a torsion test is shown in Figure 5. The monotonic yield stress values of the material are:

Offset, %	Equivalent Tensile Yield Stress, MPA (ksi)
0.02	1200 (174)
0.2	1760 (255)

Torsion Testing. Cyclic torsion tests were carried out on hollow, cylindrical specimens. The specimen dimensions, as shown in Figures 6(a) and 6(b), are not altered by the cyclic deformation. The tests were carried out at room temperature with a frequency f = 0.5 Hz on an axial-torsion, servohydraulic testing machine. The stress amplitude and mean stress were automatically controlled and manually adjusted to maintain the desired constant plastic strain amplitudes. It was frequently difficult to control strain amplitude accurately during the first N = 25 cycles because of the rapid cyclic hardening, but it presented no problems during the subsequent cyclic life.

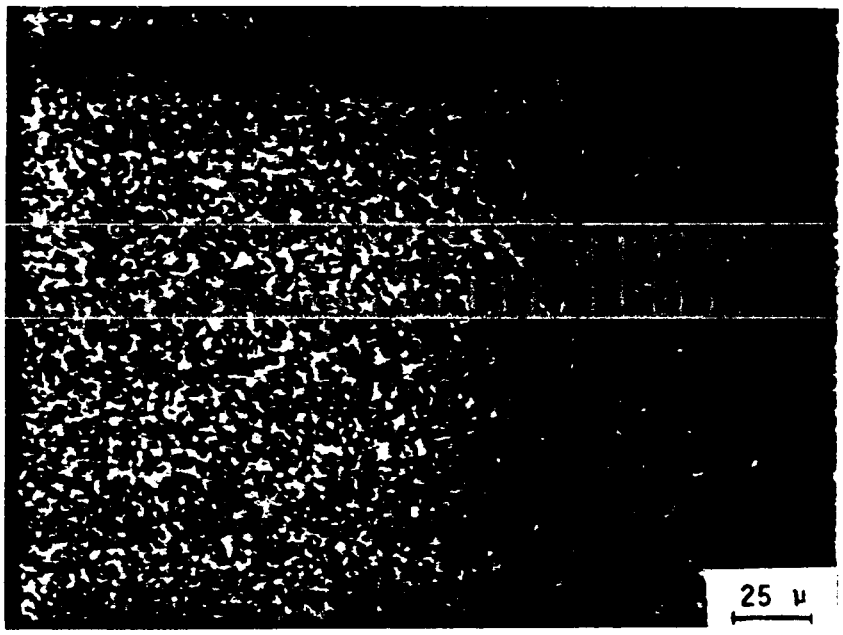

Figure 3. Microstructure of 440C steel after heat-treatment.

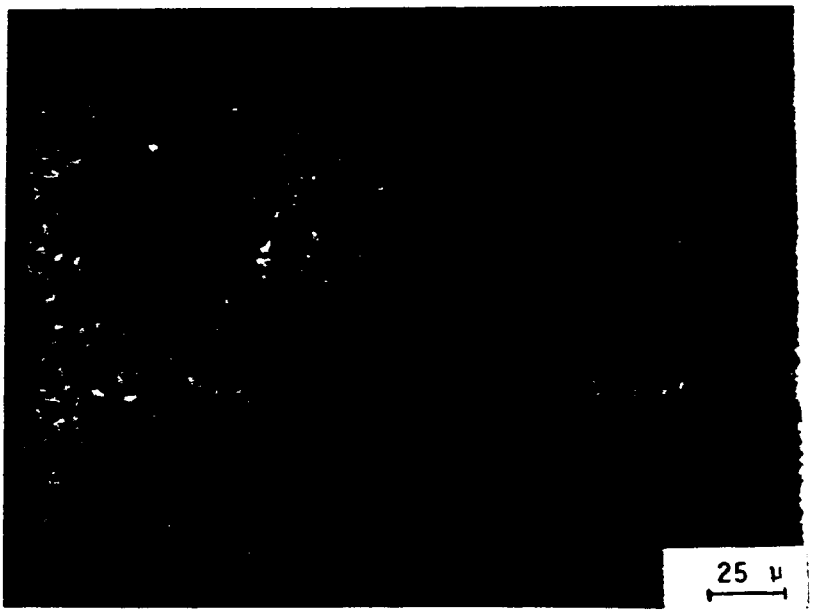

Figure 4. Microstructure of 440C steel showing some inclusions.

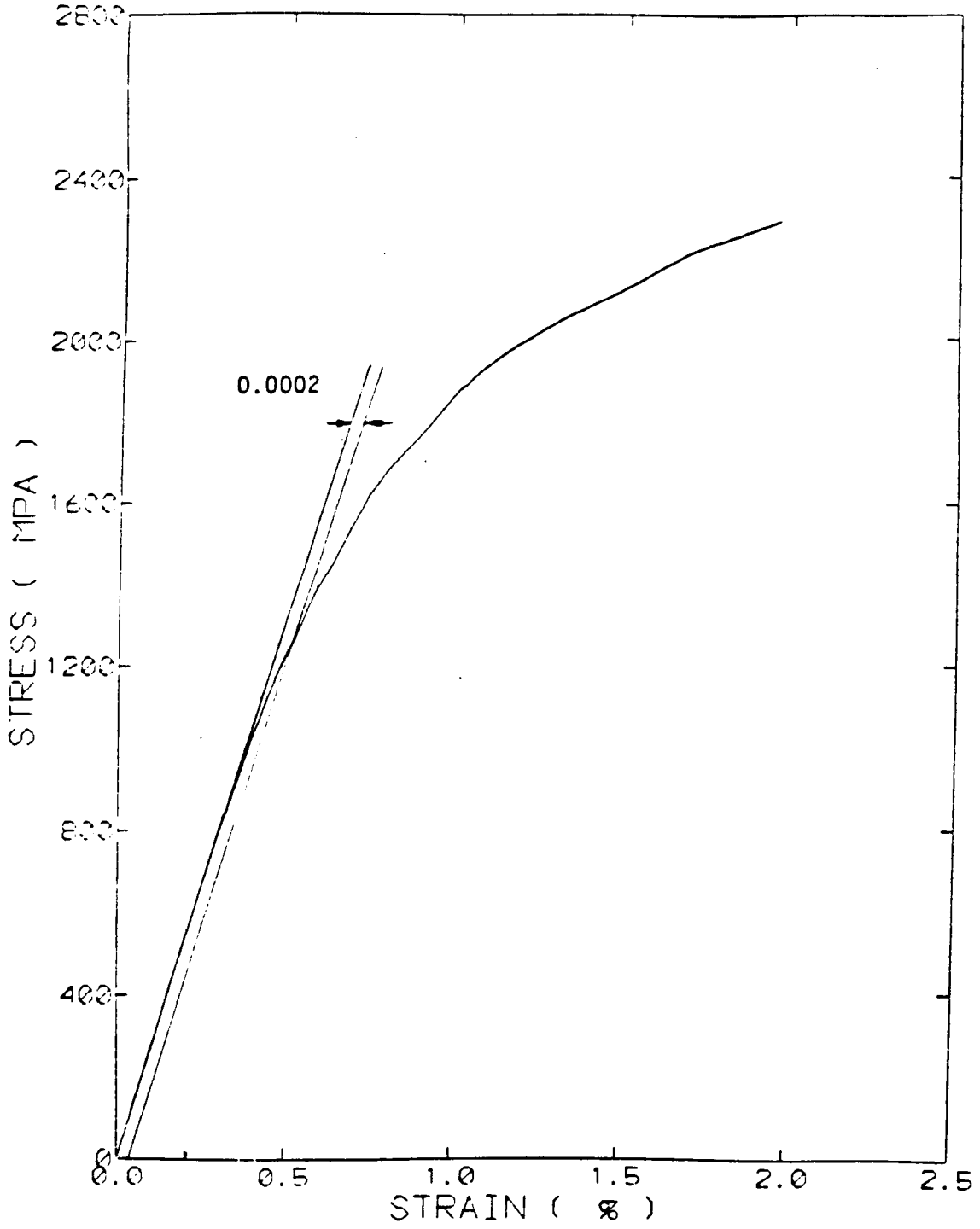

Figure 5. Monotonic equivalent stress-strain curve for 440C showing 0.02% offset. The curve is derived from a torsion test.

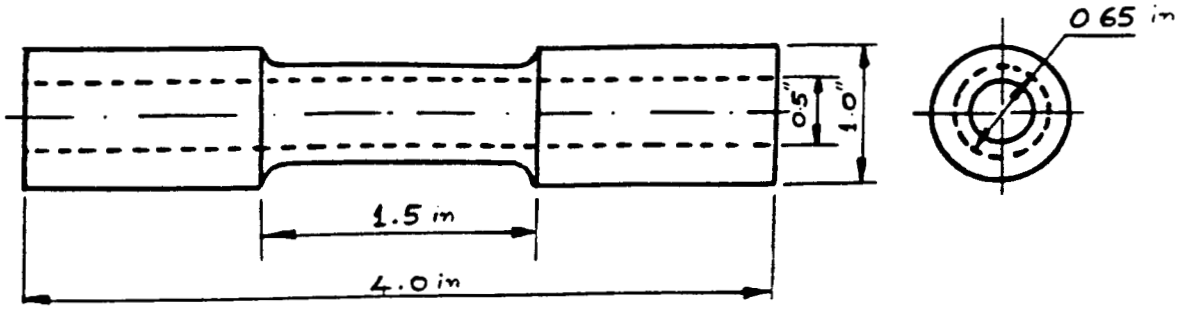

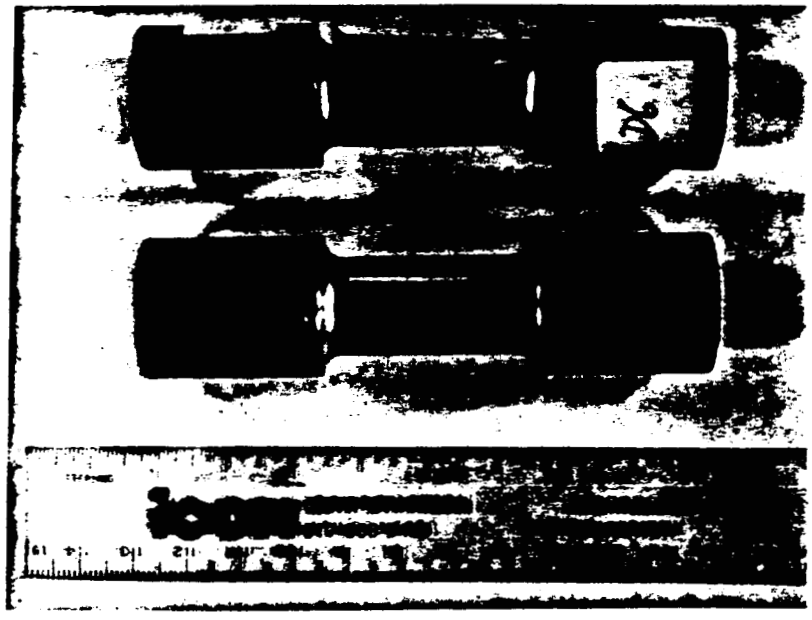

Figure 6. (a) Torsion test specimen dimensions. (b) Specimen geometry before and after the test.

The first cycle was recorded with manual load control at about f= 0.1 Hz to define the elastic loading (and unloading) line. Subsequent cycles were performed at f= 0.5 Hz, and the torque-rotation loop was recorded with a data acquisition computer. The computer first installs the elastic shear stress-strain lines. It then converts 400 separate sets of torque and rotation values in each cycle to shear stress-strain values consistent with an elastic slope of G = 79.6 GPa; and plots the loop (see Figure 7). The system then determines the 0.035% shear strain offset (0.02% equivalent strain offset), shear yield strength (horizontal marks) and other 2 ELKP parameters described in Figure 2, and their tensile equivalents :

(i) k_K and $\sigma_K = \sqrt{3}\, k_K$, the kinematic shear and tension yield strength, and

(ii) M_s and $M = 3\, M_s$, the plastic shear and tension modulus (linear strain hardening coefficients).

Two alternative ways of defining the parameters: $\sigma_K(1)$, M1 and $\sigma_K(2)$, M2, illustrated in Figure 2, were examined. In addition the system automatically computes U, the loop area, which represents the plastic work per unit volume and corresponds closely with heat evolution. The values of U are compared with $U' = 2\Delta\bar{\varepsilon}^P \sigma_K$, the area of the ELKP-loop.

3.3 Results

Examples of the hysteresis loops displayed by the 440C steel samples are reproduced in Figure 8. After the first few strain cycles the departures from linear elastic behavior are observed at very modest stresses. The

* A more accurate analysis of the torque-rotation values that accounts for the plastic contribution of the fillet regions was devised after this work was completed. This analysis leads to ~50% larger plastic strain range values and ~20% lower stress values and ~4% lower M-values than reported here. The revised results will be presented in a paper currently in preparation.

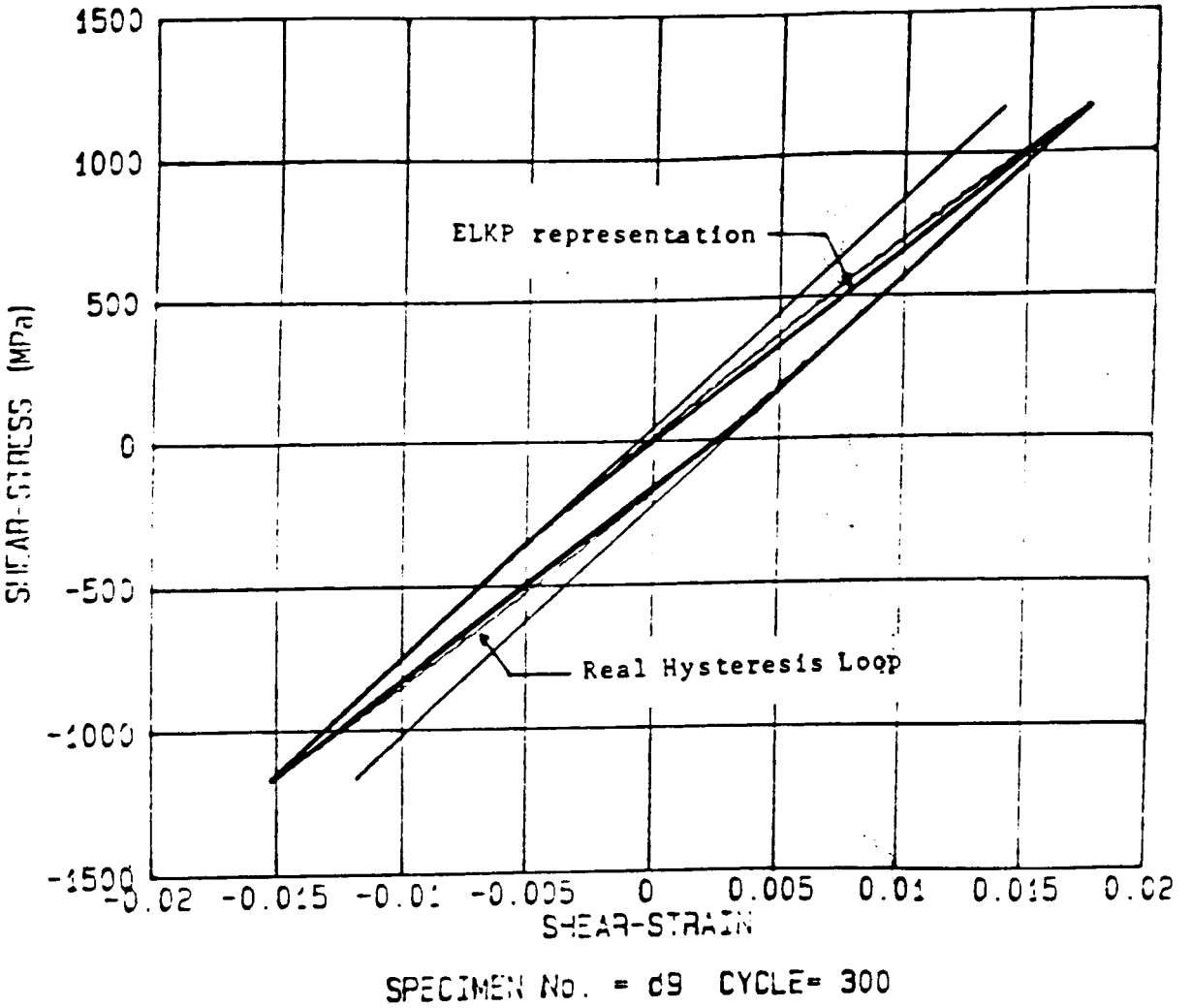

Figure 7. An elastic-linear-kinematic-hardening-plastic representation of a real 440C stress-strain loop indicating the terminology.

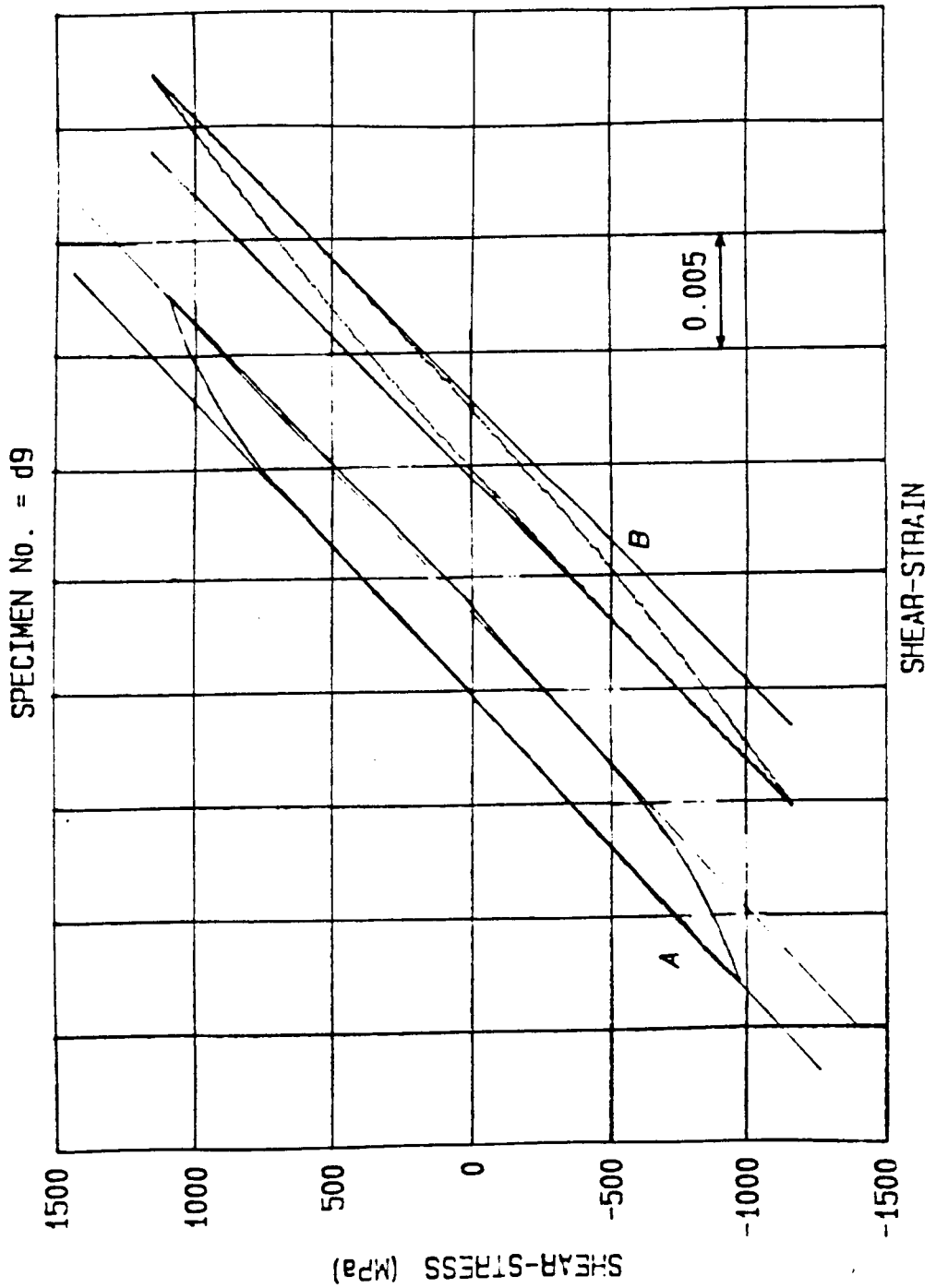

Figure 8(d). Hysteresis loops displayed by the 440C steel specimen d9. The loops A and B represent initial and the steady state loops (N = 1 and N = 250), respectively.

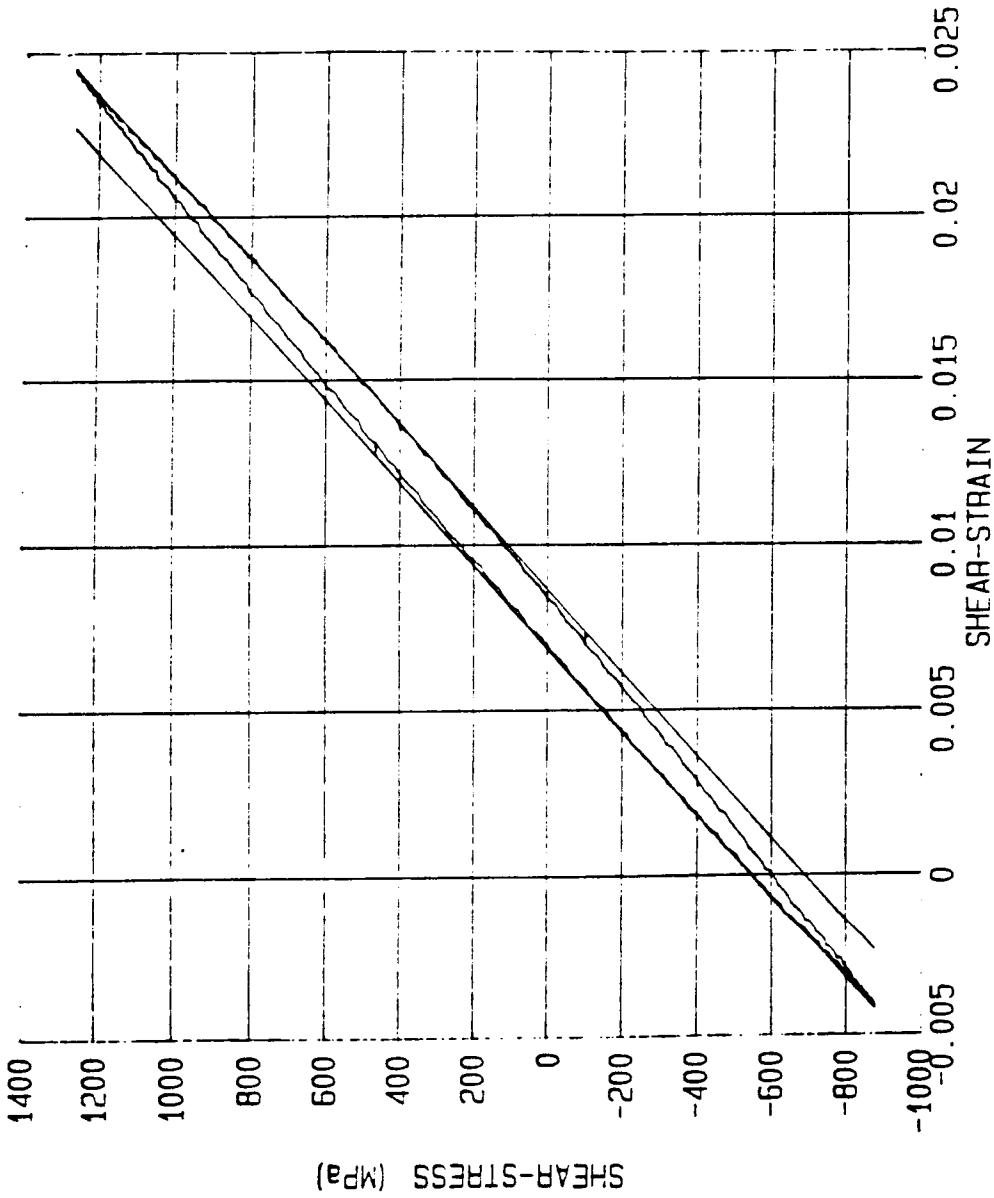

Figure 8(b). Steady state hysteresis loop recorded for specimen d10. A mean shear stress of 200 MPa was imposed during the test and correspondingly, there is an upward shift in the loop.

ensuing non-linear plastic deformation is accompanied by rapid hardening. The departure from elastic deformation occurs at negative stresses for the $\Delta\varepsilon^P$ = 0.002 strain range and for the $\Delta\varepsilon^P$ = 0.001 strain range sample with a 200 MPa mean stress; i.e., plastic compression is obtained even before the stress reversal while the stress is tensile [see Figure 8(b)]. The nonreversibility of the strain cycle produced by the 200 MPa mean stress rapidly decays (see Figure 9). All of these features are symptomatic of the kinematic hardening behavior. Figure 10 illustrates that the loop areas defined by the 2 ELKP-idealizations agree very well with the actual loop areas for small values of strain range. The $\sigma_K(2)$, M2 characterization appears to be slightly better at the highest strain.

The variation of the loop parameters σ_K, σ_c, σ_a and M are shown in Figures 11-13. The samples displayed noticeable cyclic hardening throughout their relatively modest lives: 300 cycles $\leq$ N $\leq$ 600 cycles. Both σ_c, σ_K and σ_a increase with N, while the plastic modulus remains more or less constant. Consequently, the steady state is not well defined by these measurements. The near end of life values summarized in Table 1 come closest to describing the ELKP properties for even larger numbers of contacts. The variation of the cyclic life with strain amplitude is presented logarithmically in Figure 14 and is approximated by the following Coffin-Manson type expression

$$N = A\ (\Delta\varepsilon^P/2)^n \qquad (1)$$

where A = 0.52 and n = -0.853. Figure 15 illustrates that the ELKP parameters σ_K and M are relatively insensitive to variations of strain amplitude and mean stress, while the conventional yield parameter measured from zero stress, σ_c, is a sensitive function of these variables.

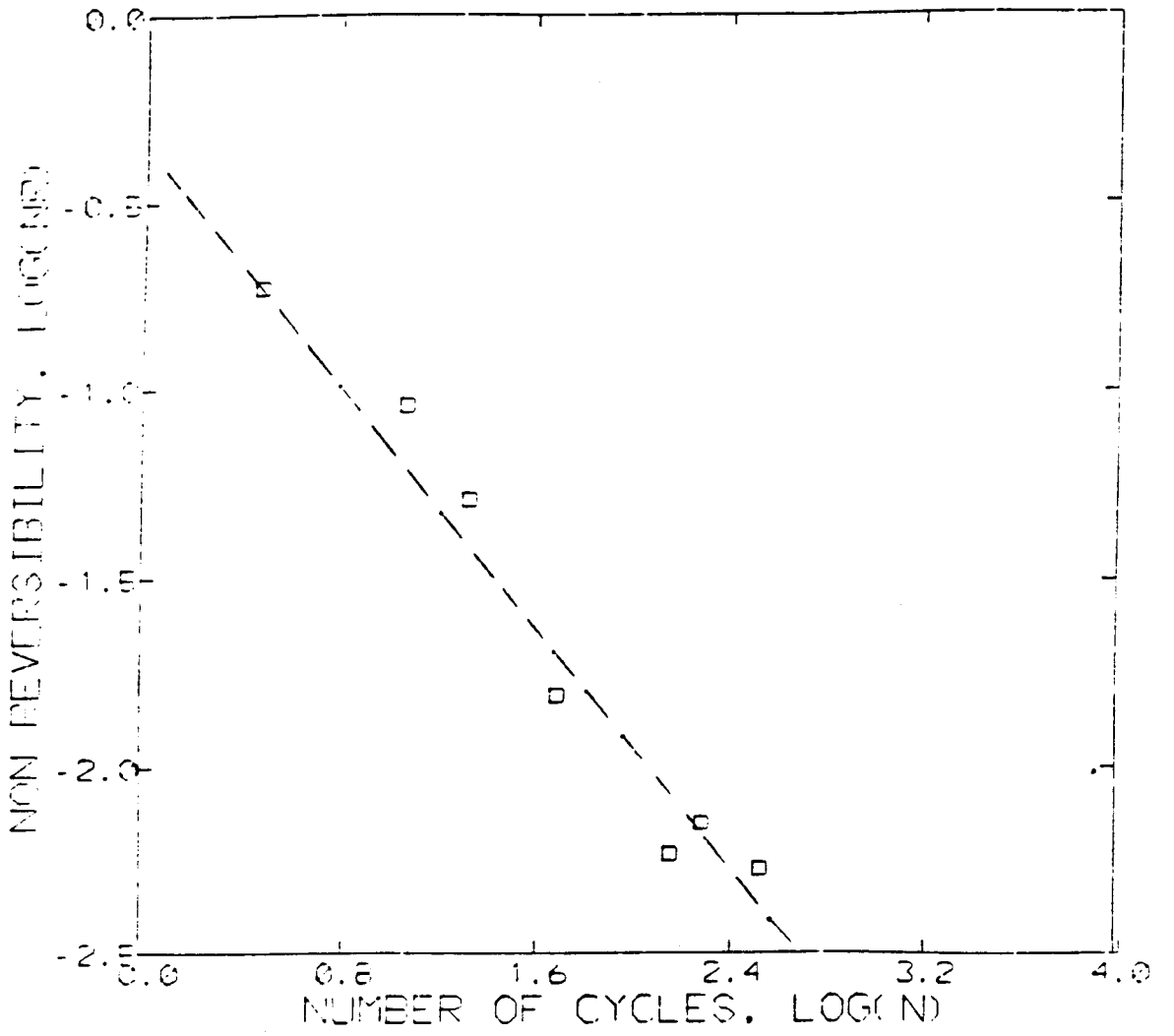

Figure 9. The exponential decay of non-reversibility with number of cycles (with an imposed mean stress of 200 MPa in shear).

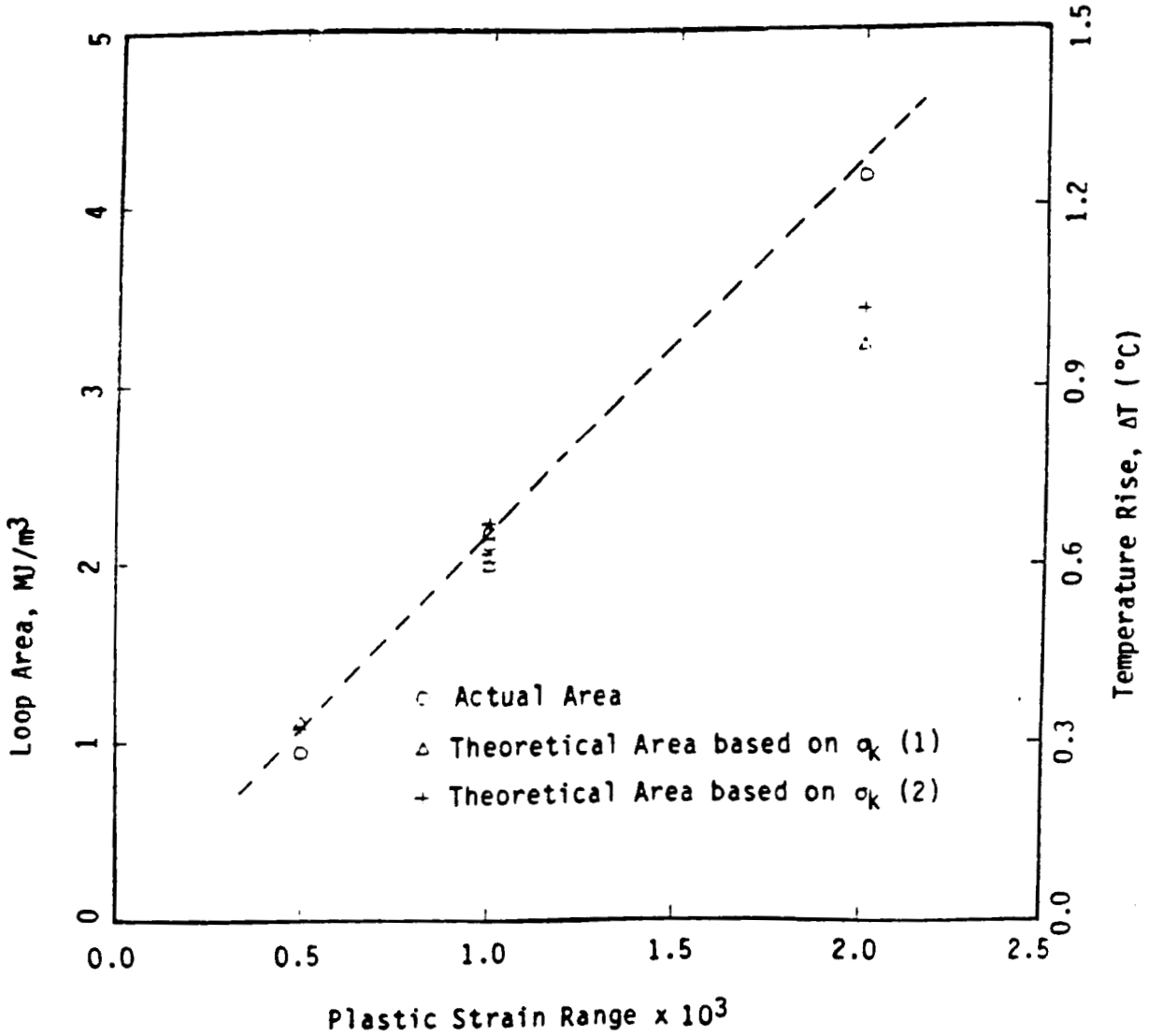

Figure 10. Comparison of the actual area of the hysteresis loops with the areas calculated based on $\sigma_k(1)$ and $\sigma_k(2)$, as a function of plastic strain range.

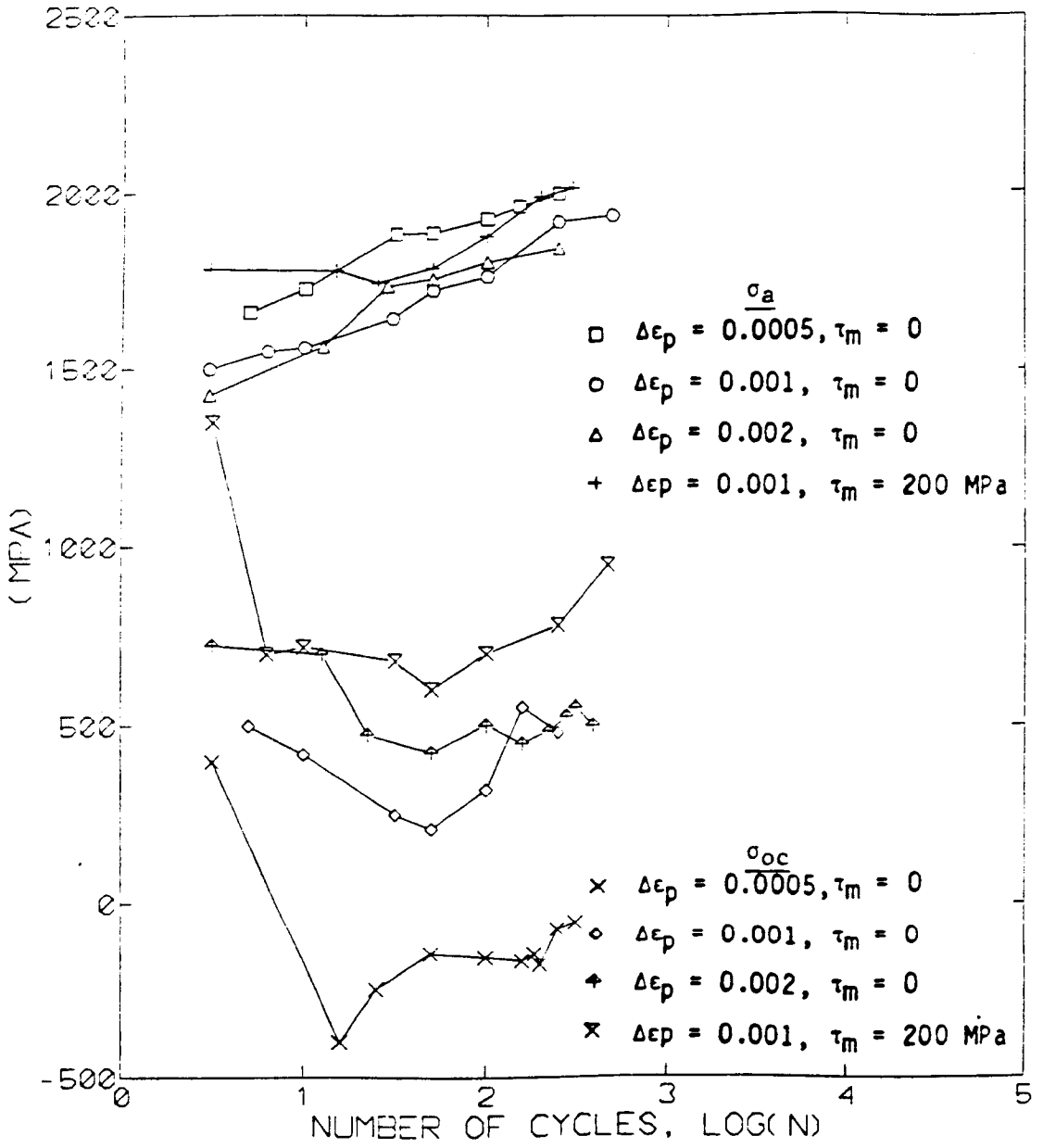

Figure 11. Variation of cyclic yield stress, σ_{oc} (0.02%) and stress amplitude, σ_a, with number of cycles.

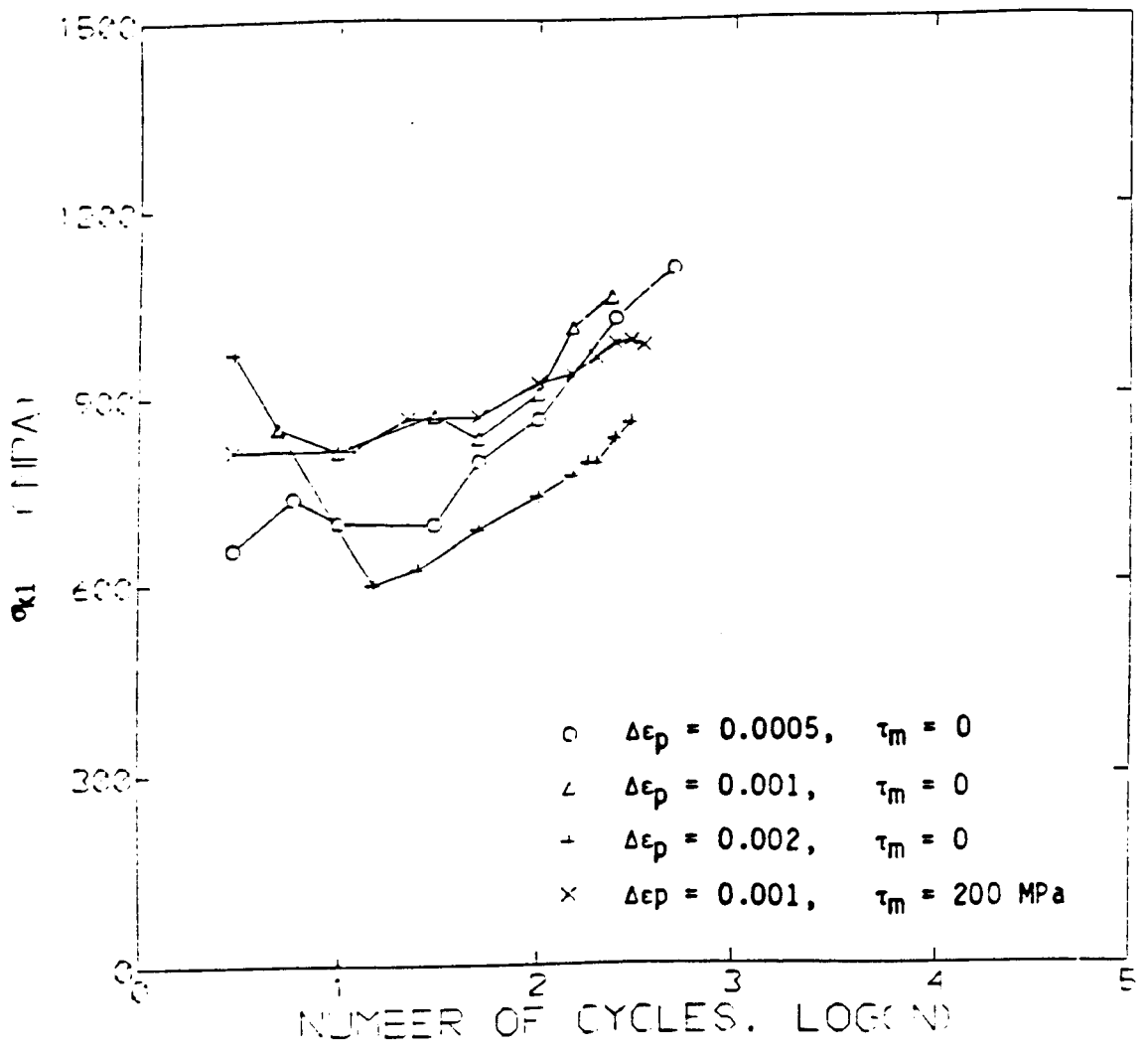

Figure 12. Variation of kinematic yield parameter, σ_{k1} with number of cycles.

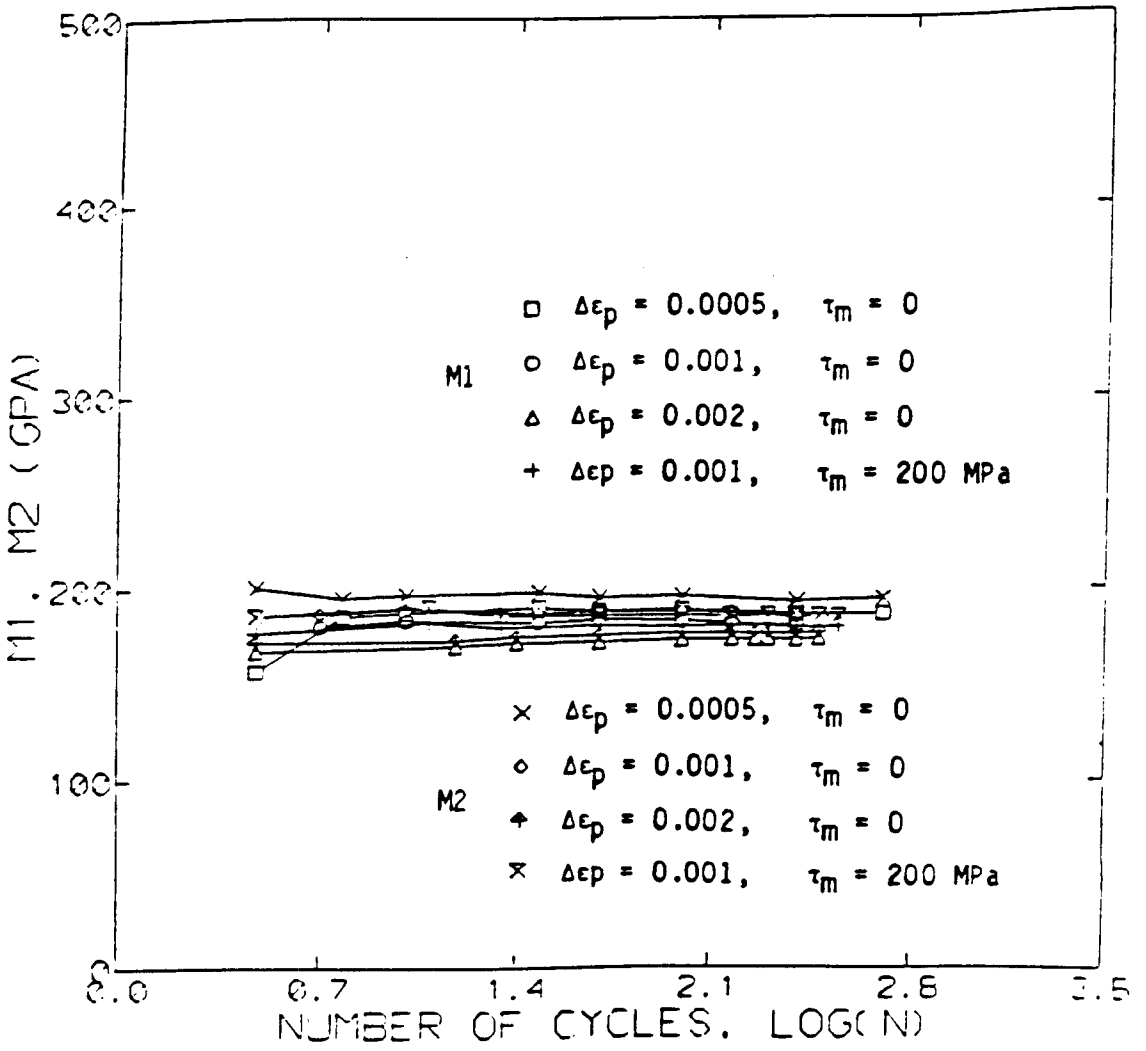

Figure 13. Variation of the plastic modulus parameters, M1 and M2, with number of cycles.

TABLE 1

END-OF-LIFE VALUES OF σ_c, σ_K, σ_a and M

Specimen ID	$\Delta\varepsilon_p$	τ_m (MPa)	N_F*	N**	σ_c (MPa)	$\sigma_K(1)$ (MPa)	$\sigma_K(2)$ (MPa)	σ_a (MPa)	M_1 (MPa)	M_2 (MPa)
D7	0.0005	0	608	500	924	1130	1082	1940	186.3	193.9
D8	0.001	0	284	250	478	1013	1103	1884	180.2	184.9
D9	0.002	0	305	250	-44	844	872	2003	172.9	176.2
D10	0.001	200	351	350	+806 -179.3	967.7	997	1844	179.4	184.8

*This is the number of cycles to failure

**This is the cycle number at which the last set of data are obtained during the test.

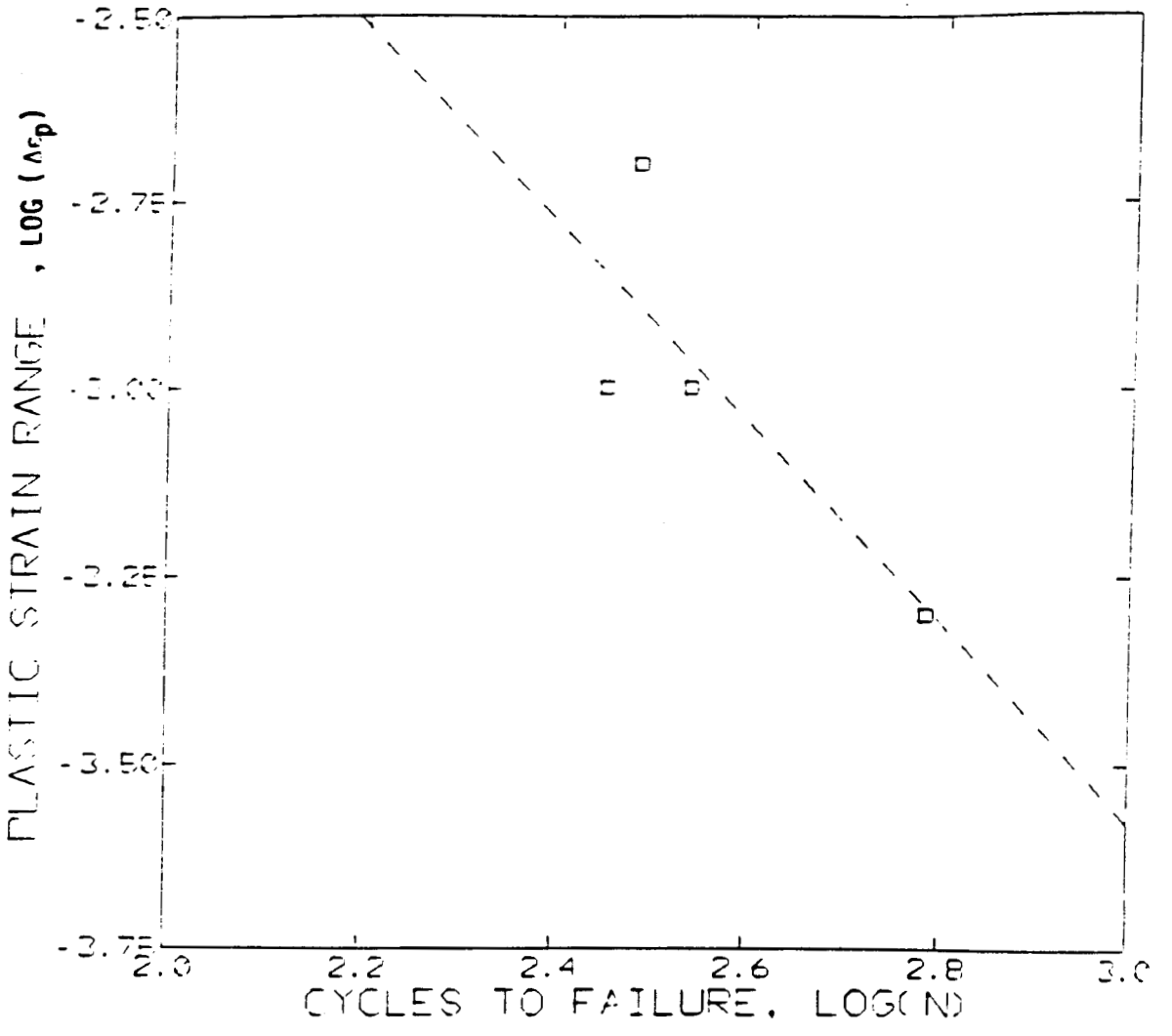

Figure 14. Variation of plastic strain range with number of cycles to failure.

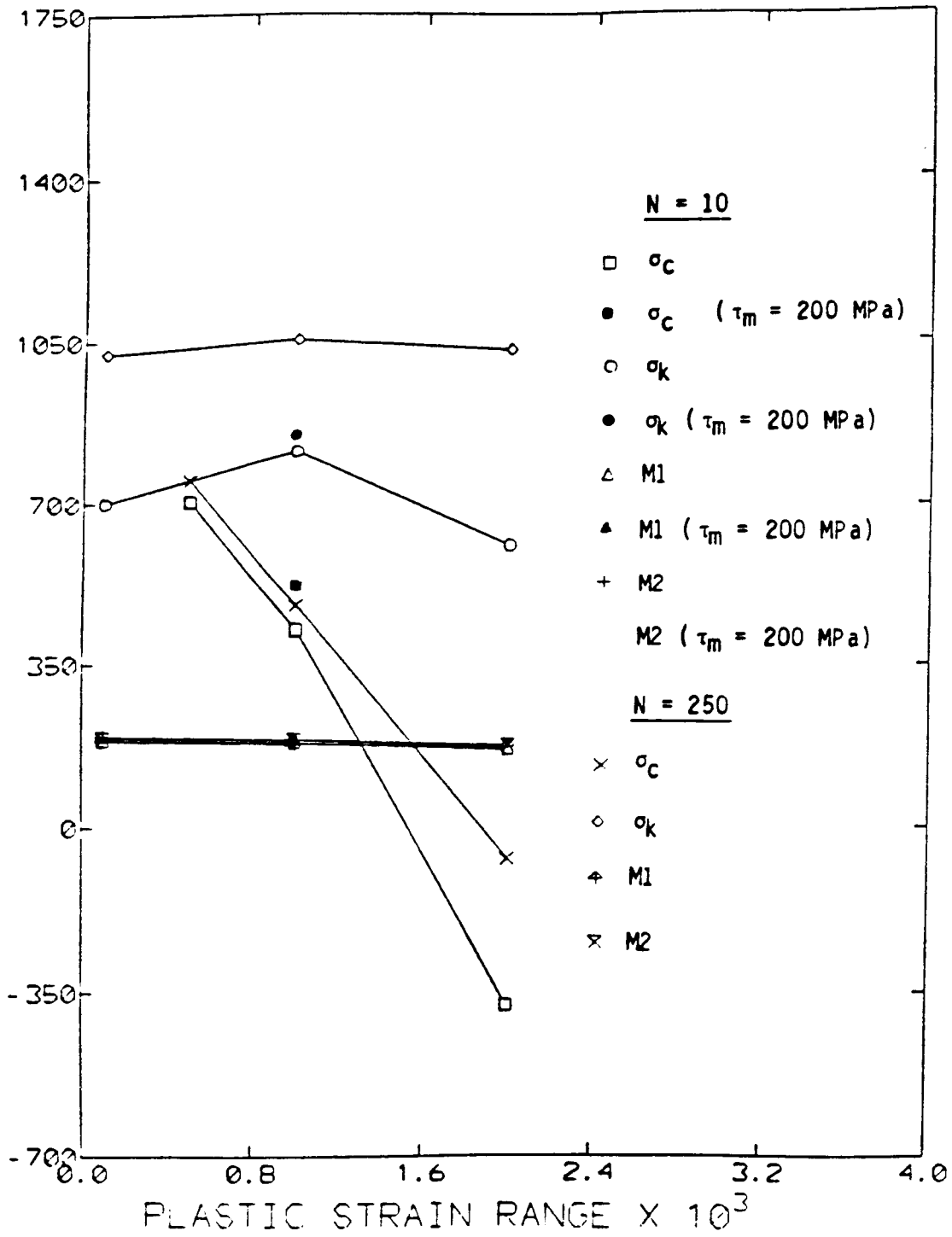

Figure 15. Variation of the cyclic parameters with plastic strain range.

4. CYCLIC CRACK GROWTH

4.1 Introduction

There is evidence that cyclic crack growth proceeds more slowly in a rim subjected to rolling contact than in other structures.*[11] As a result, the largest part of the life of the rim can reside in the crack growth stage. For example, Shao et al.[12] observed crack initiation in a case hardened rim after $N = 1.4 \cdot 10^6$ contacts. In this case, crack growth (and spall formation) proceeded in the interval $1.4 \cdot 10^6$ contacts $\leq N \leq 3.9 \cdot 10^6$ contacts, and occupied 64% of the life. In order to better understand crack growth under the contact, efforts are being made to apply fracture mechanics to this problem. This involves:

(i) Calculation of the Mode II and Mode III cyclic crack growth driving force, ΔK_{II} and ΔK_{III}[13-15].

(ii) Measurement of the Mode II and Mode III cyclic crack growth resistance; the $da/dN-\Delta K_{II}$ and $da/dN-\Delta K_{III}$ curves for the material. In the absence of these properties, the Mode I, $da/dN-\Delta K_I$ curve has been employed as a first approximation[11].

The measurements described in this section were undertaken in an effort to evaluate the $da/dN-\Delta K_{II}$ and $-\Delta K_{III}$ curves for 440C steel at room temperature.

4.2 Experimental Procedure

Crack growth tests were performed with cyclic torsion loading and the same hollow torsion samples described in Section 3 (see Figure 6). The authors have previously produced stable crack growth and fatigue striations

---

*The compressive nature of the loading and friction at the crack faces restrict the crack face sliding that is reponsible for crack growth.

in HRC 4140 steel samples of this design subject to cyclic loading (see Figure 16). In order to reduce the stress and time for initiation, first a single microhardness impression and then a cluster of impressions were placed on the surface to act as stress raisers. These specimens were subjected to large numbers of stress cycles with progressively increasing amplitudes and eventually fractured, but without signs of stable cyclic crack growth. To provide a more potent stress raiser, the sample was fitted with a circumferential, 3 mm-long, 0.5 mm deep crack-like slit introduced by spark machining. The specimen was subjected to cyclic torsion with progressively increasing shear stress amplitudes (see Table 2).

4.3 Results

The specimen fractured suddenly with no obvious signs of cyclic crack growth at an applied torque amplitude of 0.24 kN-m (2.12 kip-in) and shear stress amplitude of $\Delta\tau/2$ = 292 MPa. Crack extension proceeded at about 45° to the specimen axis (see Figure 17). Apparently, the crack preferred to grow in Mode I rather than in Mode II or Mode III. Fractographs in Figures 18-21, show signs of cyclic growth in Mode I.

Figure 18 shows the edge of the notch from which the fatigue crack started at 45° to the plane of the notch. The regions A, B and C identified in Figure 18 are magnified and shown in Figures 19, 20 and 21 respectively. Regions A and B show the typical fatigue markings which gradually change to a ductile mode away from the edge of the notch, as shown by the region C.

Figure 16. 4140 steel with Mode II/III fatigue striations.

TABLE 2

CYCLIC TORSION TEST DATA ON 440C STEEL
HOLLOW CYLINDRICAL TORSION SPECIMEN

Applied Torque Amplitude, T/2 (kN-m)	Shear Stress Amplitude, $\Delta\tau/2$ (MPa)	Estimated Applied Stress Intensity (MPa $\sqrt{m}$)	Number of Cycles
0.06	73	10	25,000
0.09	110	15	25,000
0.12	146	20	10,000
0.15	183	25	5,000
0.18	219	30	5,000
0.21	256	35	5,000
0.24	292	40	1,526

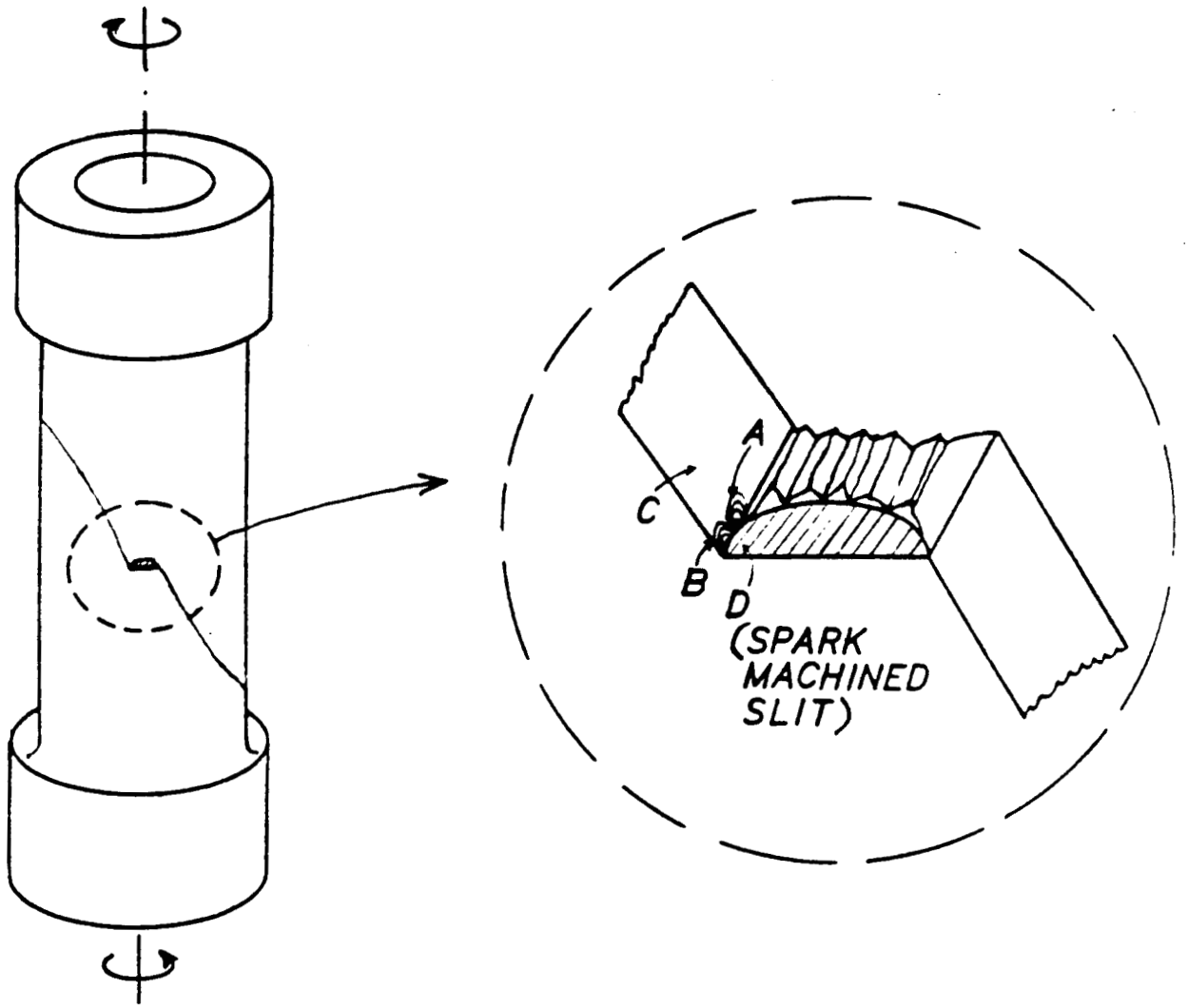

Figure 17. Schematic view of prenotched torsion specimen just after the specimen fractured. Fractographs of regions A, B, C and D identified here are presented in Figures 18 through 21.

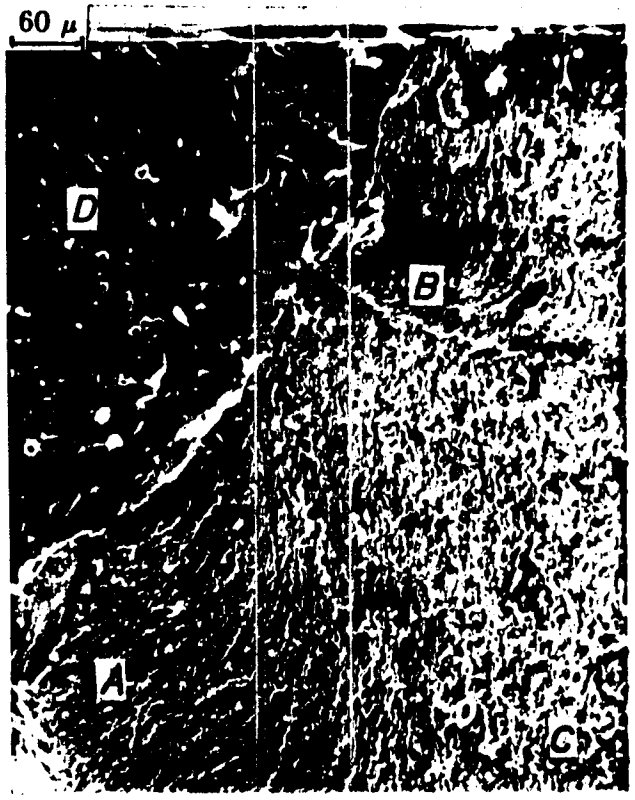

Figure 18. Fractograph of a 440C pre-notched torsion specimen showing the edge of the spark-machined notch (region D) and the fracture surface. Magnified views of Regions A, B and C are shown in Figures 19, 20, and 21, respectively.

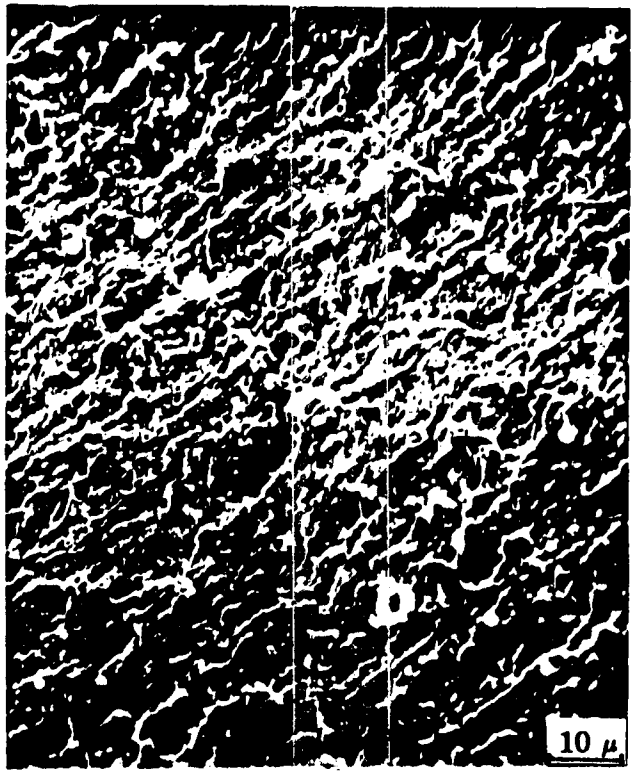

Figure 19. Magnified view of Region A (refer to Figure 18) showing fatigue marks.

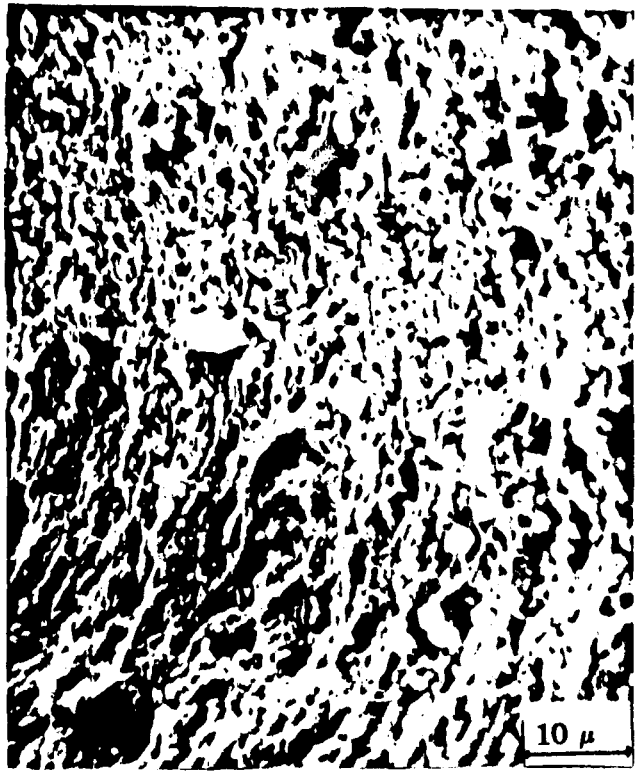

Figure 20. Magnified view of Region B (refer to Figure 18).

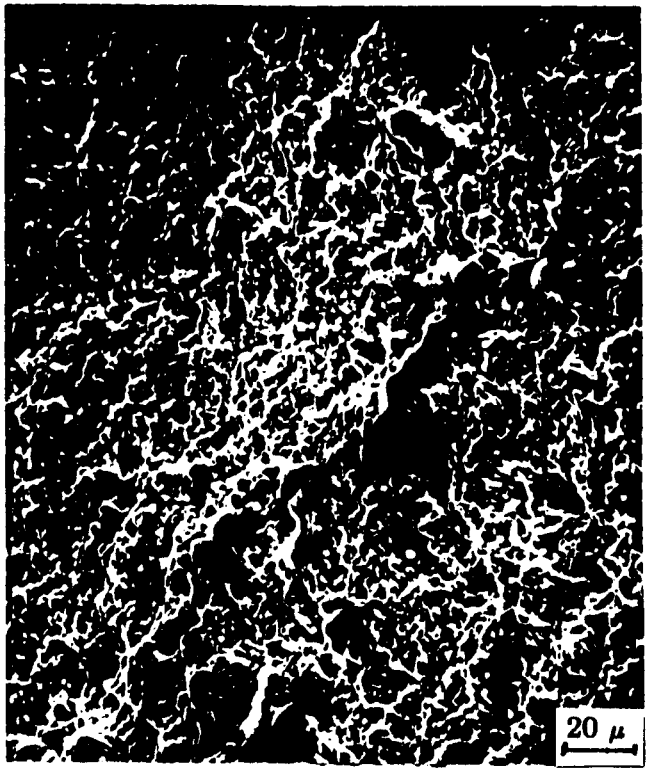

Figure 21. Magnified view of Region C (refer to Figure 18).

5. ROLLING CONTACT STUDIES

5.1 Introduction

Spalls are initiated in plastically deforming portions of the rim, usually with the involvement of second phase particles or inclusions. This occurs within a few micrometers of the running surface in the presence of surface tractions[16] (rolling-plus-sliding) or at much larger depths, e.g., 0.6w corresponding with peak cyclic strain activity, for well lubricated rolling[12,17]. The as-initiated cracks can be inclined from 20° to 30° to the running surface in the early life[12,16] or parallel to the surface (shelling) in the presence of high circumferential residual stresses that retard radial crack growth[17]. The cracks observed by Bhat and Dolan[1,2] in 440C HTOP bearings under laboratory conditions with large axial loads initiate within about 2 μm of the running surface with inclinations of from 10° to 25°. They are similar in appearance to the near surface cracks observed by Soda and Yamamoto in 1045 steel cylinders transmitting shear tractions[16]. It appears that poor lubrication and plastic deformation of the surface contribute to the spalling obtained by Bhat and Dolan. In addition, high surface temperatures, thermal stresses and attending stress fluctuations may also be important in the HPOTP environment.

This section describes direct observations of damaged 440C steel rims. The work was undertaken to learn more about the mechanisms of spalling of 440C steel under different conditions.

5.2 Experimental Procedure

Spalls produced by R. Thom of the NASA-MSFC on cylindrical 440C specimens in the 3-ball-rod rolling contact fatigue tester have been examined in the scanning electron microscope. The specimen geometry, and the design and

operation of this rolling machine have been described elsewhere[47]. Two sets of spalls were examined.

The first set was observed on a 440C test cylinder subjected to lubricated rolling contacts at a peak Hertzian pressure of 4.04 GPa (586 ksi), using roughened balls. The number of contacts to failure varied between 10^6 cycles and 10^7 cycles. The second set was observed on a test cylinder ion plated with copper to a thickness of about 0.5 μm. This specimen was tested at two contact stress levels: 4.04 GPa and 5.42 GPa. While no failures were observed for the tests carried out at a stress level of 4.04 GPa, the life varied between 30×10^6 and 65×10^6 for the tests at 5.42 GPa. Thus, the ion plated copper coating improved the life significantly. In addition, observations were made of wear tracks on larger 440C cylinders subject to rolling-plus-sliding deformation experiments produced with the Vanderbilt rolling contact machine. The rolling machine is of the cantilever type and is designed to produce rolling, sliding and combinations of rolling and sliding under different contact loads. Both line contact (2-D) and point contact (3-D) can be simulated depending on the geometries of the test specimen and the contacting roller. The design and the operation of the machine are described in reference 48. The contacting roller is made of heat treated 52100 bearing steel (HRC 62.5) and possesses a double curvature radii of 51 mm and 18.26 mm, such that it produces a circular contact patch when in contact with a cylindrical radius of 57 mm. The 440C test cylinders were 57 mm in diameter and 25 mm wide. A contact force of 2344 N was applied during the test, which converts to a Hertzian pressure of 2600 MPa and a relative peak pressure: p_o/k_k of 4.2. Two tests were conducted at this contact pressure of 2600 MPa and a relative slip of 2%. Total number of contacts for the two tests was 15,500, each under fully lubricated and unlubricated conditions, respectively. Surface

damage after the unlubricated test was very severe, while there was very little damage after the lubricated test. A photomicrograph of the specimen after the unlubricated test is shown in Figure 22(A). A magnified veiw of the wear track is shown in Figure 22(B), which shows microcracks on the surface that may eventually lead to a spall.

5.2 Results

Both the uncoated and copper coated 440C samples displayed classical, V-shaped spalls that probably originate near the surface close to the V-apex (see Figures 23-29). The dimensions of the spalls are typically: 0.3 mm - 0.6 mm in the rolling direction and 0.6 mm transverse to the rolling direction, with the latter corresponding to 2U, the diameter of the elliptical contact* and wear track. The depths of the spall craters were not determined but appear to be a small fraction of the other dimensions. The spalls display the following features, which are shown schematically in Figure 23.

(i) The V-apex [see Figure 23(A)] points in the rolling (forward) direction.

(ii) The cracks grow laterally and circumferentially on a surface making a small angle to the running surface. Thus the cracks grow deeper as it extends in the direction opposite to the rolling direction.

(iii) At an early stage, the crack breaks through to the surface at the shallow end, producing a cantilevered flap supported

---

*The following are the dimensions of the Hertzian contact ellipse produced in the 3 ball/rod tester, where 2U and 2w are the diameters of the ellipse in the transverse and rolling direction respectively:

p_o,GPa	2U,mm	2w,mm
4.04	0.6	0.34
5.42	0.8	0.46

(A)

(B)

Figure 22. 440C stainless steel specimen subjected to rolling-plus-sliding experiments in the Vanderbilt rolling contact machine: (A) photograph of the specimen showing wear tracks; and (B) magnified view of the wear track.

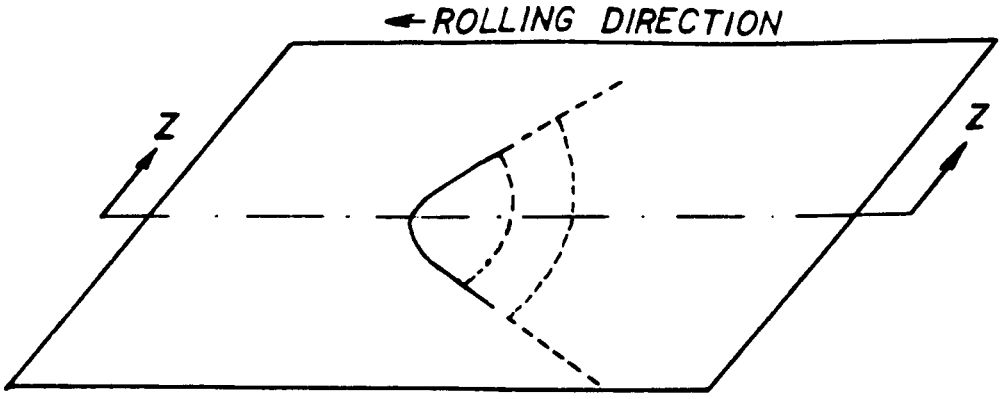

(A)

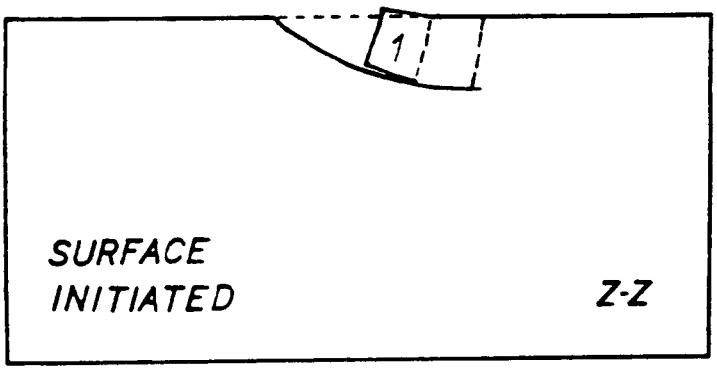

(B)

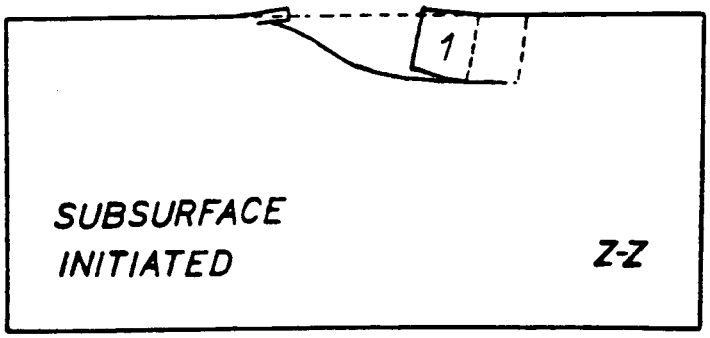

(C)

Figure 23. Schematic diagram of a V-shaped spall: (A) V-shaped apex on the surface of the wear track; (B) longitudinal section Z-Z of the wear track illustrating a surface initiated spall; and (C) a similar section illustrating a subsurface initiated spall. A cantilevered flap on the "deeper" side is identified as region 1 in (B) and (C).

by unbroken material on the "deeper" side. Such a flap will exist from the very beginning for cracks initiating at the surface [see Figure 24(A)].

(iv) Portions of the flap behind the crack front break off periodically producing wear fragments. Additional fragments are produced as more unsupported flap forms and breaks off behind the growing crack.

The loose flaps or flap stubs at the deeper end of the spall are evident in virtually all of the spalls of the uncoated and coated specimens (see Figures 24(A), 24(B), 25(A), 28 and 29). Two differences are noticeable. The spall surfaces of the uncoated samples are flat and continuous (though not necessarily smooth) at the V-apex where they reach the surface. Other surface imperfections are frequently visible near this location. In contrast the spalls of the coated samples are discontinuous close to the apex, revealing undercutting, i.e., a flap stub. In these cases, surface defects were not in evidence near the spall apex. The implication is that the spalls in the uncoated samples initiate at the running surface, at surface imperfections, while the spalls in the coated samples initiate below the surface and tend to grow parallel to the rim as they approach the running surface.

Scanning electron micrographs of the running surface produced by lubricated and unlubricated rolling and sliding are reproduced in Figures 30 and 31. The surface of the specimens was artifically damaged by means of Rockwell C hardness impressions. Figure 30 shows a hardness impression after the lubricated test. In the case of the unlubricated test (N = 15,500), the surface damage was very severe and the "ploughing" was deep enough to completely erase the hardness impressions. As shown in Figure 31, the wear track on the specimen after the unlubricated test show early signs of "V-shaped" features which could eventually lead to the formation of flakes.

(A) (B) (C)

Figure 24. Examples of spalls produced on the surface of 440C steel rods subjected to repeated rolling contact at p_o = 4.04 GPa. The micrographs display the cantilevered flap (1) produced by the subsurface crack which breaks off periodically: (A) N = 2.2 x 10^6; (B) N = 6 x 10^6; and (C) N = 4.8 x 10^6.

(B)

(A)

Figure 25. (A) Spall produced after N = 3.2 x 10^6 contacts. (B) Magnified view of Region 1.

(A)

(B)

Figure 26. (A) Spall produced after N = 6 x 10^6 contacts. (B) Magnified view of Region 2.

Figure 27. (A) Spall produced after N = 5.7 x 10^6 contacts. (B) Magnified view of Region 4 showing a secondary initiation site.

(a)

Rolling Direction

(b)

Figure 28. Characteristic "V"-shaped spall of a copper coated cylindrical specimen subjected to a Hertzian pressure p_o = 5.42 GPa and N = $6.5 \cdot 10^7$ repeated contacts: (a) spall, and (b) higher magnified view of region 1 in (a) showing this to be undercut, cantilevered flap.

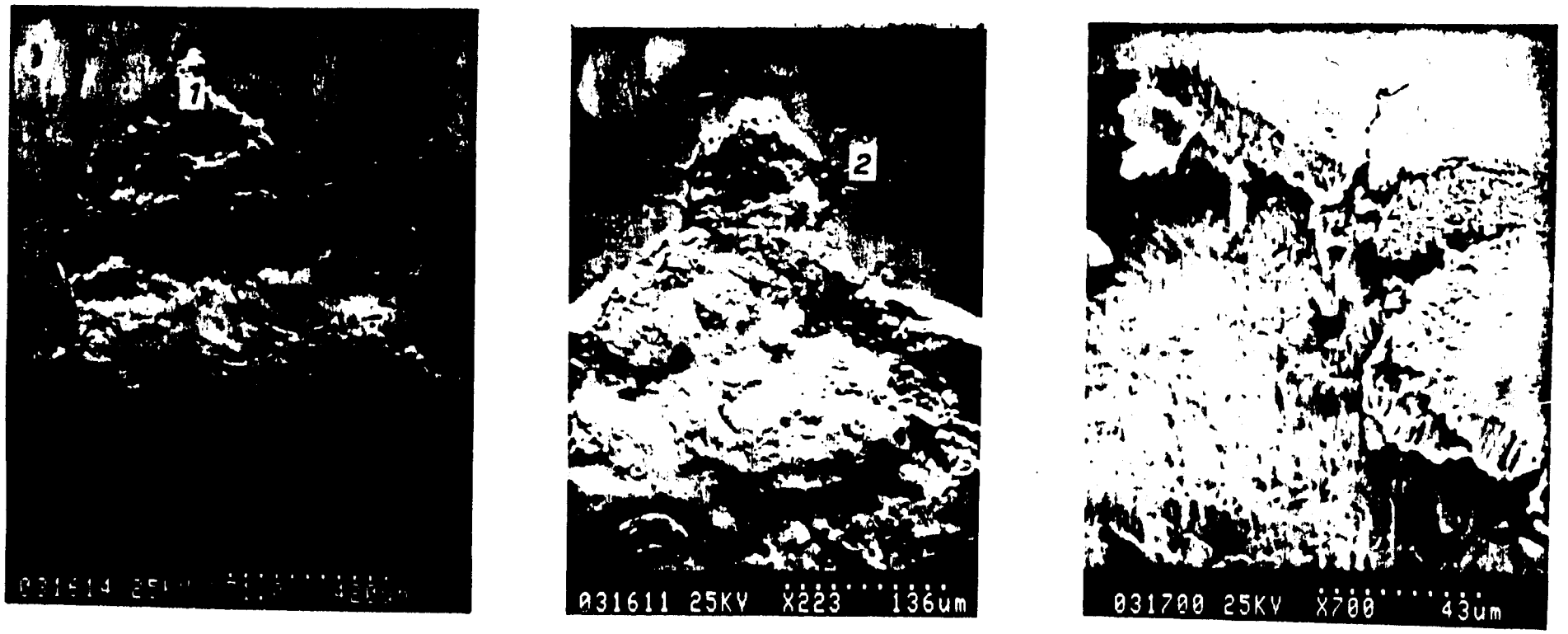

Figure 29. Characteristic "V"-shaped spall of a copper coated cylindrical specimen subjected to a Hertzian pressure p_o = 5.42 GPa and N = 3.1 • 10^7 contacts: (a) spall, (b) higher magnified view of initiation region 1 of (a), and (c) higher magnified view of Region 2 in (b) showing this to be an undercut, cantilevered flap.

Rolling Direction →

Figure 30. Wear track after the lubricated test showing the hardness impression (N = 15,000).

(A) (B)

Figure 32. Wear track after the unlubricated test showing: (A) extensive surface damage; and (B) magnified view of a "V-shaped" feature on the surface (N = 15,500).

6. ELASTO-PLASTIC FINITE ELEMENT ANALYSES OF ROLLING-PLUS-SLIDING

6.1 Introduction

In the past, elasto-plastic analyses of repeated rolling and rolling-plus-sliding contact have been confined to isotropic, elastic-perfectly-plastic (EPP) material behavior. Furthermore, the analyses were either limited to shakedown or not reliable.* As a result, such features of the contact as the magnitude of the cyclic strain amplitudes and residual stresses and their variation with depth remain ill-defined. Recently, Bhargava, Hahn and Rubin[18,19] have devised a finite element model of repeated rolling contact that is free of arbitrary assumptions. The model can treat EPP, isotropic hardening and elastic-linear-kinematic-hardening-plastic (ELKP) behavior[6,7]. It can simulate pure rolling[6,7,19] as well as rolling-plus-sliding[6,20] and 2-D[6,7,19,20] and 3-D contacts[21]. The results of such calculations reveal that the strain amplitudes and residual stresses are markedly affected when ELKP-behavior is substituted for perfect plasticity[6,7].

Finite element analyses of repeated, 2-D pure rolling contact have been carried out for high strength bearing steel with ELKP-material behavior and properties[7]. This section describes initial efforts to extend the ELKP calculations to repeated rolling-plus-sliding with materials parameters appropriate for the 440C steel.

6.2 Analytical Procedure

The finite element mesh employed is shown in Figure 32. It consists of 288, 8-noded, isoparametric plane strain elements and is roughly 16 w long

---

*The classical analyses of Merwin and Johnson[8] and Johnson and Jefferis[9] do not enforce equilibrium or continuity directly and require the arbitrary and over-constraining assumption that the total strain (elastic plus plastic) is equal to the Hertzian elastic value.

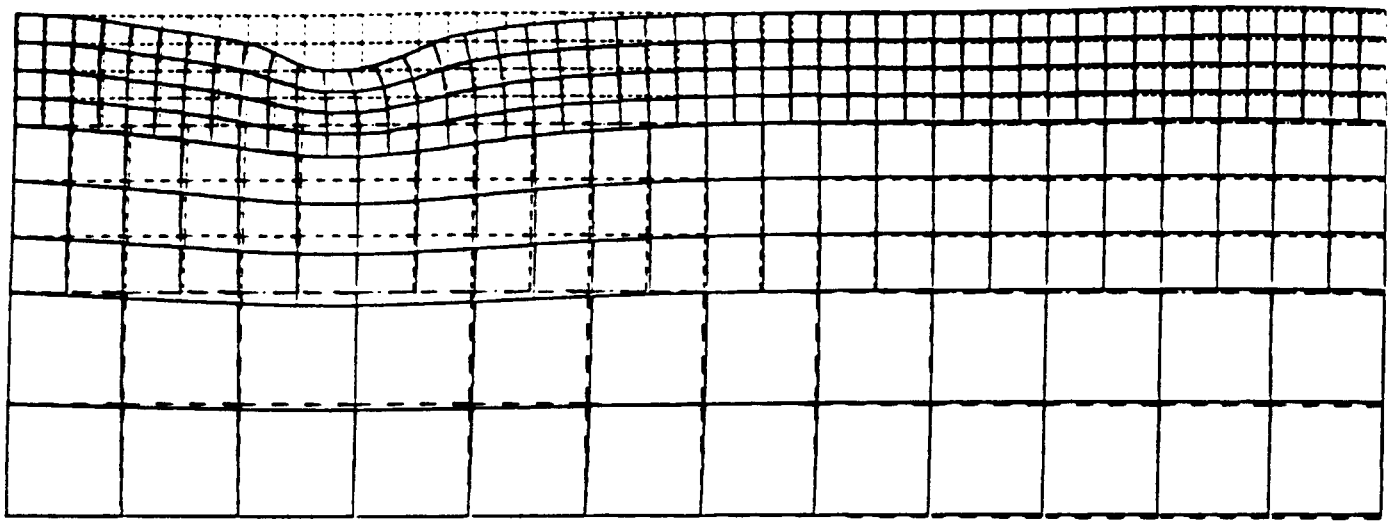

Figure 32. Deformed finite element mesh showing displacements under a normal Hertzian pressure p_o = 2500 MPa and the corresponding traction with a coefficient of friction μ =0.2. Displacements are magnified 24x.

and 6 w high (where 2w is the contact width). This mesh is made to mimic a semi-infinite half space by appropriately displacing the boundaries for each loading condition. Repeated rolling-sliding is simulated by translating a Hertzian pressure distribution and the appropriate surface tractions across the top of the mesh. A steady state is obtained after only two translations, hence only two translations need to be made. This and other features including the adequacy of the mesh have been verified previously[18,19]. The calculations are performed using the multipurpose finite element package "ABAQUS" and consume, typically, 2.10 cpu hrs on a VAX 8800.

The calculations employed ELKP behavior and material properties for 440C steel derived from the measurements in Section 3. Effects of surface heating on the ELKP parameters were neglected. Three rolling conditions were examined:

Case 1. Rolling-with-(full)sliding under a peak Hertzian pressure p_o = 2.5 GPa and a coefficient of friction μ = 0.2.

Case 2. Same as Case 1 with the value of σ_K reduced by 8% to reflect softening due to rim heating.

Case 3. Same as Case 1 with an elevated peak Hertzian pressure of p_o = 3.64 GPa and a coefficient of friction μ = 0.2.

The material parameters are used in the analysis and the rolling conditions simulated by the model for each of the three cases are summarized in Tables 3 and 4.

TABLE 3

MATERIAL PARAMETERS USED IN FINITE ELEMENT ANALYSIS

	Case 1	Case 2	Case 3
Young's Modulus, E (MPa)	2.07×10^5	2.07×10^5	2.07×10^5
Poisson's Ratio,	0.3	0.3	0.3
Plastic Modulus, M (GPa)	188	188	188
Kinematic Yield Stress, σ_k (MPa)	1050	962.3	1050
Kinematic Shear Yield Strength, k_k (MPa)	606.2	555.6	606.2

TABLE 4

ROLLING CONDITIONS

	Case 1	Case 2	Case 3
Radius of Half Space, R_1			
Radius of Rigid Contact Cylinder, R_2 (m)	0.05	0.05	0.05
Hertzian Peak Pressure, p_o (GPa)	2.500	2.500	3.64
Hertzian Contact Width, 2w (mm)	2.2	2.2	3.18
Ratio of Tangential to Normal Force, T/N	0.2	0.2	0.2
Coefficient of Friction, μ	0.2	0.2	0.2
Ratio of Hertzian Peak Pressure to Kinematic Shear Yield Strength, p_o/k_k	4.124	4.5	6.0

6.3 Results

The appearance of the mesh after the first and second contact at $p_o/k_k = 6$ is illustrated in Figure 33. Note that the displacements are magnified 820X to make them readily visible. At this magnification a substantial amount of deformation is visible after the first contact but there are virtually no further changes in the displacements after the second contact. The implication is that the plasticity is not reversed during the first contact, but is fully reversed during the second and subsequent contacts as a result of kinematic hardening. This is confirmed by the stress-strain histories experienced by the material as shown in Figure 34.

The magnitude of the continuing cyclic plasticity experienced during the second and subsequent contacts is illustrated in Figures 35-37. These show the variations with depth below the surface of $\Delta\varepsilon^p_y$, the radial plastic strain range, and $\Delta\bar{\varepsilon}^p$ the equivalent strain range, which peak at a relative depth of $y/w \sim 0.65$. The magnitudes of the peak equivalent strain range $0.0005 \leq \Delta\bar{\varepsilon}^p(\max) \leq 0.002$ for $4.5 < p_o/k_k < 6$, correspond with the values of $\Delta\bar{\varepsilon}^p$ for which the ELKP properties were evaluated in Section 3.

The circumferential and axial residual stresses are described in Figures 38 and 39. These are related to the net amounts of plastic deformation produced during the first contact. The peak compressive values, 20 MPa $\leq \sigma^R_{max} \leq$ 35 MPa are quite modest. The small circumferential tensile residual stress values obtained close to the surface at the highest contact pressure; are not observed in the absence of shear tractions. They are interesting because they produce a fluctuating tensile stress, and Mode I driving force for radial cracks, but appear to be too small: $\sigma^R_{x(max)} = 17$ MPa to enforce cyclic crack growth. Comparisons with results for pure rolling (see Figures 35, 36, 38 and 39) with the same ELKP properties show that the shear tractions

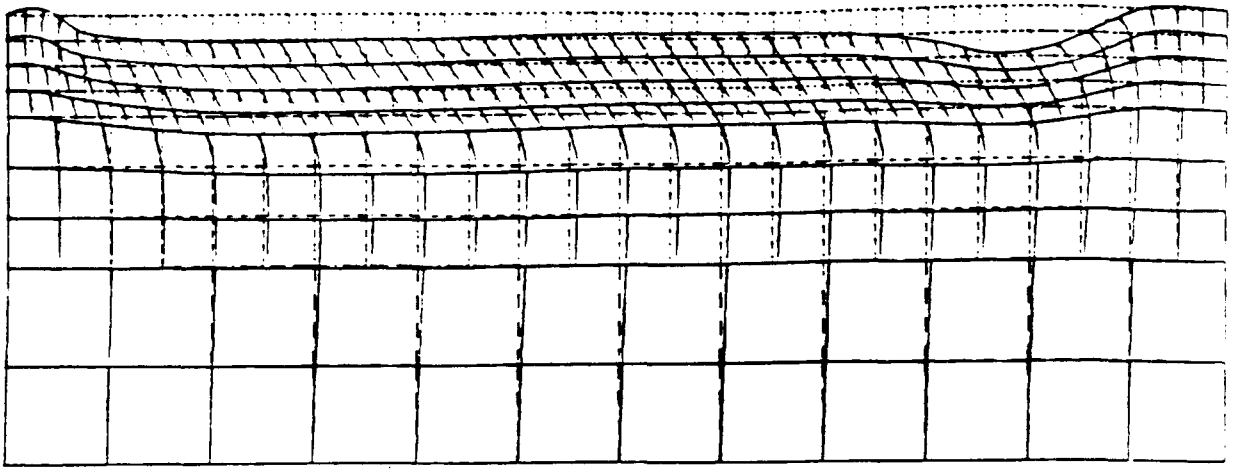

(a) After I Contact

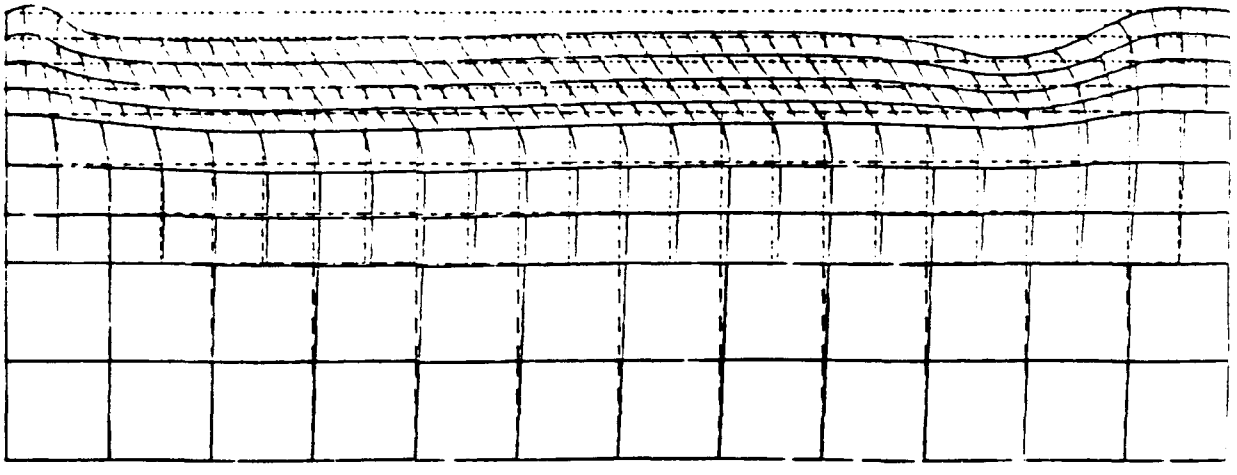

(b) After II Contacts

Figure 33. Deformed mesh for Case 3: $p_o/k_k = 6.0$, after the load is removed. Displacements are magnified 820X.

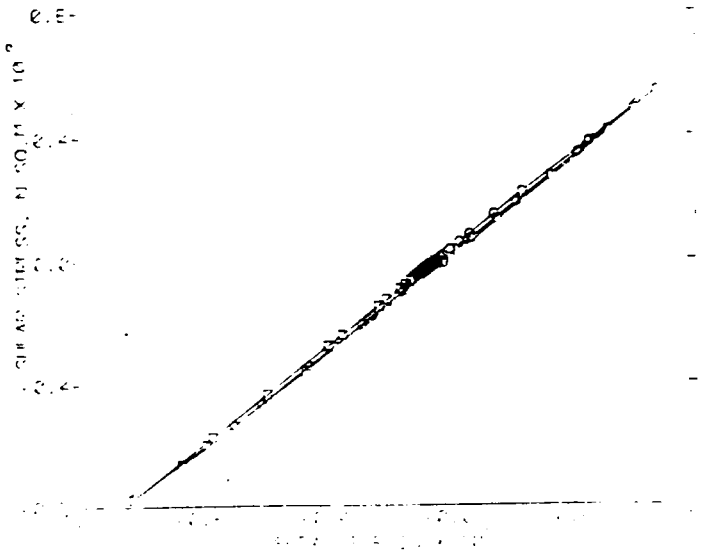

(a)

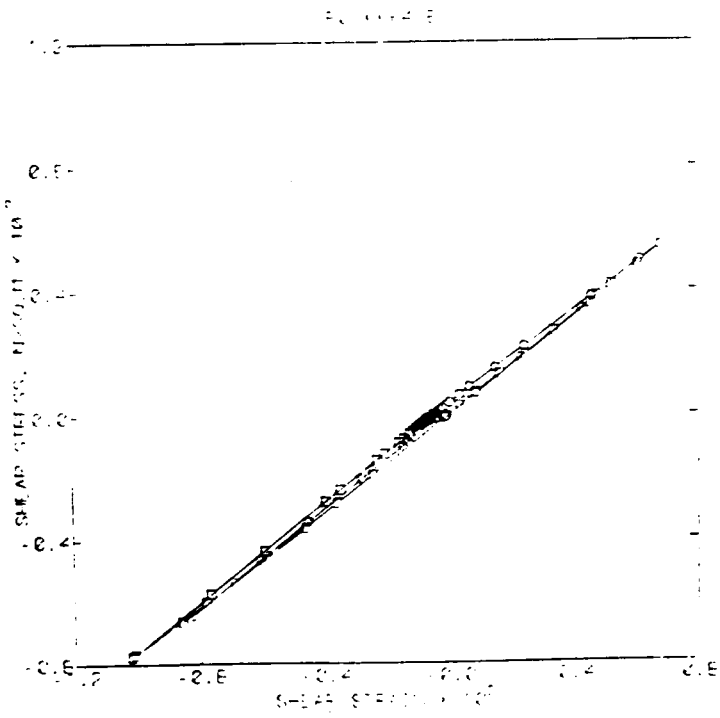

(b)

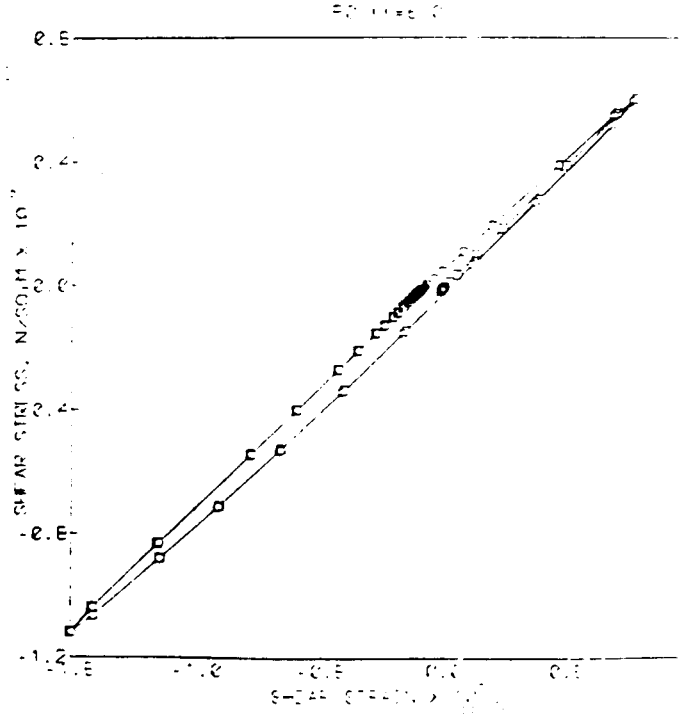

(c)

Figure 34. The stress-strain history produced at a depth of y = 0.4w for the first and second contacts, derived from the model for 3 different relative pressures: (a) p_o/k_k = 4.124, (b) p_o/k_k = 4.5, and (c) p_o/k_k = 6.0.

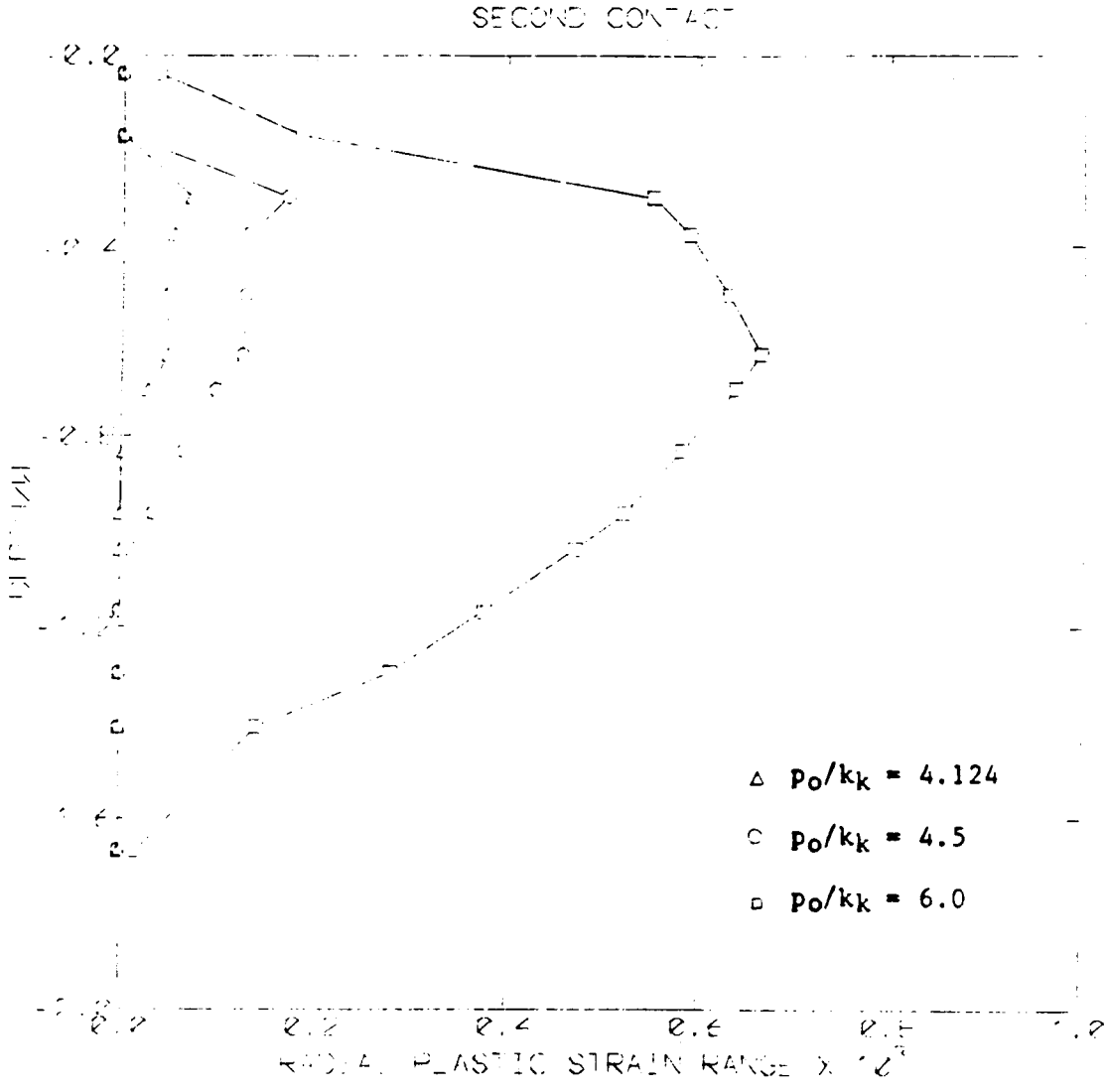

Figure 35. Variation of the radial plastic strain range, $\Delta\varepsilon_y^p$, with normalized depth.

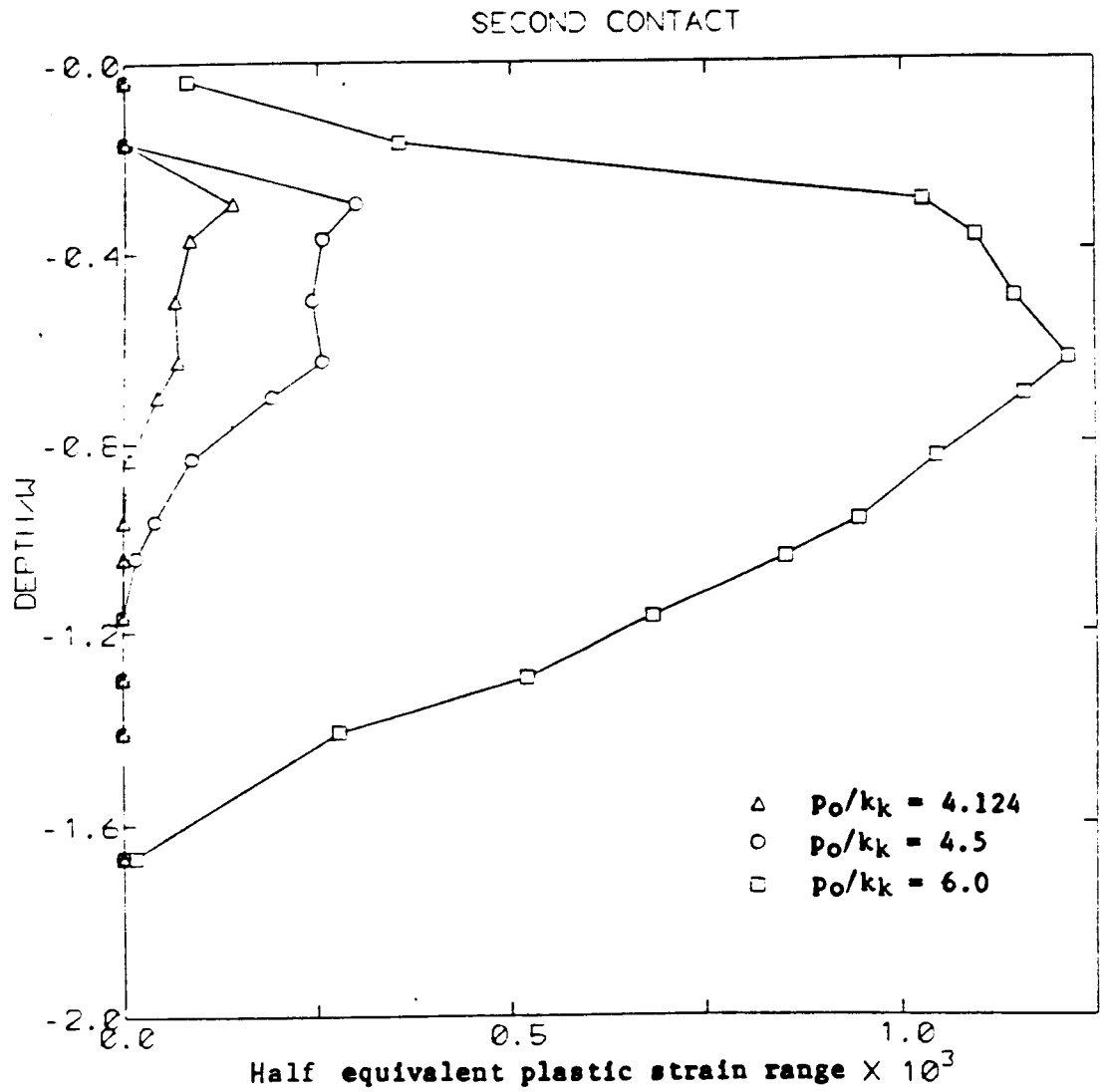

Figure 36. Variation of the half equivalent plastic strain range, $\Delta\bar{\varepsilon}_p/2$, with normalized depth.

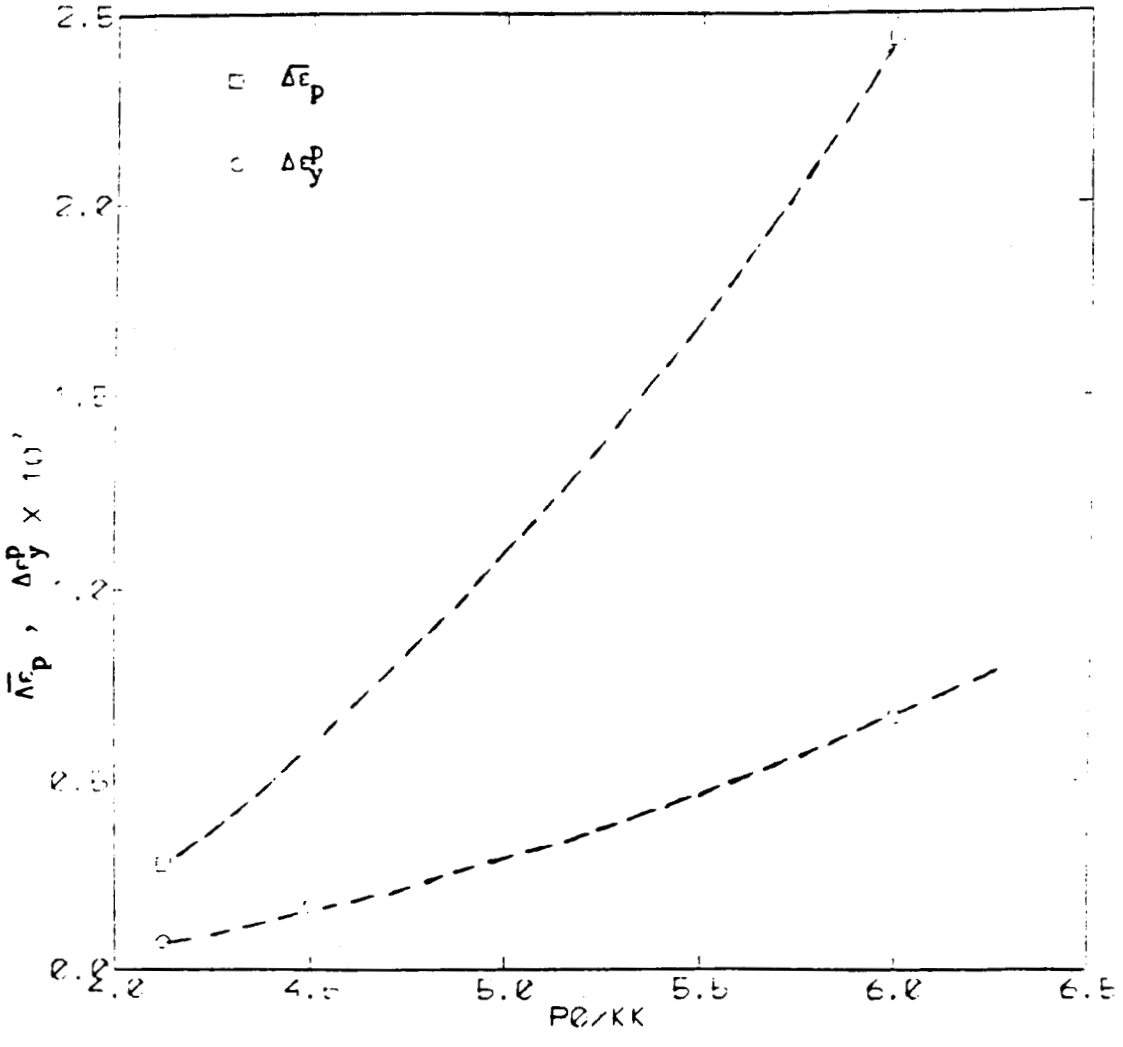

Figure 37. Variation of peak values of $\overline{\Delta\varepsilon}_p$ and $\Delta\varepsilon_y^p$ with p_o/k_k.

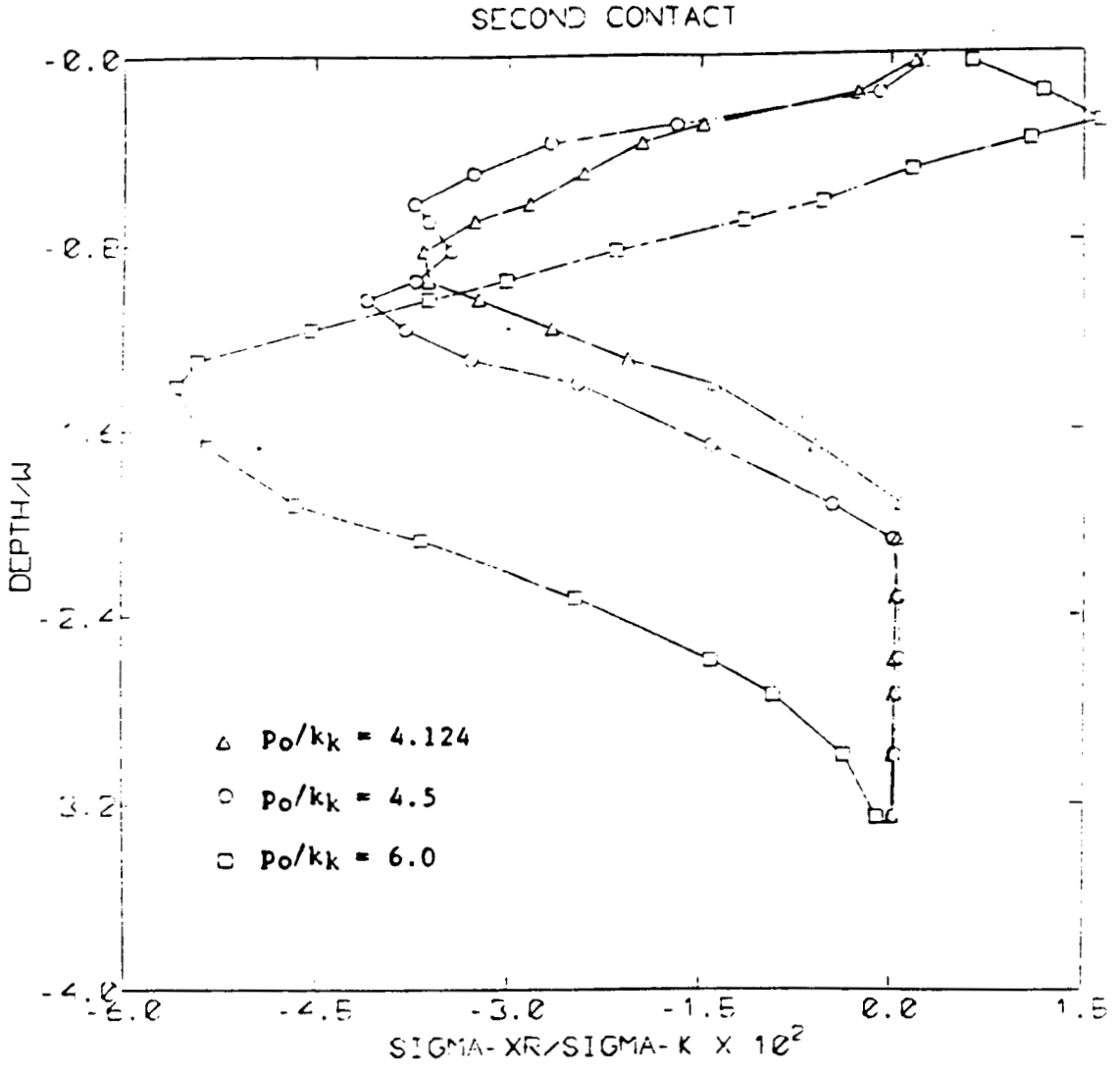

Figure 38. Variation of the normalized circumferential residual stress with normalized depth.

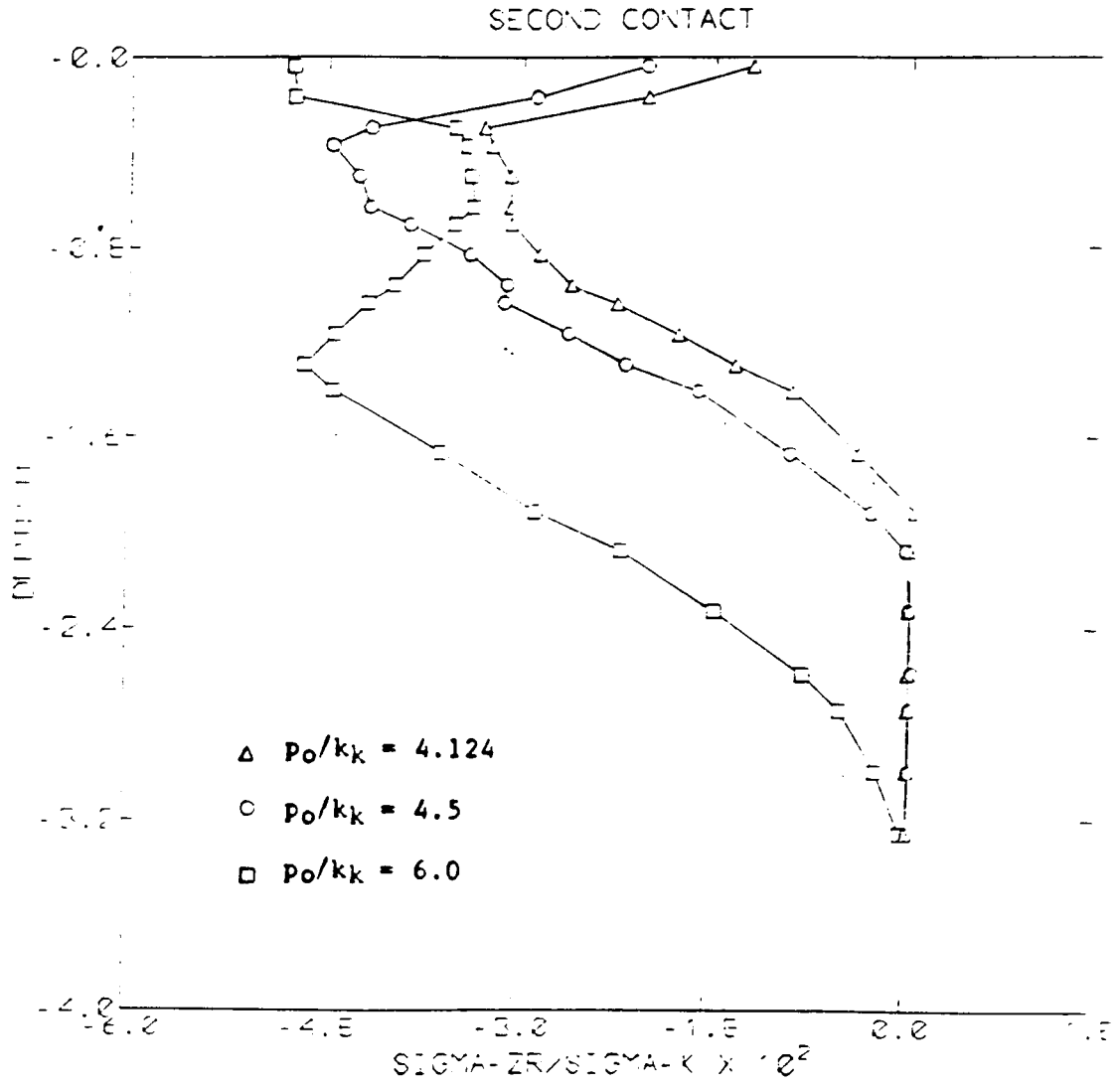

Figure 39. Variation of the normalized axial residual stress with normalized depth.

have hardly any effect on either the plastic strain ranges or the residual stresses. This is not found to be the case for EPP-behavior which leads to much larger strains and stresses in the presence of shear tractions.[20]

Table 5 illustrates the variation of U_i, the plastically dissipated energy per unit translation of a unit length of line contact, with normalized depth. The averages of these values, U_p , are the total plastic energy dissipated in the plastic zone during contact, most of which is converted to heat. These values are from 3% to 15% of the energy dissipation of friction*, U_f, for S = 2% slip. While the adiabatic temperature rise produced by the plastic deformation is significant, e.g., 0.6^oC per contact, it is a small fraction of the rise produced by friction at the running surface. The heat generation rate U = 41.9 KJ/m^2 corresponds to U = 51.9 KW.**

---

*The energy dissipation of friction is $U_f = 0.5 \mu w p_o s$ where s is the slip.

**For an average (inner/outer) race diameter of 65 mm and 13 balls rotating at 28,000 rpm with an effective contact ellipse dimension v = 1 mm.

TABLE 5

VARIATION OF THE PLASTIC ENERGY DENSITY IN 367 μm LAYERS OF THE FINITE ELEMENT MODEL WITH RELATIVE DEPTH

Relative Depth, y/w	Plastic Energy, U_i (MJ/m^3), Density Case 1	Case 2	Case 3
0.167	0.227	0.320	1.450
0.5	0.602	0.874	3.283
0.833	0.434	0.657	3.077
1.166	0.217	0.326	2.185
1.667	0.039 0.039	0.084 0.084	0.723 0.723
2.334	0	0	0.168 0.168
2.867	0	0	0.009 0.009
3.0	0	0	0
4.0	0	0	0
5.33	0	0	0
U_i, MJ/m^3	1.56	3.87	11.8
U_p, KJ/m^2	0.476	1.18	5.41
T, °C/contact	0.08	0.18	0.60
U_f, KJ/m^2	17.3	17.3	36.5
U, KJ/m^2	17.8	18.5	41.9

U_i - Plastic energy density in a layer

U_p - Plastic energy dissipated per unit of contact translation per unit thickness: $U_p = y_o \Sigma U_i/n$, where y_o is the total depth of plastic zone and n is the number of layers composing it.

U_f - Energy dissipated by friction at the surface per unit of contact translation per unit thickness: $U_f = 0.5 \mu w p_o s$, where 2w is the contact width, p_o is the peak pressure, $\mu = 0.2$ is the coefficient of friction and $s = 0.02$ is the slip.

U_T - Total energy dissipated as heat per unit contact translation per unit thickness: $U = U_p + U_f$.

T - Adiabatic temperature rise plastic zone arising from plastic

7. FINITE ELEMENT MODEL OF FRICTIONAL HEATING UNDER ROLLING AND SLIDING CONTACT

7.1 Introduction

Poorly lubricated bearings exposed to rolling and sliding contact under load may also be subject to high temperatures and thermal stresses arising from the frictional heating. The bulk of the literature in this area deals with theoretical thermo-elastic treatments[22-35]. Mow and Chen[36] obtained an anlaytical solution to the stresses induced by an arbitrarily distributed, fast moving heat source on a convective elastic-half plane. There are a few elastic and elastic-plastic finite element analyses, but they are concerned with the effects of thermal and thermal-mechanical loading for a rail wheel in regions far removed from the contact[37-40]. Theoretical and experimental work has been done to study the reduction in bearing service life due to localized overheating observed for HPOTP bearings used in the Space Shuttle Main Engine[42,43]. A more recent, elastic-plastic, thermomechanical model of the region near a shallow weld in a thick plate developed by Newman[44] reflects the growing sophistication of the analyses. The main limitation of these models in dealing with the non-stationary temperature field is that only the effect of thermal loading is considered. Hence, there is a need for coupled temperature-displacement analysis of rolling and sliding contact in order to deal with the problem more accurately. This section describes preliminary steps towards a coupled temperature-displacement finite element analysis of rolling and sliding. The intent of the study was to determine whether the thermal stresses are large enough to affect the local stress state produced by elastic plastic contact. The results show large effects that radically alter the residual stress state for large heat fluxes.

7.2 Description of the Model

A finite sized mesh with appropriate boundary conditions has been used to perform a coupled temperature displacement elastic-plastic finite element analysis of a long, stationary, heat-generating Hertzian cylinder indenting a semi-infinite half plane. All the heat generated in the cylinder is assumed to be conducted into the semi-infinite half plane. The model approximates the steady state temperature distribution produced by a rapidly rotating heat source, and the stresses and deformations directly under the contact. However, it sheds no light on the cyclic temperature, thermal and applied stress fluctuations produced by a moving contact. A 3-dimensional model of contact that can treat aspects of the moving contact problem is being developed separately.

The finite element mesh (Figures 40 and 41) is made up of 8 noded plane-strain elements (biquadratic in displacement and linear in temperature). Taking advantage of symmetry, x-displacements along side BC are constrained, sides AD and DC are maintained at ^{o}C. For the purpose of calculating the displacements along sides AD and DC, the semi-elliptical Hertzian distribution is represented by 100 concentrated normal forces indenting an elastic half plane. The effect of shear tractions is represented by the heat fluxes, but their mechanical effect has not been included. The displacements at the nodes along AD and DC are calculated for each of the concentrated forces and then superposed. Nonuniformly-distributed mechanical and thermal loading is applied over a half contact width, w, on side AB starting from point B. The remainder of side AB is assumed to be convective.

Calculations are performed for a $p_o/k = 4.0$, (where p_o is the peak pressure and $k = \sigma_o/3$, is the cyclic shear resistance), thermal conductivity, $K = 60$ w/m ^{o}K, a uniform film coefficient, $h = 500$ w/m-^{o}K, Young's modulus,

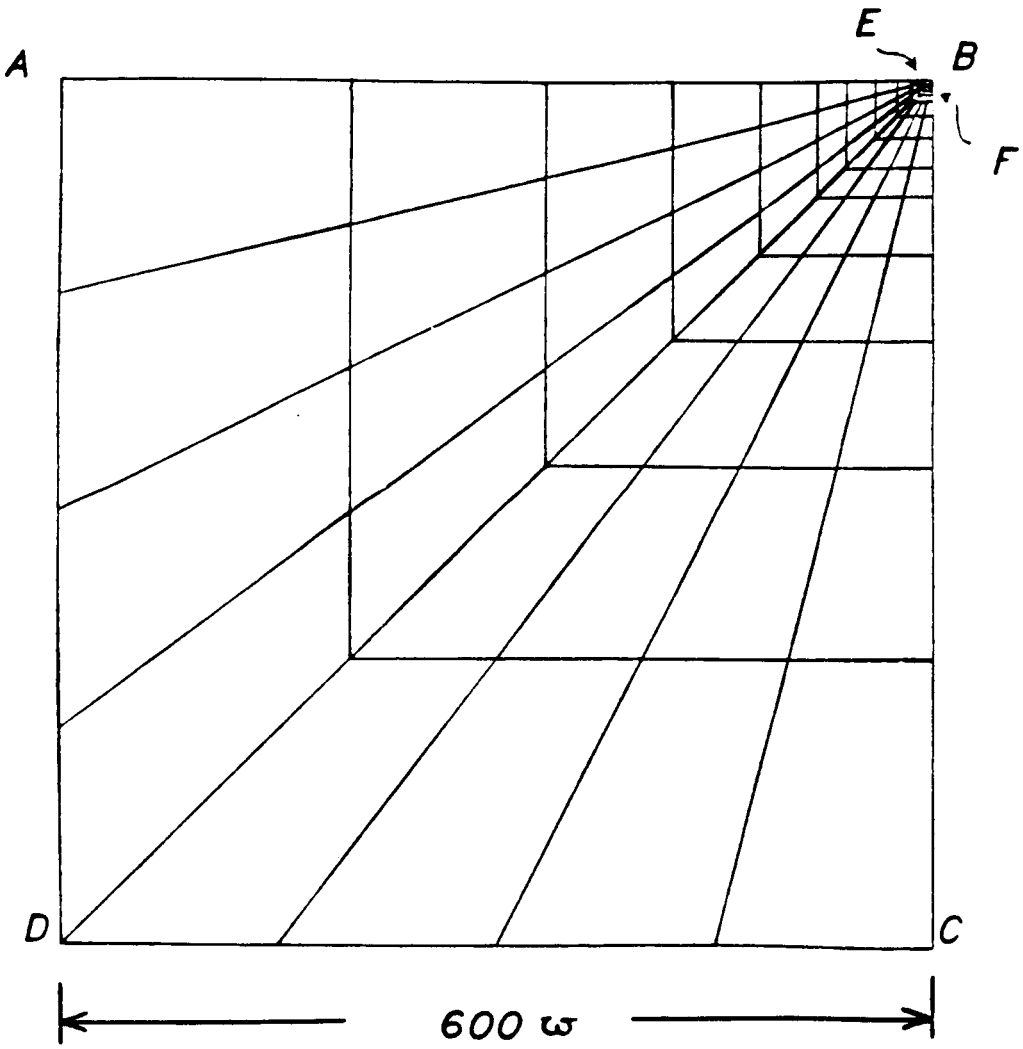

Figure 40. Finite element mesh used in the coupled temperature-displacement analysis. The contact half width w = 0.6 mm.

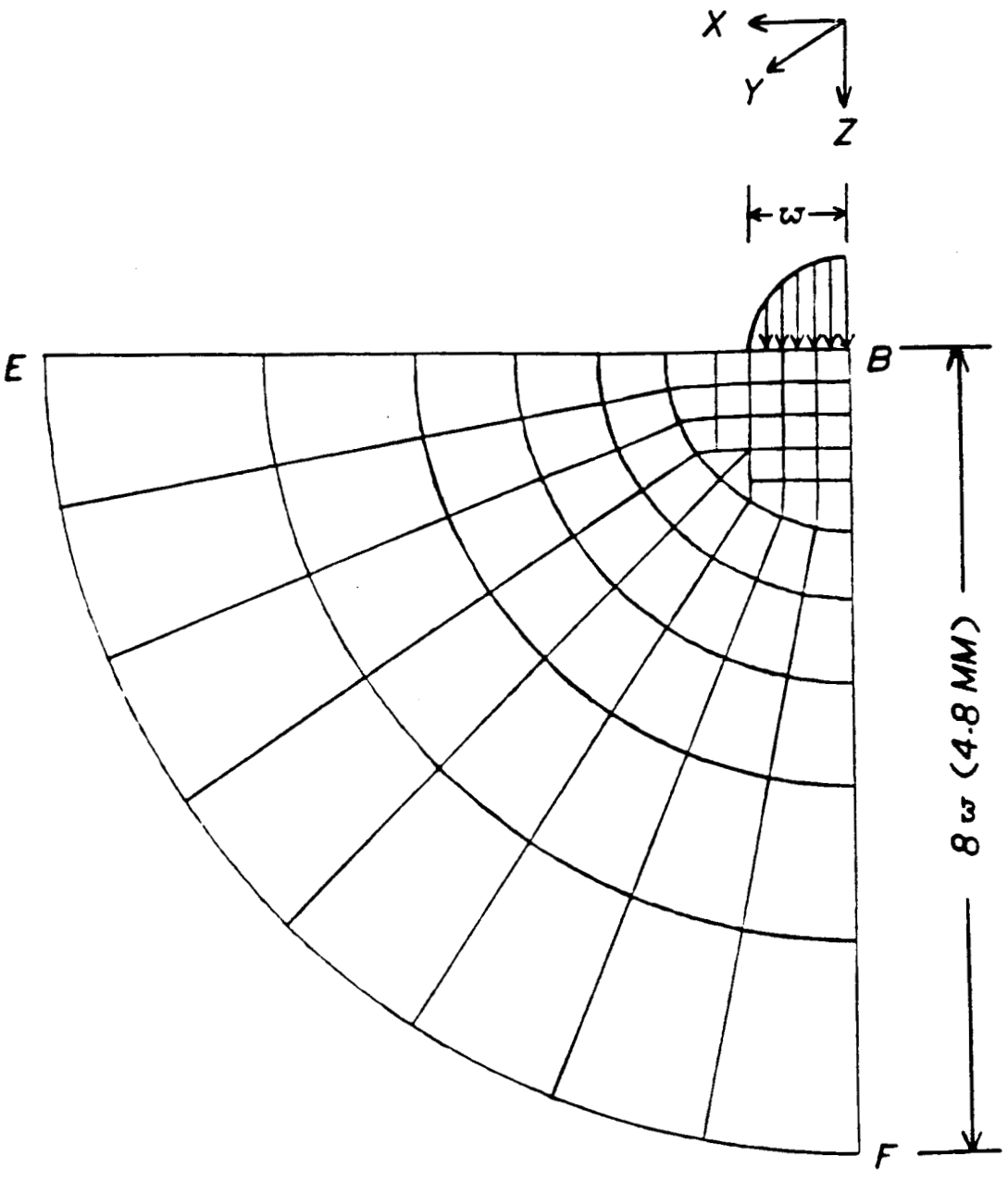

Figure 41. Detailed mesh inside the region BEF (refer to Figure 40).

E = 207 GPa, Poisson's ratio, μ = 0.3, and a temperature independent yield stress, σ_o = 393.98 MPa. The film coefficient was selected to give a peak temperature of about 1000°C at the highest heat flux consistent with experimental evidence[2]. The calculated temperature gradient is illustrated in Figure 42. The absolute value of σ_o has little significance for the elastic-perfectly plastic model. Nine calculations were made, one of them being a pure displacement analysis and the rest being coupled temperature-displacement analyses (see Table 6). Different values of heat flow were considered for the coupled calculations and steady state conditions were assumed to exist. The heat flux (q) and the Hertzian (contact) pressure distribution (p) are given by the following expressions:

$$q(w/m^3) = p_o V \mu[1 - (x^2/a^2)], \text{ and}$$

$$p(N/m^2) = p_o [1 - (x^2/a^2)]$$

where: p_o = peak pressure, N/m^2

μ = coefficient of friction

V = rolling velocity, m/a

w = half contact width; w = 0.6 mm.

Calculations were performed for the range of heat fluxes shown in Table 6. The highest value corresponds closely with the values of 10^5 KW/m^2 reported for HPOTP bearings[1,2]. The model was loaded and unloaded in increments to avoid convergence problems. The finite element modeling was done on the multipurpose finite element package "ABAQUS" on a VAX 8800 computer. Typical CPU time for a calculation was found to be 30 minutes.

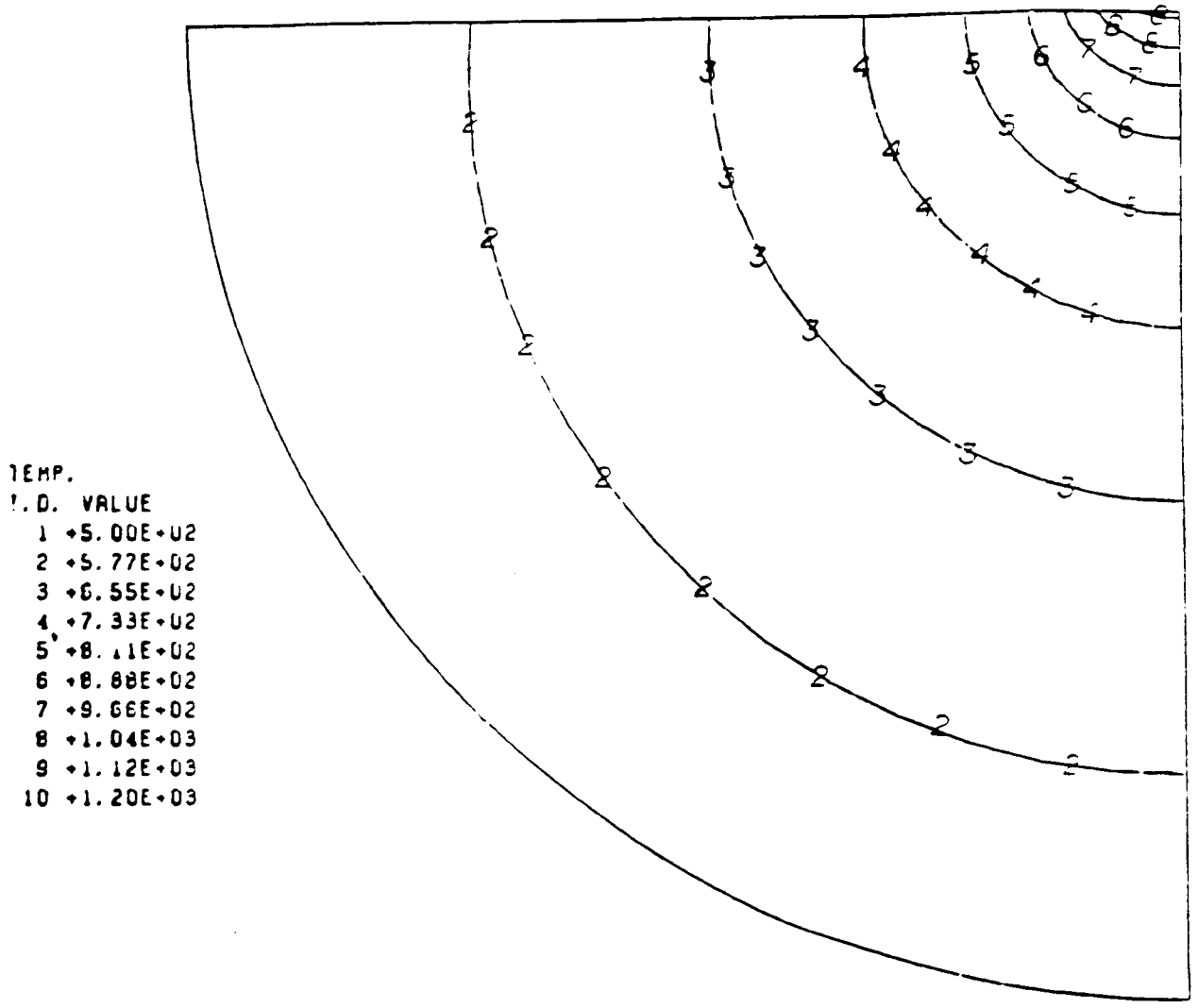

Figure 42. Temperature contours for a heat flux input of 8.6×10^4 KW/m^2.

TABLE 6

HEAT FLUX INPUTS USED IN THE ANALYSIS IDENTIFIED BY NUMBERS IN FIGURES 12 THROUGH 28

Analysis Identifier	Heat Flux kw/m^2
1	8.6×10^4
2	5.7×10^4
3A	4.3×10^4
3	2.9×10^4
3B	2.1×10^4
4	1.4×10^4
5	0.6×10^4
6	0.3×10^4
S	0

7.3 Results

As mentioned earlier, eight different heat input values were used in the coupled temperature displacement analyses. Results are presented for the loaded was well as the residual state for each case analyzed. The stresses are normalized with respect to K, the strains with respect to K/G and the depth with respect to w.

Figures 43 and 44 show the normalized residual axial stress for the various cases, and Figures 45 and 46 present the normalized residual circumferential stress. The presence of thermal loading does seem to have an effect on the residual stress state, when the heat rate input exceeds 1.67×10^4 KW/m^2 for the parameters used here.

For the pure mechanical loading case, the residual axial stresses compare well (qualitatively) with those found in existing literature[40,41]. When the heat input is low, the residual stress distributions do not change qualitatively but a slight change is observed quantitatively. However, for heat flux values exceeding 1.67×10^4 KW/m^2, drastic changes are observed in the residual axial and circumferential stresses, qualitatively as well as quantitatively. In the present analyses, for the pure mechanical loading case, the residual circumferential stress attains a high compressive value at a depth of 0.65 w below the surface and then tapers off to a low tensile value. On the other hand the axial stress first becomes tensile then, with depth, reverses to attain a high compressive value and then tapers off. With the addition of heat input, the residual axial and circumferential stresses change character and for high heat rates, they become totally tensile. For the parameters considered here, the axial stress becomes tensile for heat transfer flow values above 5.83×10^4 KW/m^2 whereas the circumferential stress becomes trensile for a heat flux value exceeding 1.33×10^4 KW/m^2.

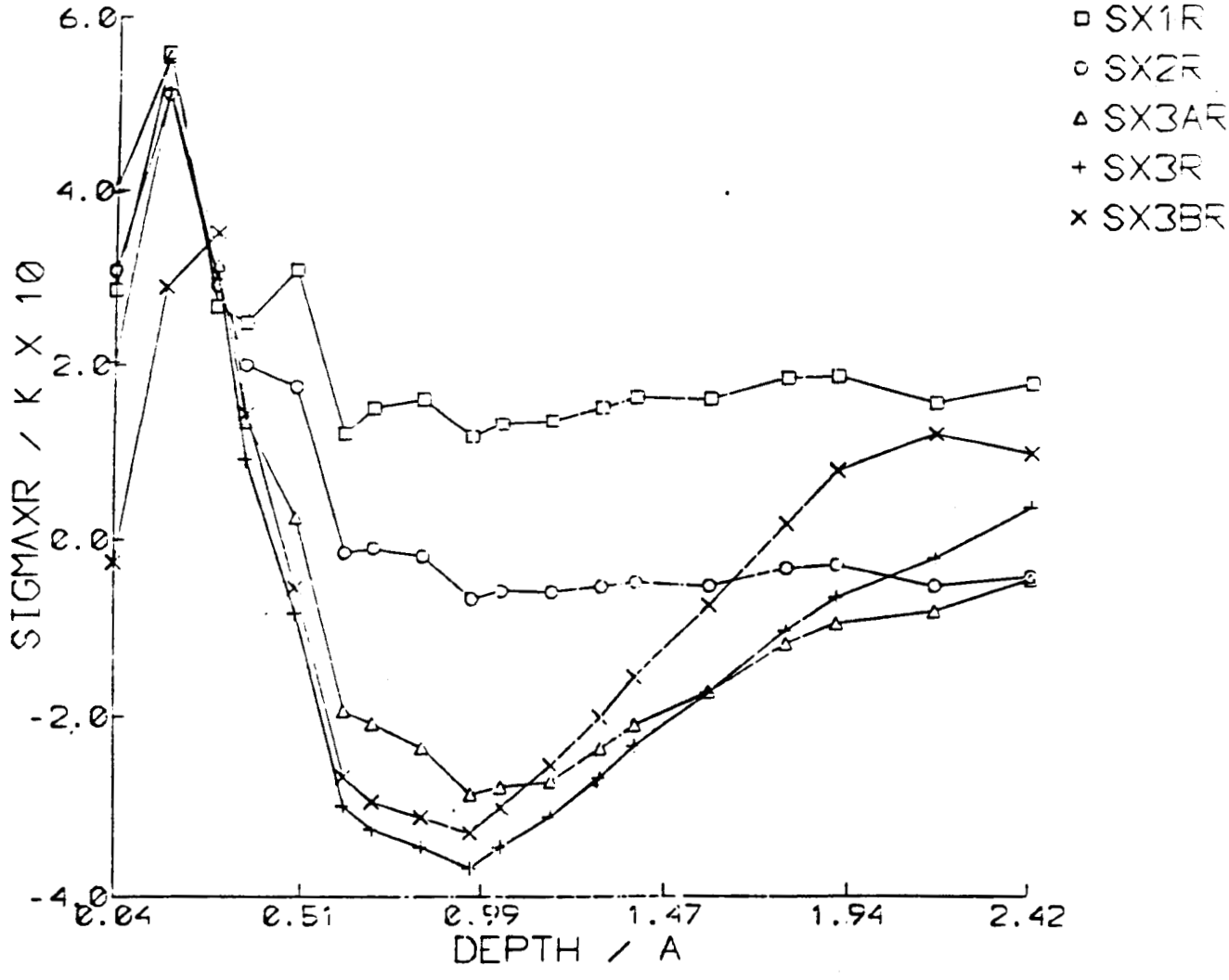

Figure 43. Variation of the normalized residual axial stress, SXR, with normalized depth for different heat inputs (see Table 6).

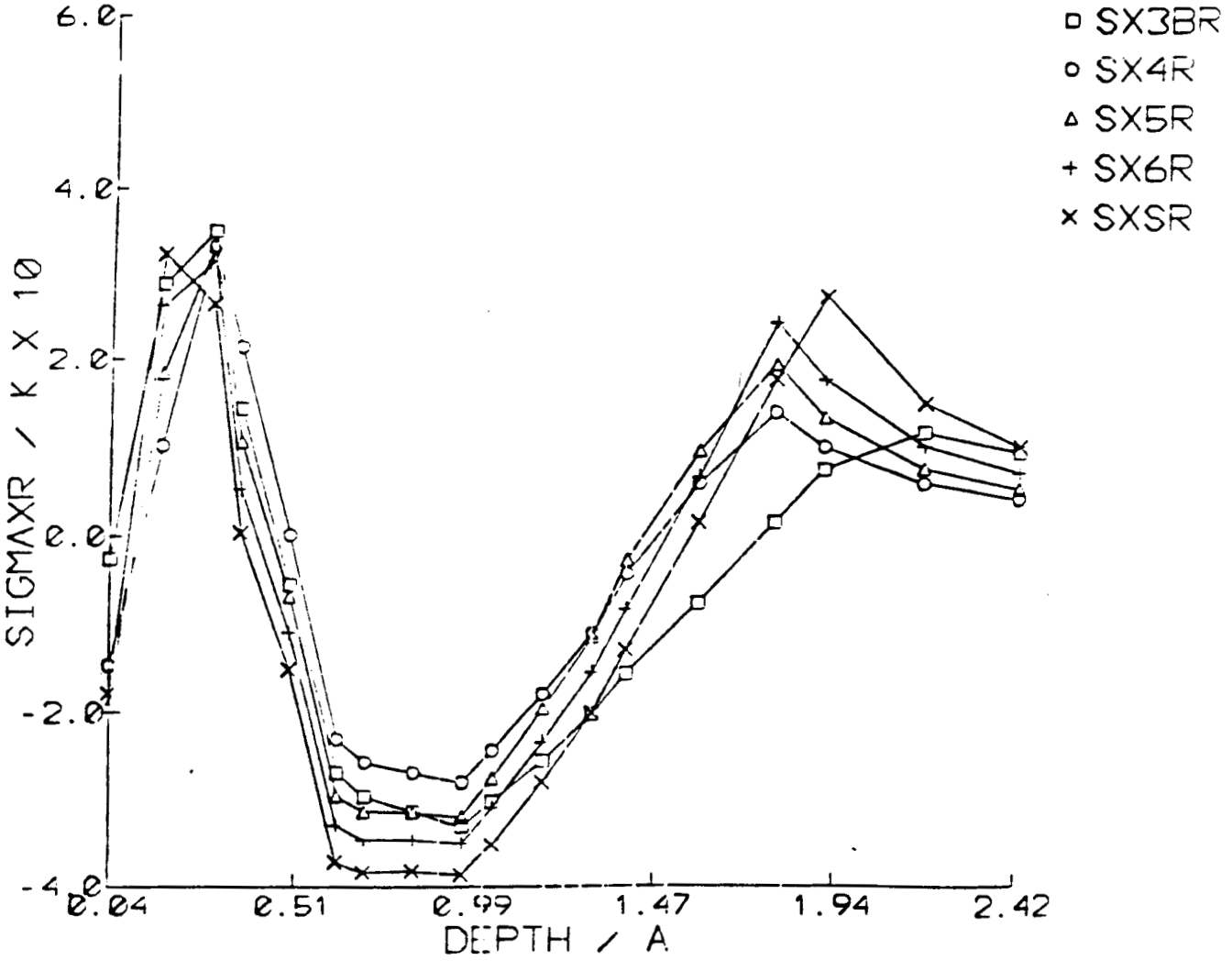

Figure 44. Variation of the normalized residual axial stress, SXR, with normalized depth for different heat inputs (see Table 6).

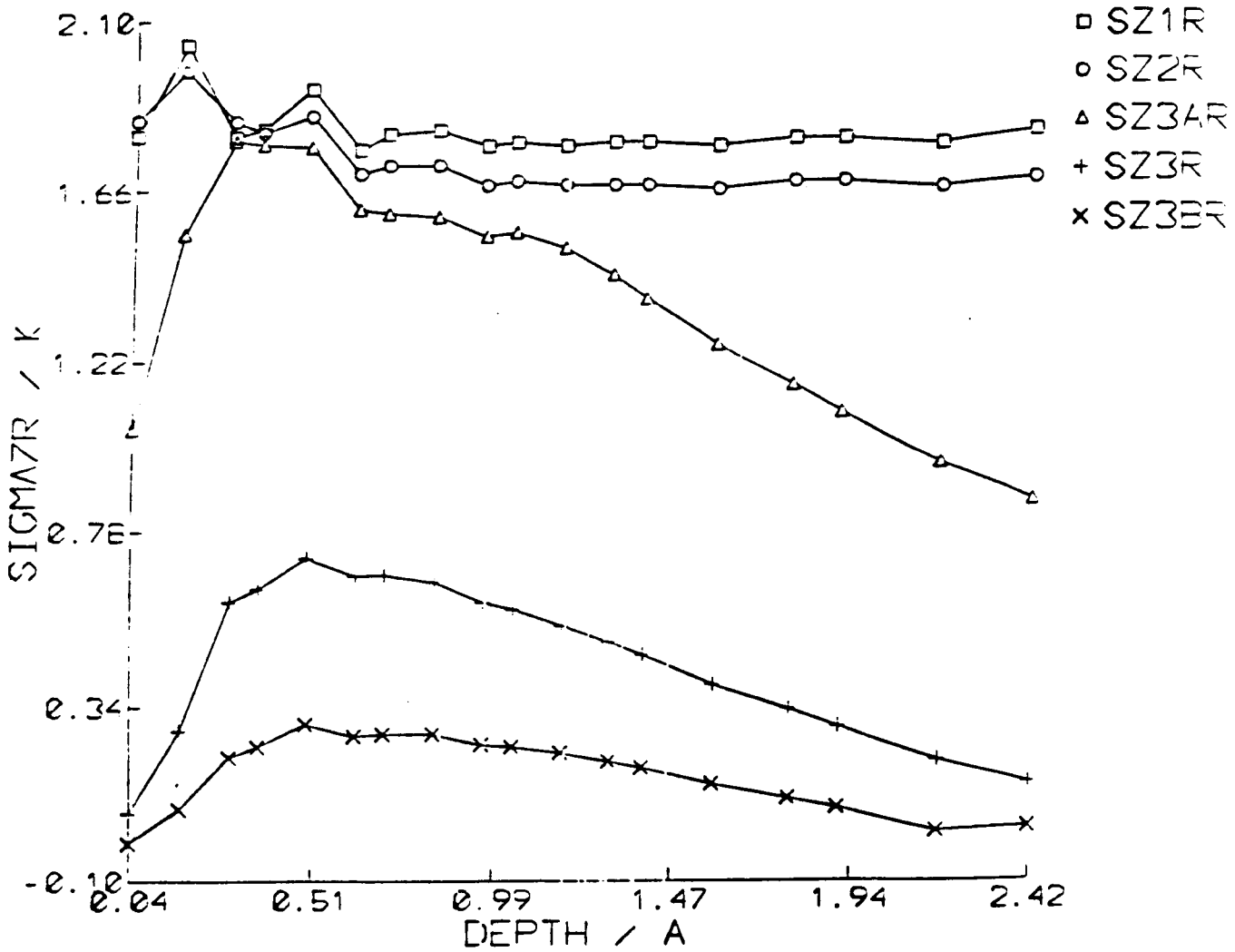

Figure 45. Variation of the normalized residual circumferential stress, SZR, with normalized depth for different heat inputs (see Table 6).

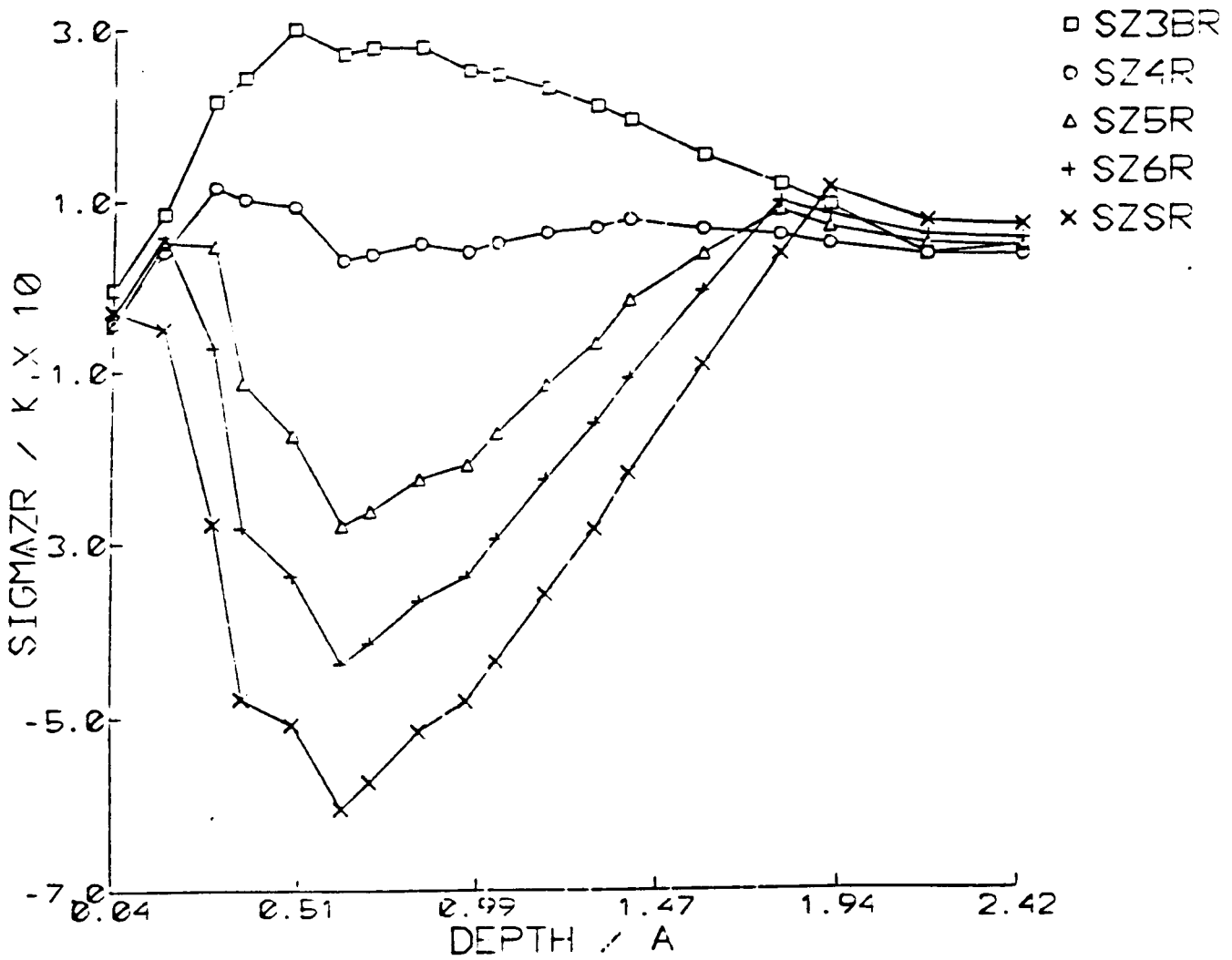

Figure 46. Variation of the normalized residual circumferential stress, SZR, with normalized depth for different heat inputs (see Table 6).

For a heat flux input of 8.6×10^4 KW/m^2, both the axial and circumferential residual stresses are found to be entirely tensile. Figures 47 and 48 plot the normalized residual radial and shear stresses against normalized depth. As expected, thermal loading has no effect on these residual stresses. Figures 49, 50 and 51 show the residual stresses for a heat flux input of 8.6×10^4 KW/m^2, for a heat flux input of 2.14×10^4 KW/m^2 and for zero heat flux input, respectively. Figures 52, 53, 54 and 55 show the stress distribution for the loaded conditions. All the above figures indicate that for combined mechanical thermal loading, the most significant effect of the heat input is on the circumferential stress. The thermal input also effects the residual strains (Figures 56, 57, 58 and 59) and displacements (Figures 60, 61, 62, 63, 64, and 65).

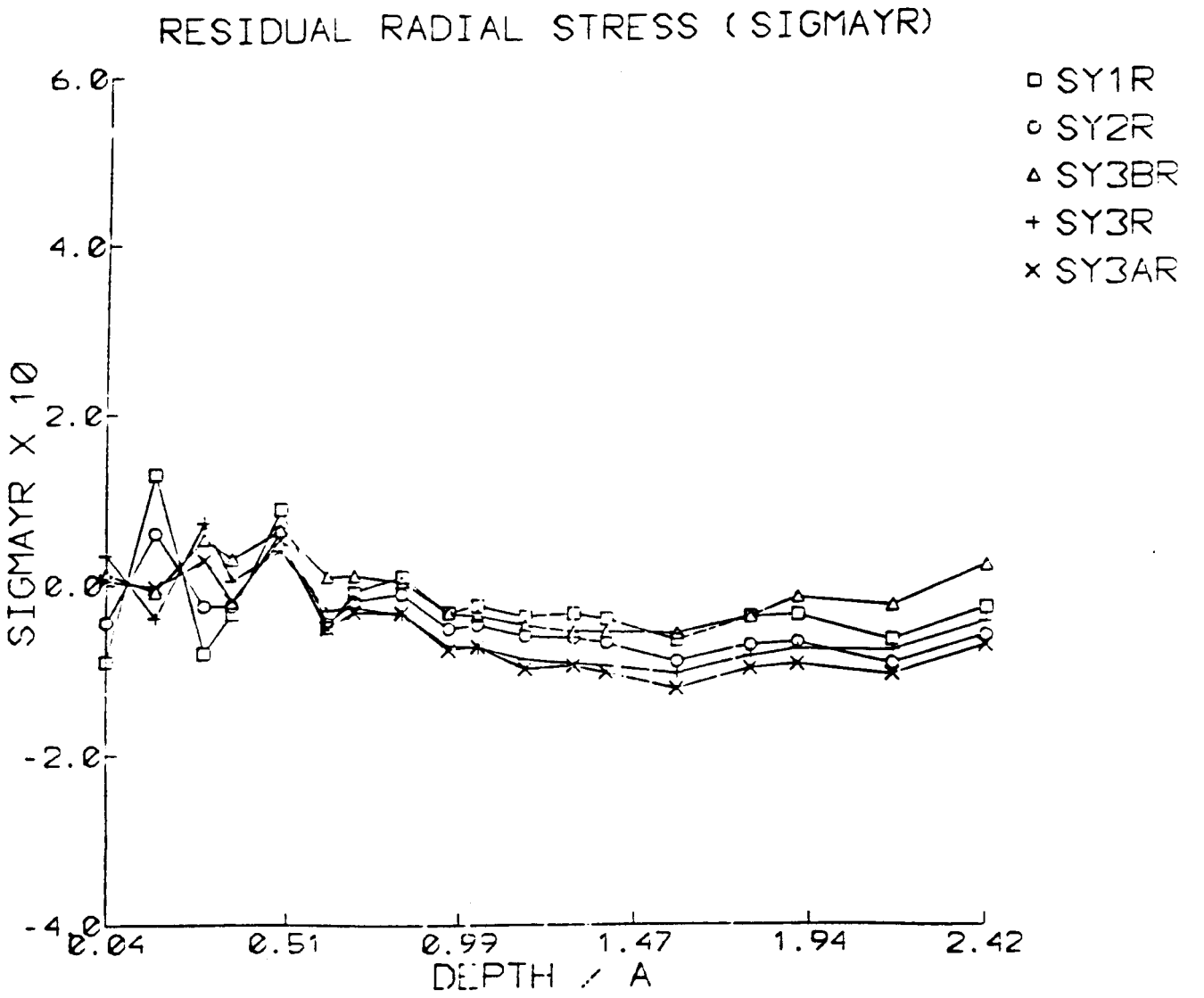

Figure 47. Variation of the normalized residual radial stress, SYR, with normalized depth for different heat inputs (see Table 6).

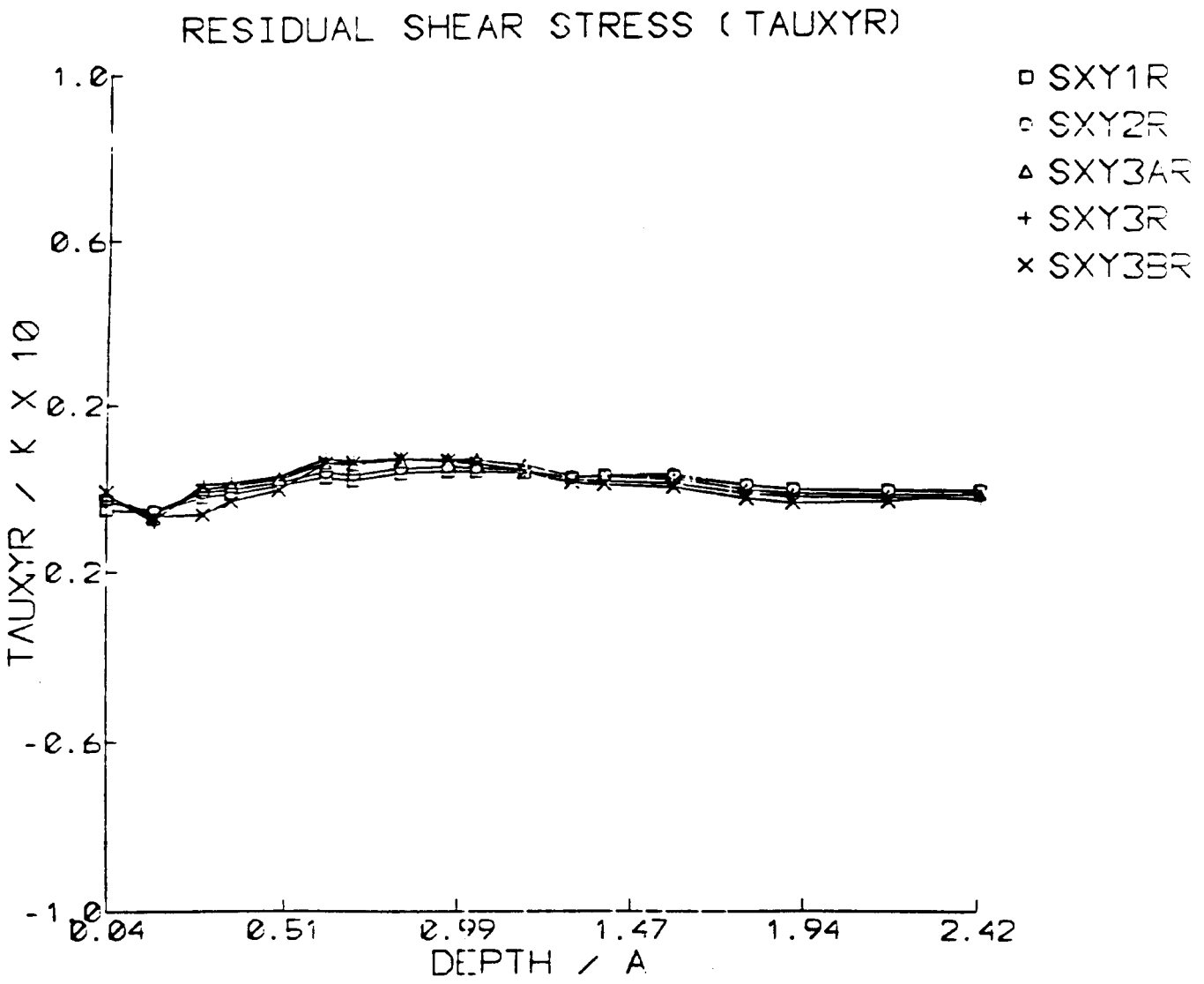

Figure 48. Variation of the normalized residual shear stress, SXYR, with normalized depth for different heat inputs (see Table 6).

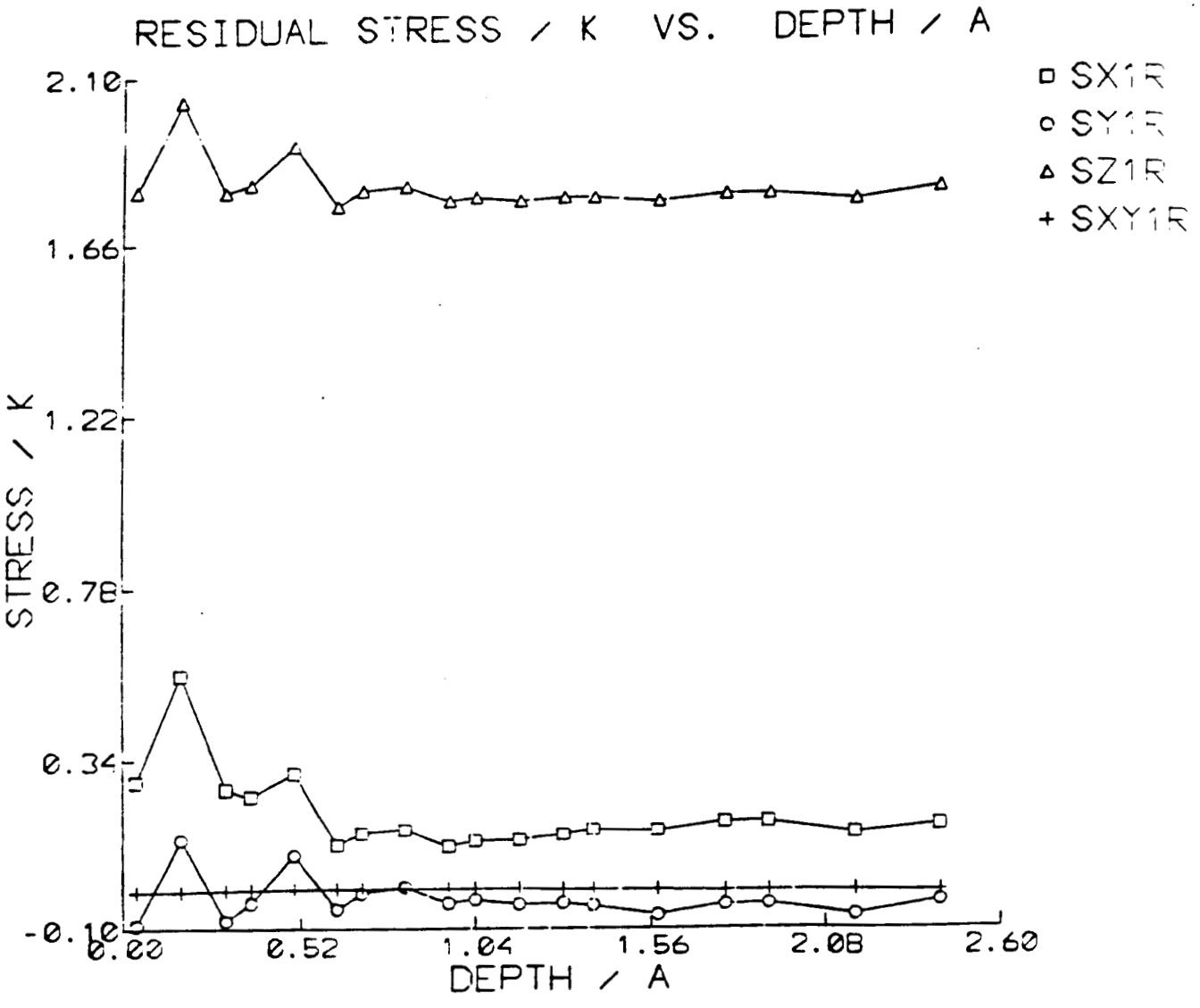

Figure 49. Variation of the normalized residual stresses, S1R, with normalized depth for a heat flux input of 8.6×10^4 KW/m^2 (see Table 6).

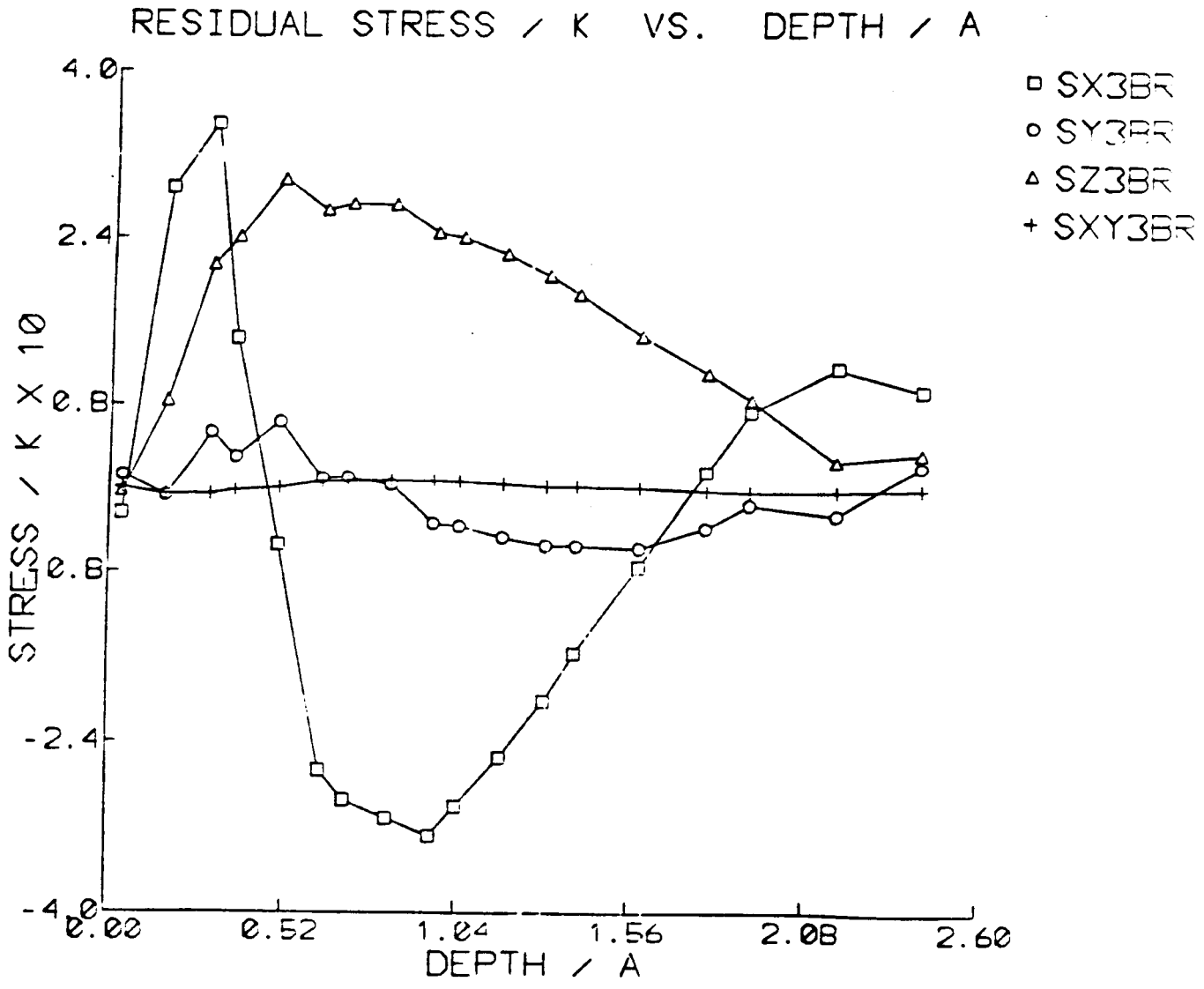

Figure 50. Variation of the normalized residual stresses, S3BR, with normalized depth for a heat flux input of 2.14×10^4 KW/m^2 (see Table 6).

ORIGINAL PAGE IS
OE POOR QUALITY

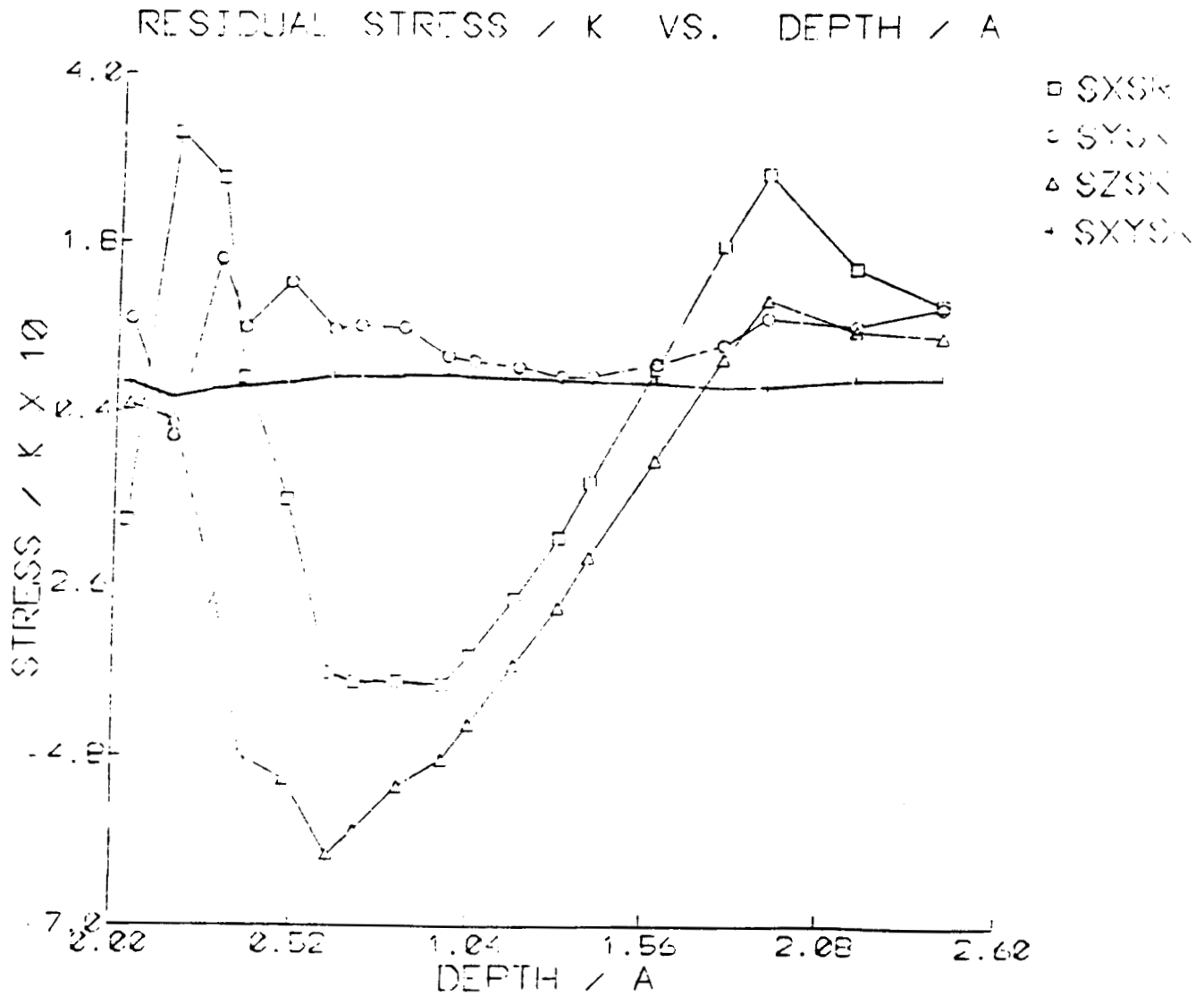

Figure 51. Variation of the normalized residual stresses, SSR, with normalized depth for zero heat flux input (see Table 6).

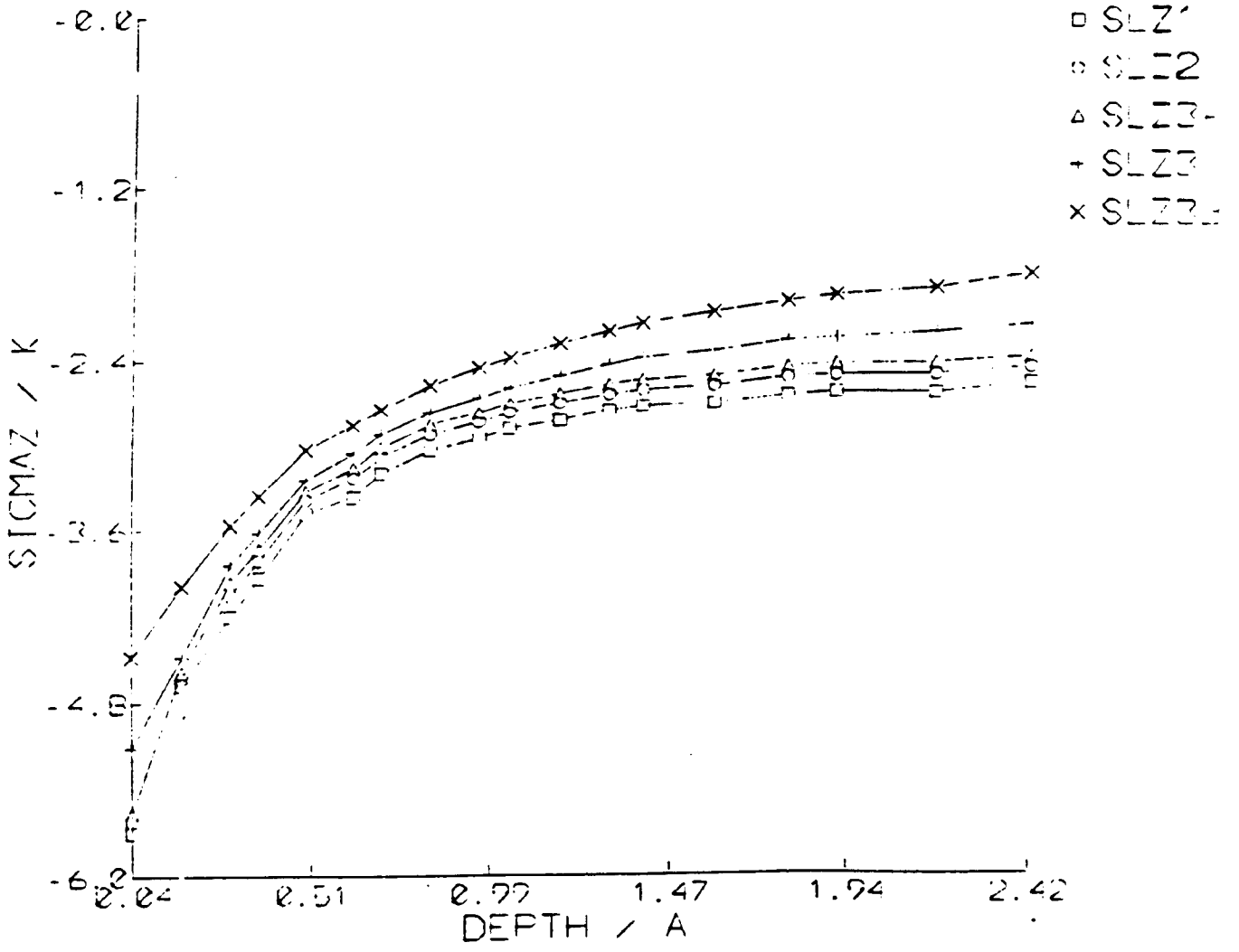

Figure 52. Variation of the normalized circumferential stress, SLZ, with normalized depth for different heat inputs (see Table 6).

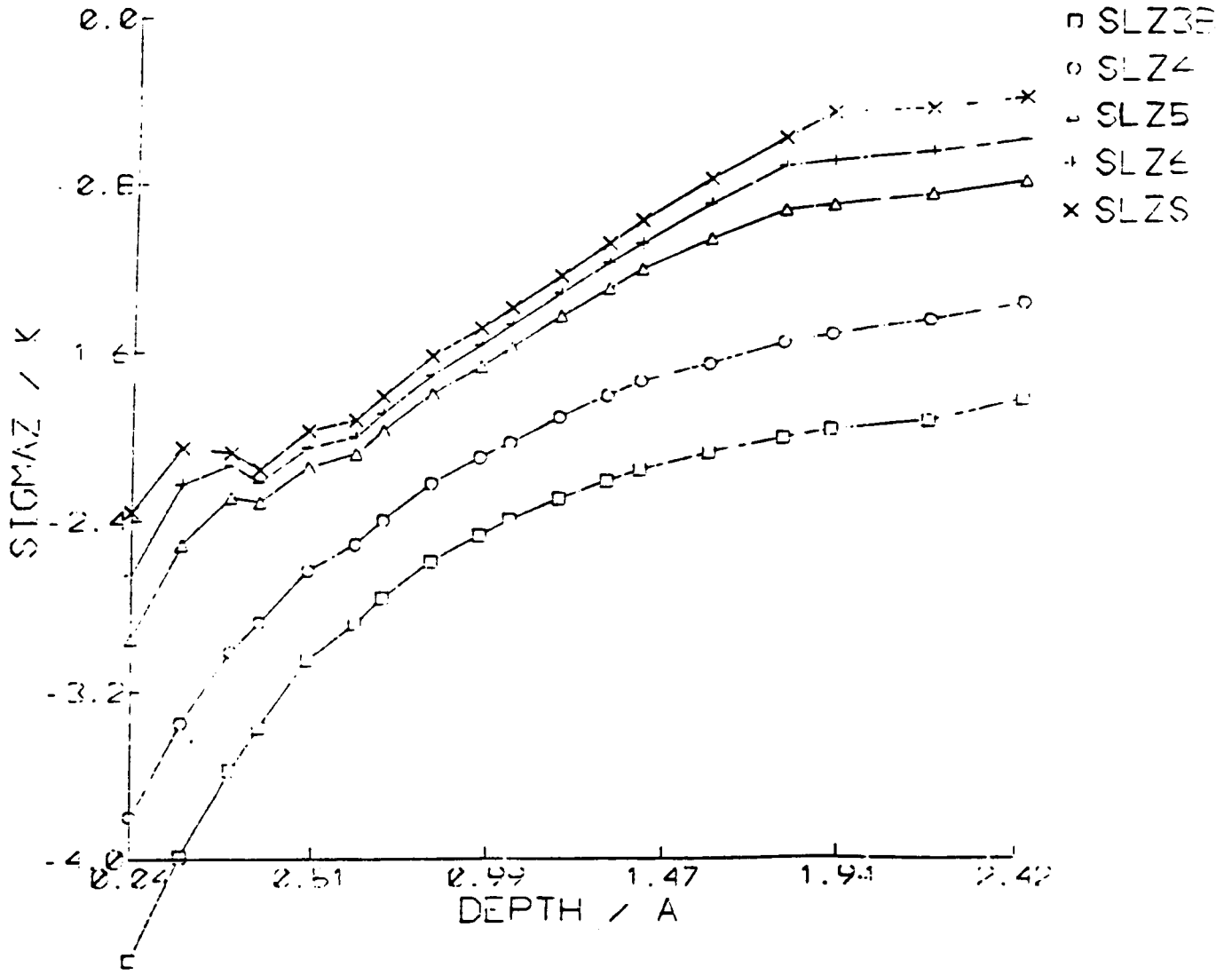

Figure 53. Variation of the normalized circumferential stress, SLZ, with normalized depth for different heat inputs (see Table 6).

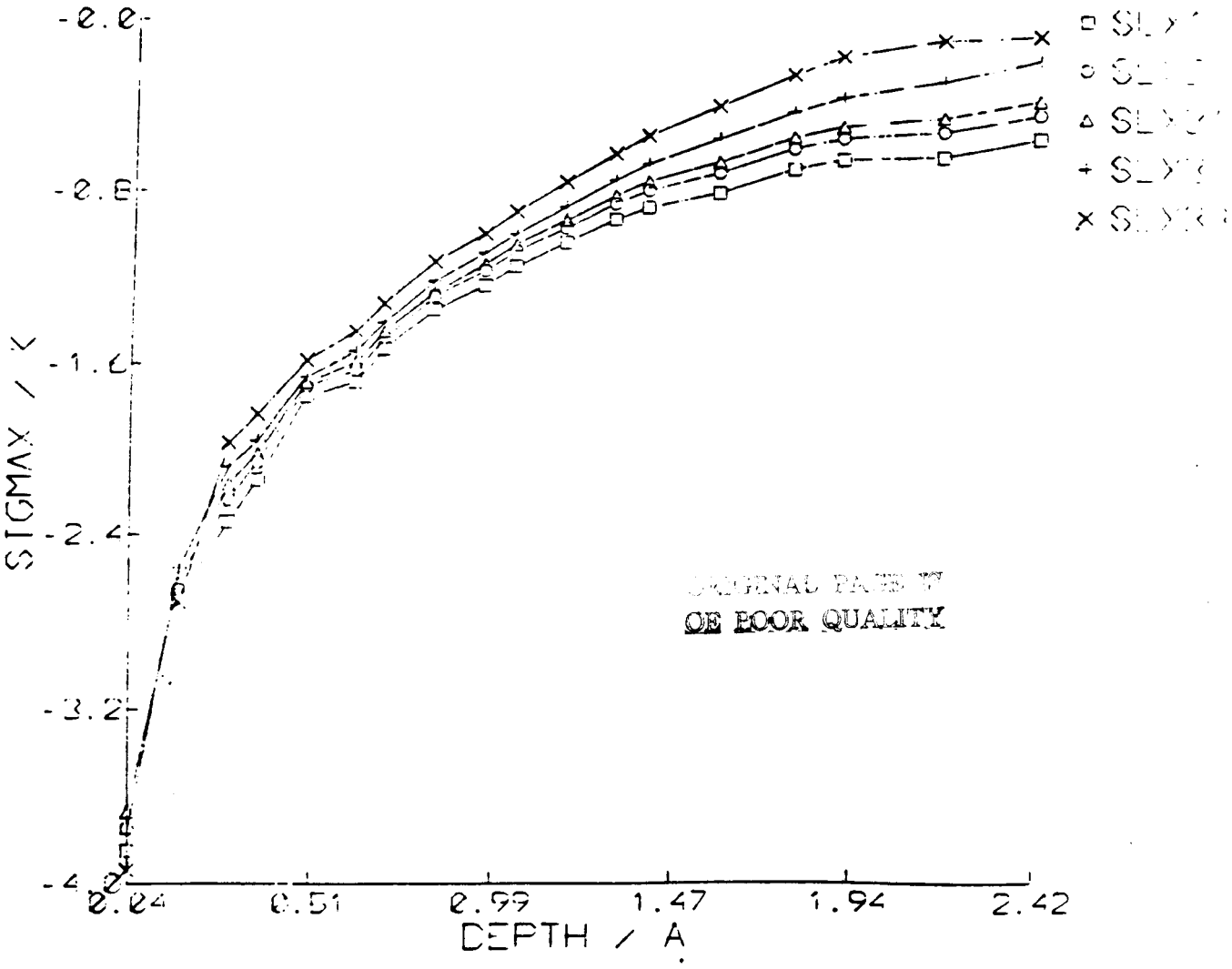

Figure 54. Variation of the normalized axial stress, SLX, with normalized depth for different heat inputs (see Table 6).

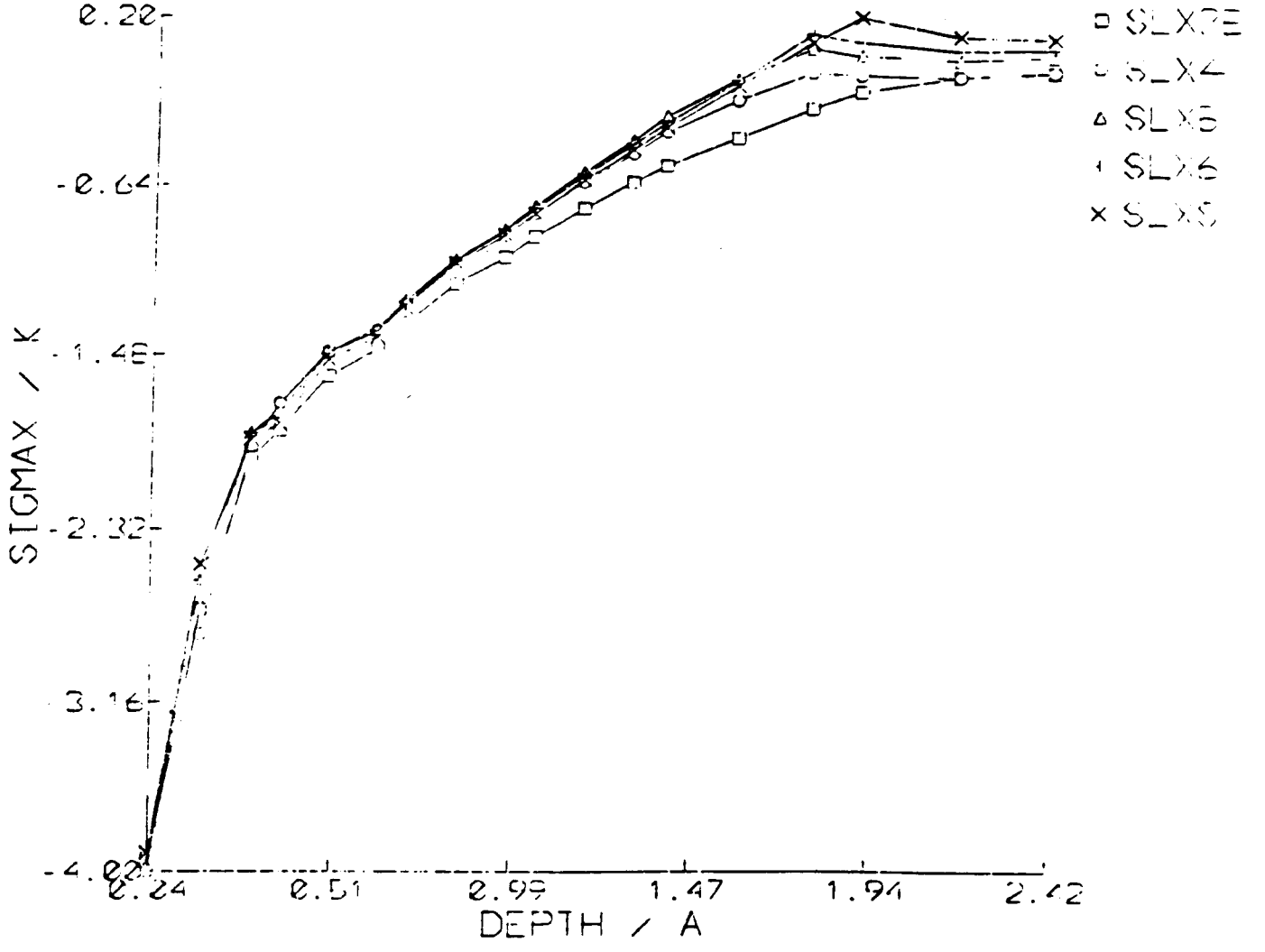

Figure 55. Variation of the normalized axial stress SLX, with normalized depth for different heat inputs (see Table 6).

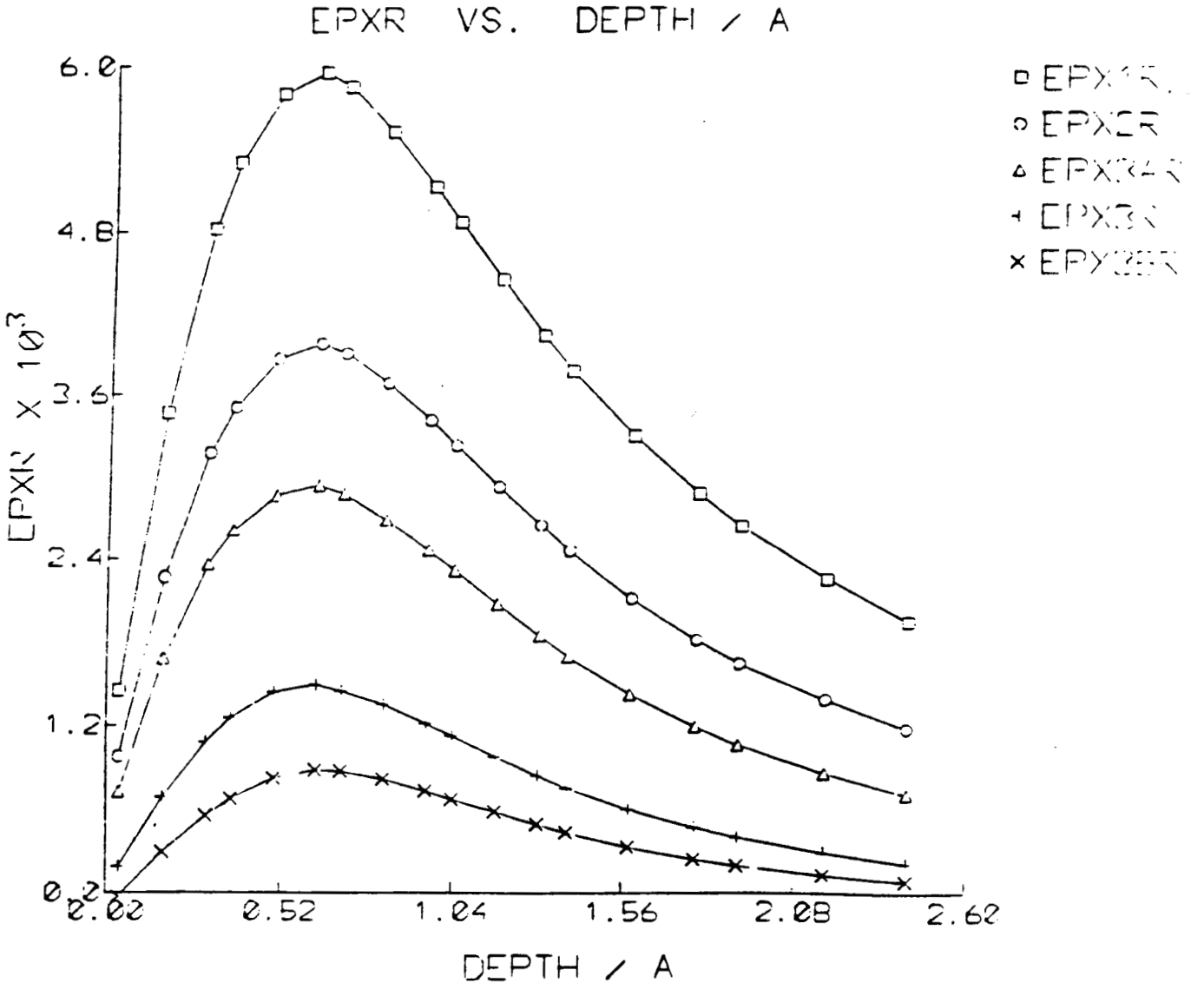

Figure 56. Variation of the normalized residual axial strain, EPXR, with normalized depth for different heat inputs (see Table 6).

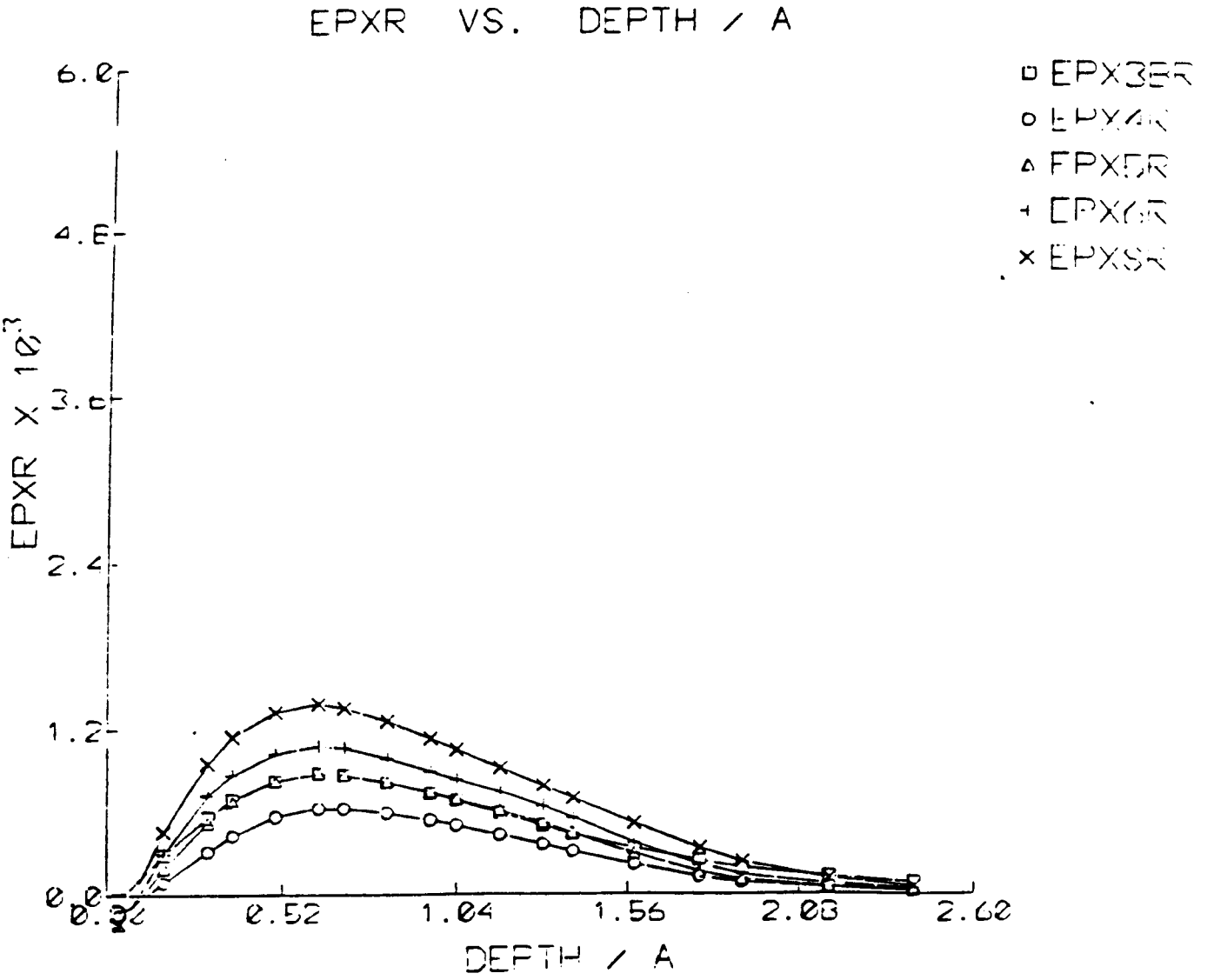

Figure 57. Variation of the normalized residual axial strain, EPXR, with normalized depth for different heat inputs (see Table 6).

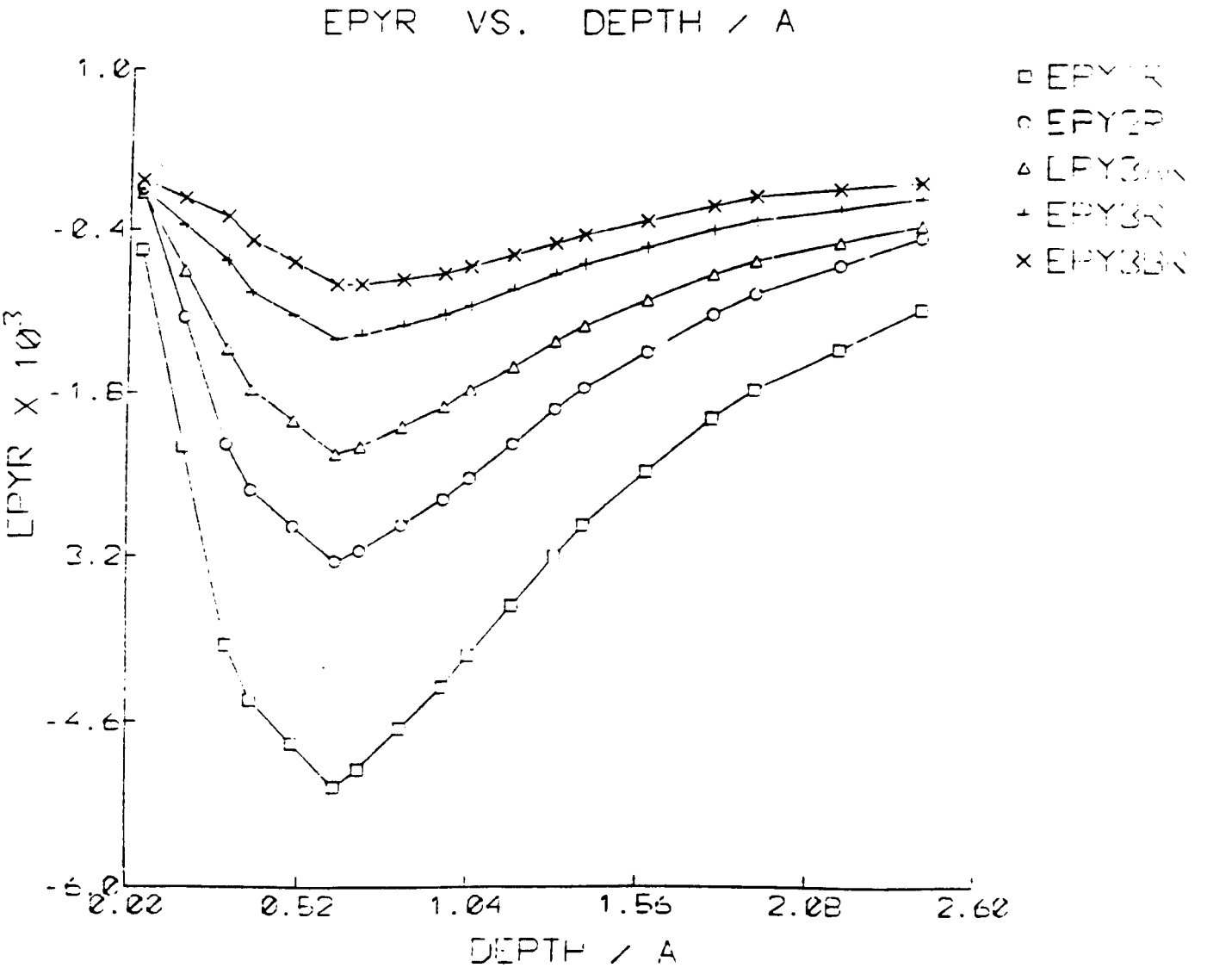

Figure 58. Variation of the normalized residual radial strains, EPYR, with normalized depth for different heat inputs (see Table 6).

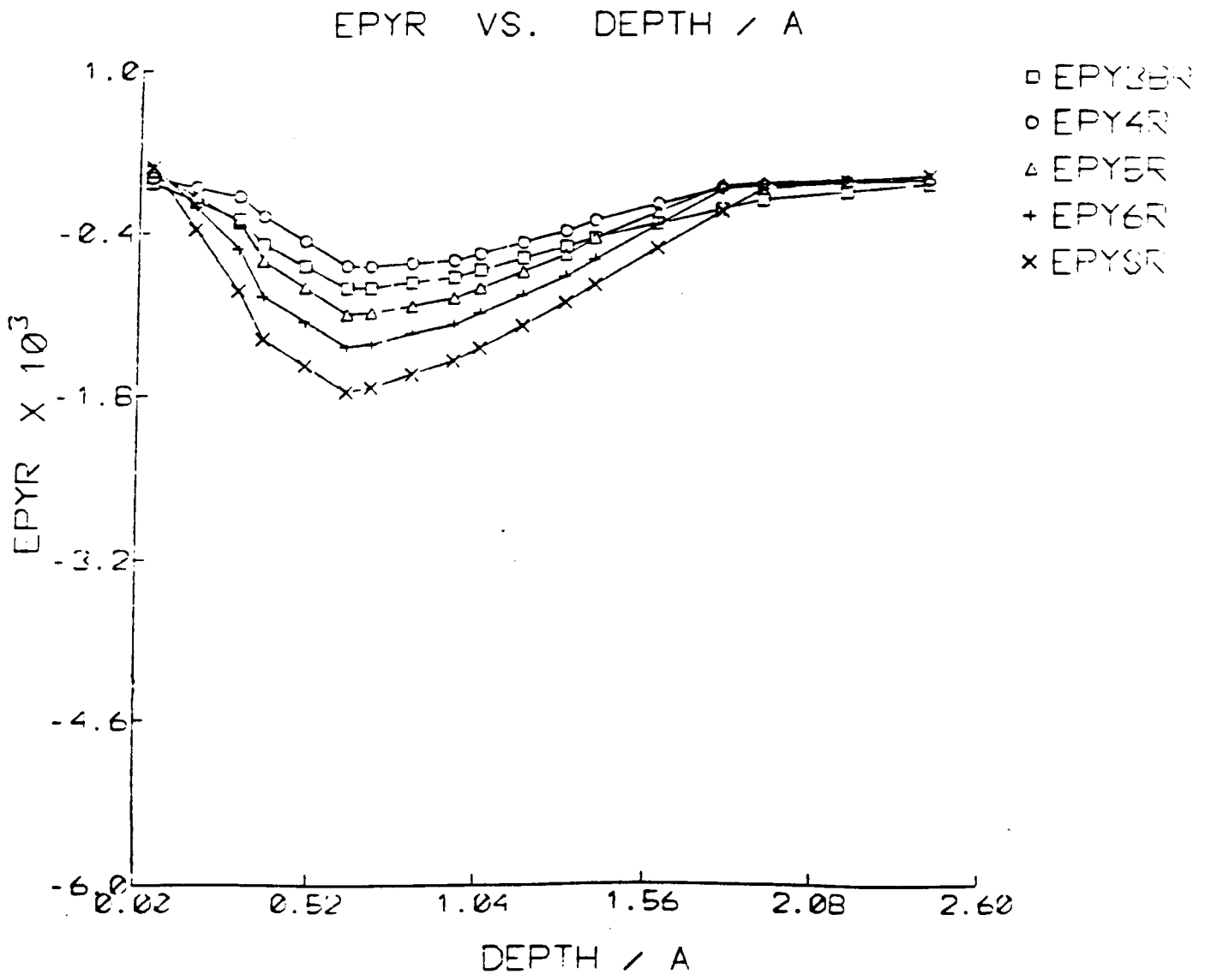

Figure 59. Variation of the normalized residual radial strains, EPYR, with normalized depth for different heat inputs (see Table 6).

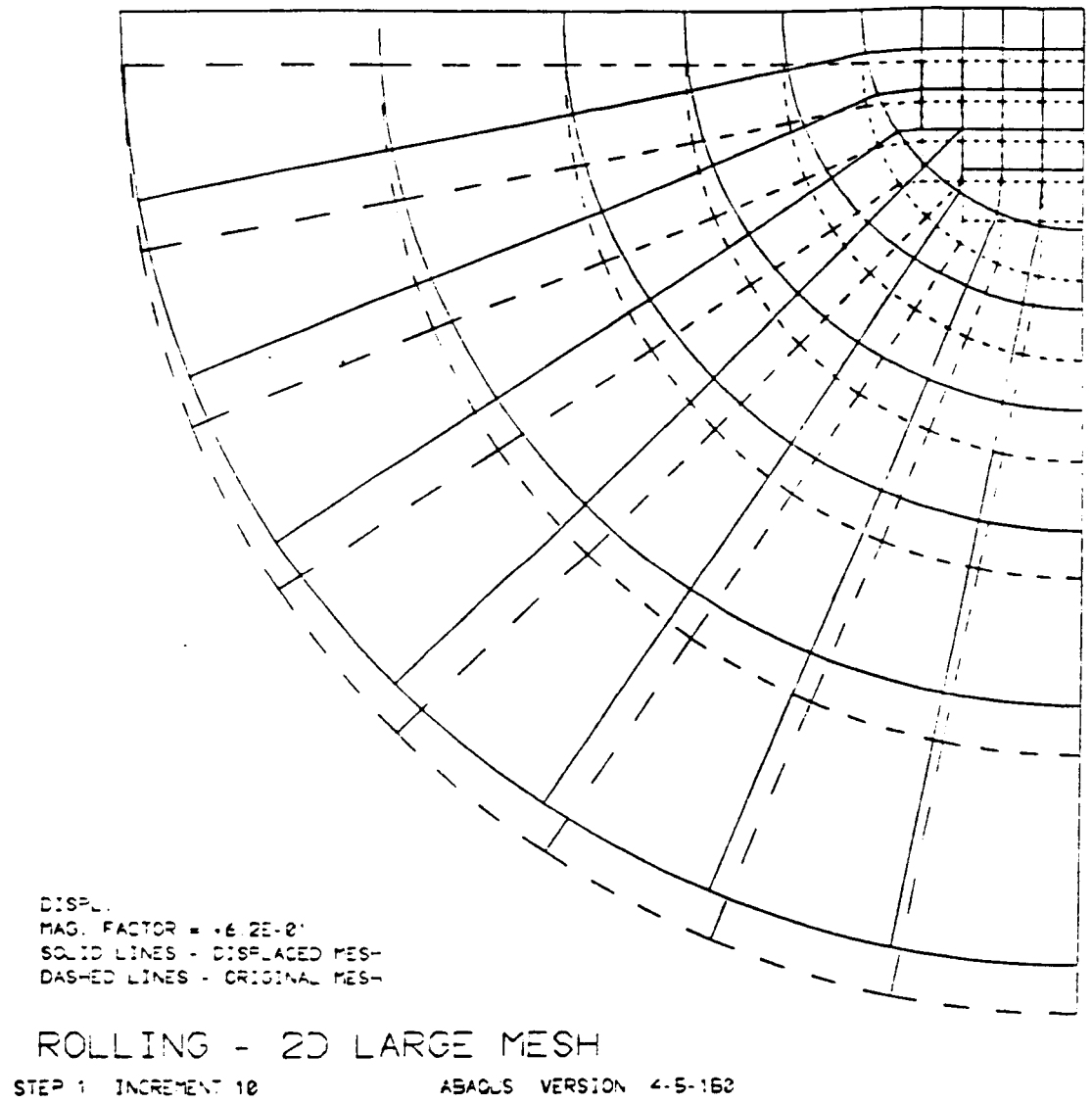

Figure 60. Displaced mesh (under load) for a heat flux input of 8.6 10^4 KW/m^2 (see Table 6). Solid lines - displaced mesh, dashed lines - original mesh. Mag. factor = 0.62.

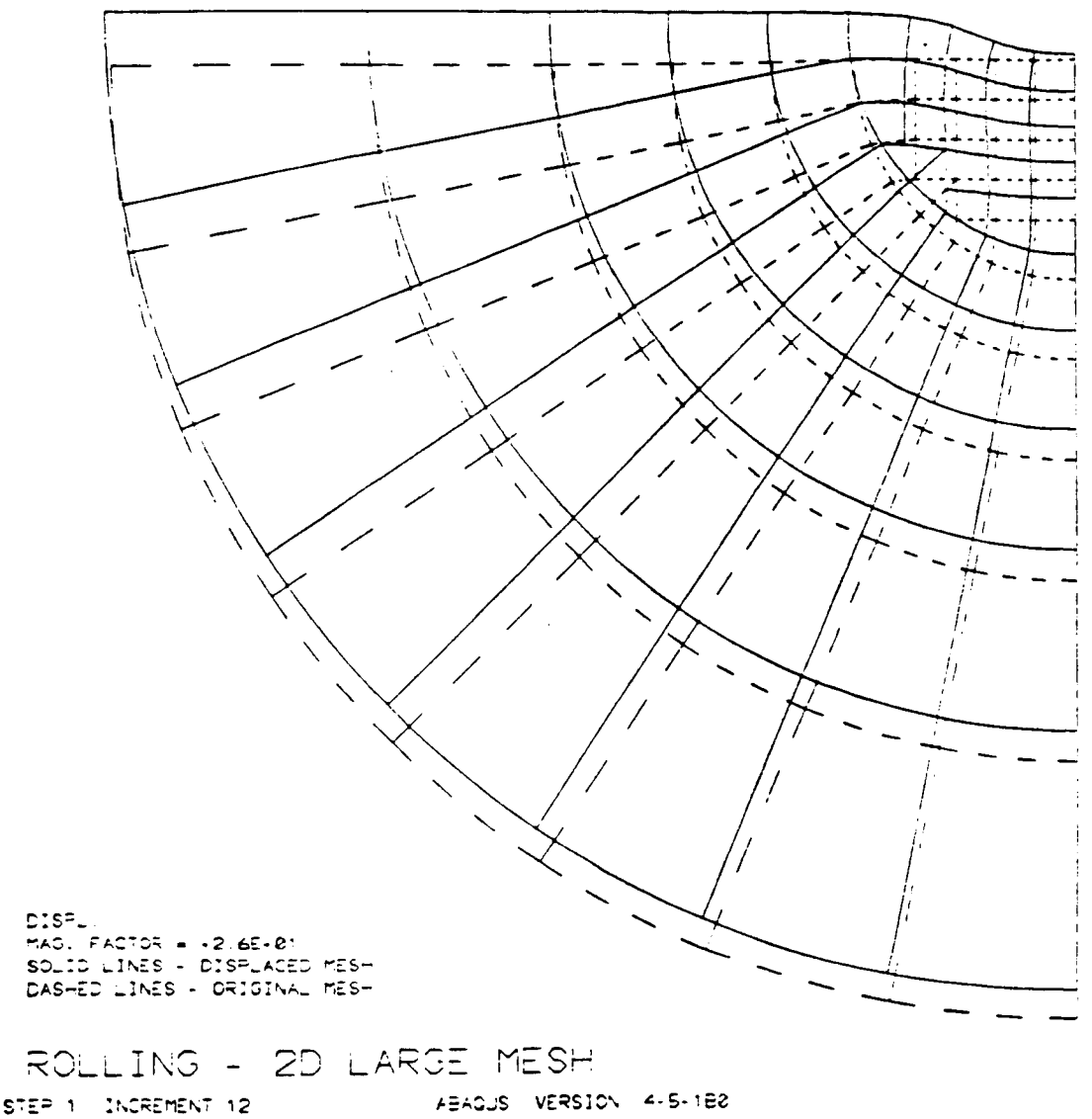

Figure 61. Displaced mesh (residual state) for a heat flux input of 8.6×10^4 KW/m^2 (see Table 6). Solid lines - displaced mesh, dashed lines - original mesh. Mag. factor = 26.0.

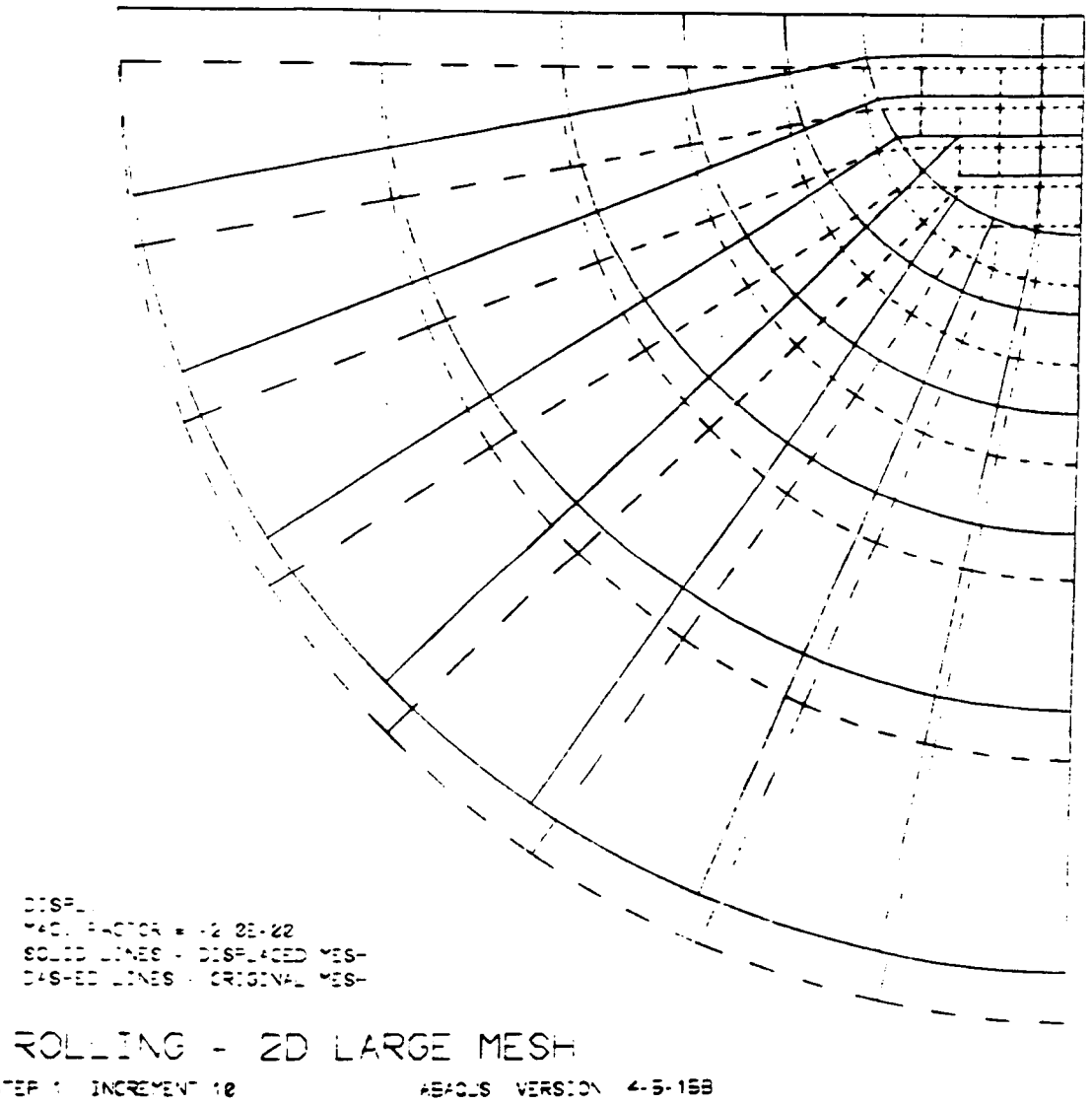

Figure 62. Displaced mesh (under load) for a heat flux input of 2.9×10^4 KW/m^2 (see Table 6). Solid lines - displaced mesh, dashed lines - original mesh. Mag. factor = 2.00.

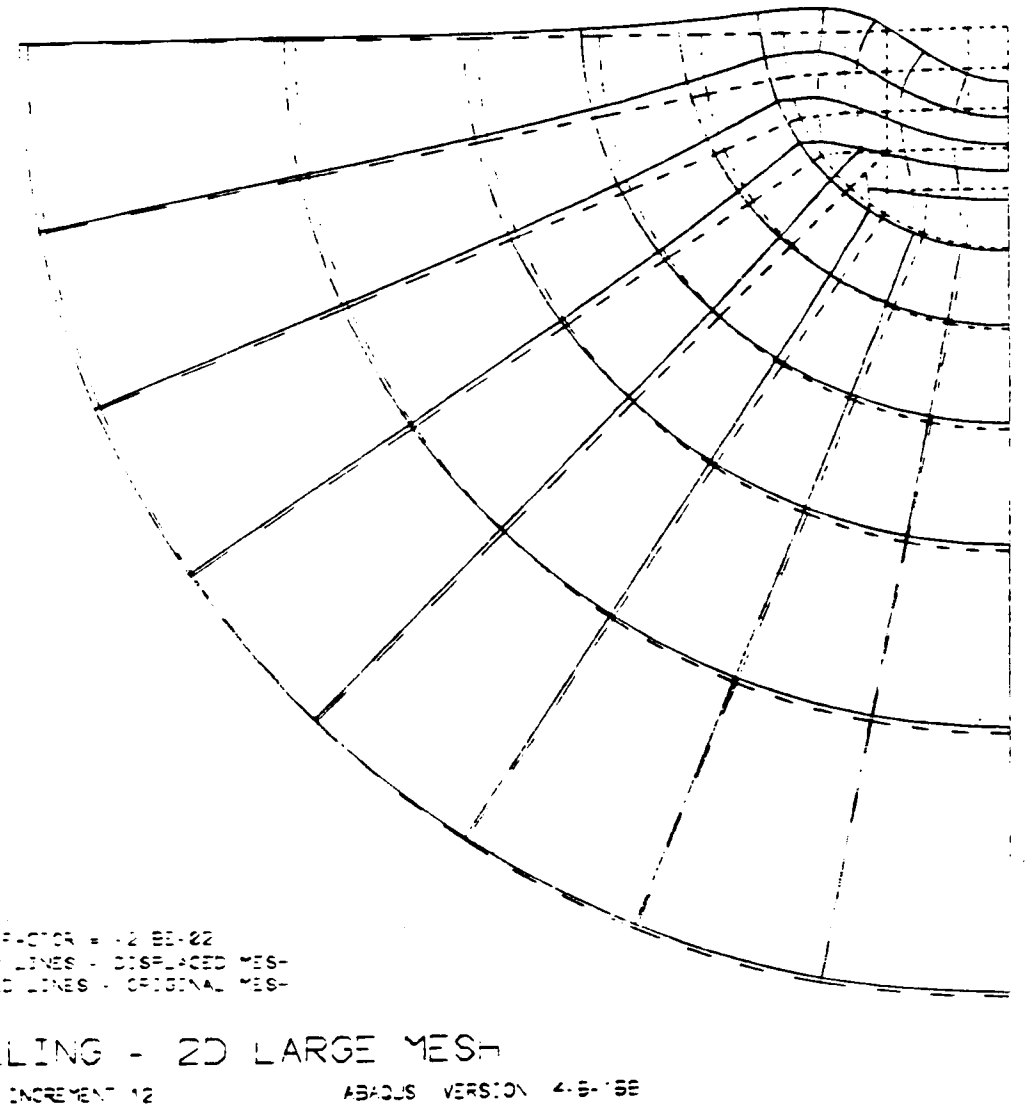

Figure 63. Displaced mesh (residual state) for a heat flux input of 2.9 x 10^4 KW/m^2 (see Table 6). Solid lines - displaced mesh, dashed lines - original mesh. Mag. factor = 280.

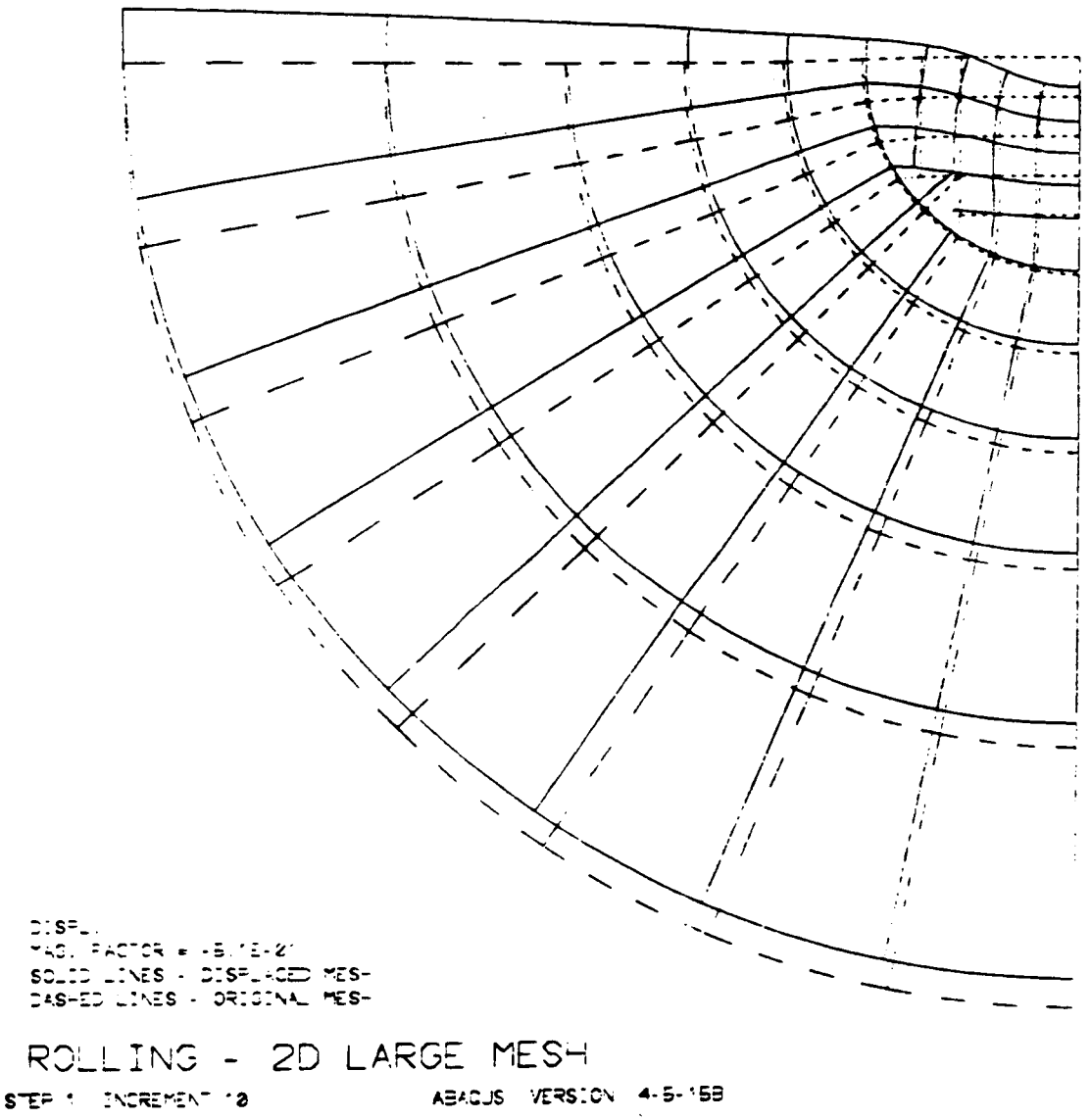

Figure 64. Displaced mesh (under load) for a heat flux input of 0.3×10^4 KW/m^2 (see Table 6). Solid lines - displaced mesh, dashed lines - original mesh. Mag. factor = 51.0.

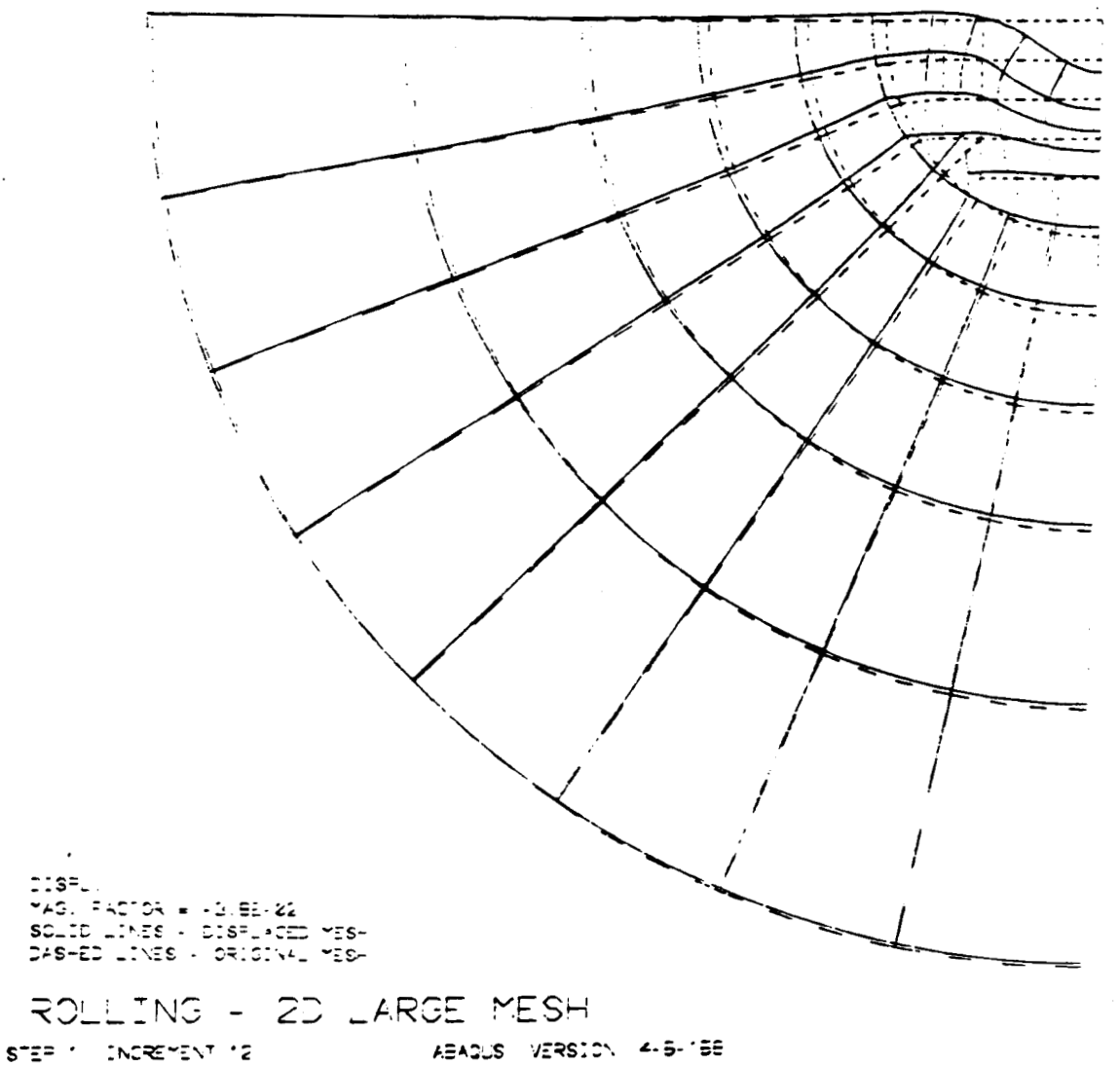

Figure 65. Displaced mesh (residual state) for a heat flux input of 0.3 x 10^4 KW/m^2 (see Table 6). Solid lines - displaced mesh, dashed lines - original mesh. Mag. factor = 380.

8. DISCUSSION

8.1 Cyclic Flow Properties of 440C Steel

The measurements reported here reveal that the elastic-linear-kinematic-hardening plastic (ELKP) representation offers a good description of the cyclic stress-strain behavior of 440C steel at room temperature and for the relatively long deformation times, i.e., 2s and the low strain rates, i.e., $\dot{\varepsilon} \simeq 10^{-3}s^{-1}$, employed in the cyclic torsion tests. It should also be clear that the values of σ_K and M appropriate for rolling contact service conditions, which encompass a wide range of temperatures[1,2] and much shorter deformation times, i.e., $\sim 10^{-5}$s, may be substantially different from the values used in the present calculations.

The torsion tests show that the 440C steel undergoes significant cyclic hardening, amounting to a 50% increase of σ_K in the first N = 600 cycles. The hardening is attributed to the cyclic-strain-induced-transformation of retained austenite. The premature failure of the torsion test pieces prevents the measurement of σ_K and M for the much larger number of contacts encountered in service. However, it is possible that the transformation proceeds more rapidly in the torsion test than under the compressively loaded contact since it produces a volume expansion. Consequently, it is not clear whether the ELKP-properties derived from short lived torsion tests apply to equally small or much larger numbers of rolling contacts. This issue deserves to be examined more closely since it affects the interpretation of the torsion test results. It is possible that the relatively short cyclic lives encountered in cyclic torsion - 10^4 times shorter than under rolling contacts producing similar strain amplitudes - are related to the absence of the high hydrostatic pressures produced by rolling contact.

The near end of life values of the ELKP material parameters of 440C steel: σ_K = 606 MPa, and M = 188 GPa are similar to those obtained for other hardened bearing steels[7]. They are regarded as the best estimate of the cyclic strength properties that govern the mechanical response to repeated rolling-sliding contact at room tempertaure.

8.2 Cyclic Crack Growth

The failure to produce stable, Mode II and Mode III cyclic crack growth in the hardened 440C torsion test pieces is attributed to a relatively low Mode I resistance. This makes it easier for the crack to extend in Mode I in spite of the less intense Mode I stress state. The fact that Mode II/Mode III growth was obtained in the same sample and for the same loading in a softer 4140 test piece, indicates that the Mode I resistance may degrade more with hardening than either the Mode II or Mode III. Alternatively, retained austenite decomposition at the tip of the crack identified earlier with cyclic hardening, and accompanying residual compression stresses, may interfere more with Mode II/III growth than with Mode I. This problem requires further work.

8.3 Rolling Contact Studies

The process of spall formation proposed here is very similar to the process observed by Shao et al.[12] and illustrated in Figure 66. The observations indicate that the increase in life obtained with the copper coated samples is associated with a shift defect assisted from surface-to-subsurface-initiation. The sensitivity of bearing life to surface imperfections has been emphasized before[49]. It is not clear whether the copper coated samples possessed better quality surfaces to begin with or whether the copper coating rendered the surface defects less harmful. Other questions about the spall process remain unanswered. The identity and location of the subsurface

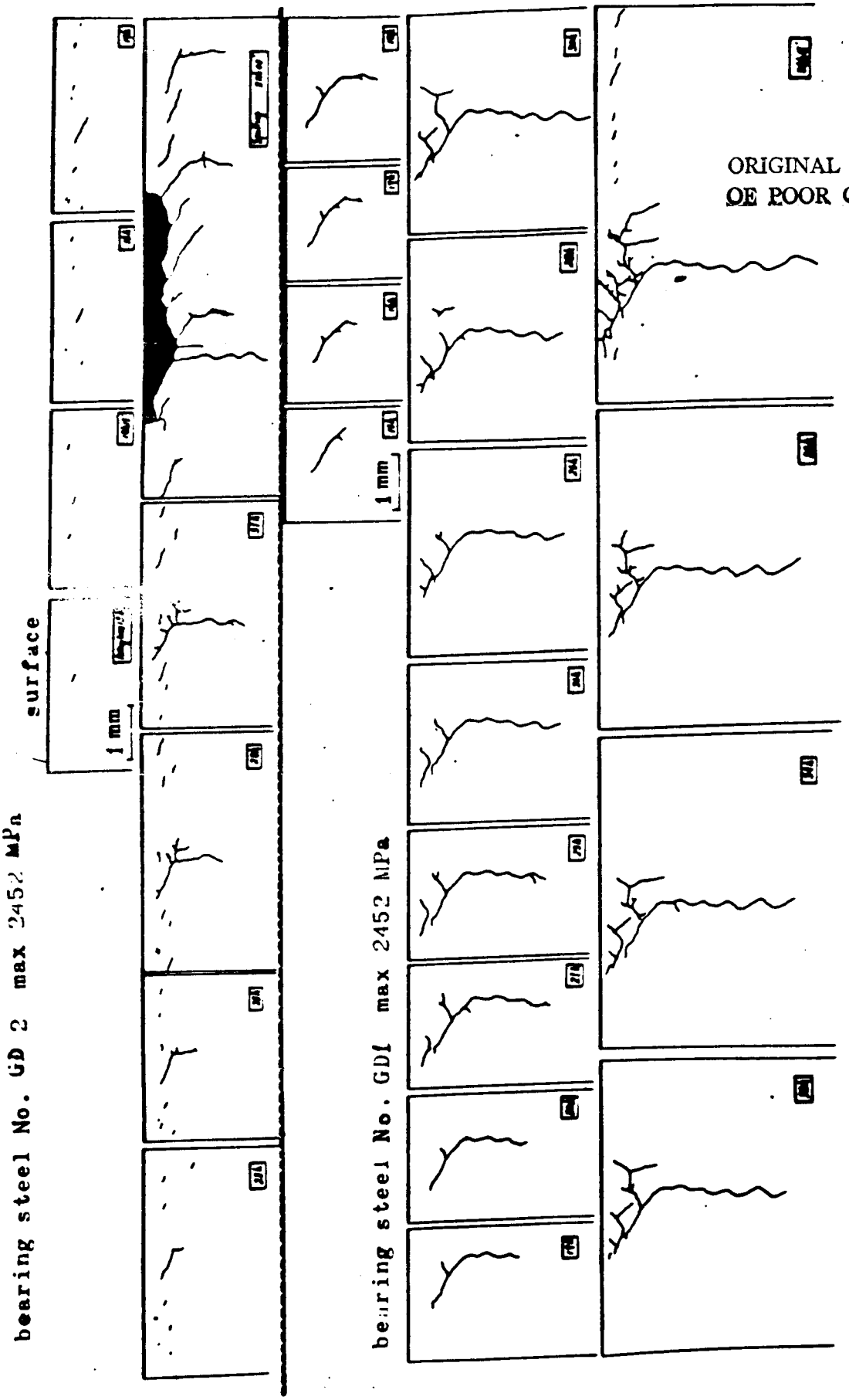

Figure 66. Rolling contact cyclic crack growth diagram for bearing steel.

initiation sites are unclear in this case. The conditions for crack initiation, the life remaining after initiation and the effects of the steep temperature and strength gradients arising from surface heating are not understood.

8.4 Finite Element Analyses

The finite element analyses reveal that the hardened 440C steel ELKP material properties greatly reduce the plastic strains generated by rolling-plus-sliding contact. The peak, half equivalent strain range obtained here: $\Delta\bar{\varepsilon}^p/2 = 0.00025$ (for $p_o/k_k = 4.5$, $T/N = 0.2$, $\mu = 0.2$), is less than 1/10 the value: $\Delta\bar{\varepsilon}^p/2 = 0.0032$ reported by Ham et al.[20] for elastic-perfectly-plastic (EPP) behavior for the same contact condition. The relatively large radial plastic strain range, reported by Ham et al. at the surface: $\Delta\varepsilon_x^p = 0.0022$, is absent for ELKP behavior. The large continuing forward flow of $\Delta\delta_x = 20$ μm/contact displayed by the EPP model is completely absent in the present case. The large changes are attributed to the unidirectional character of the strains produced by sliding which is obviated by kinematic hardening and by the large value of the plastic modulus. Thus, the results for rolling-plus-sliding are close to those for pure rolling for kinematic hardening. The calculations assume that the material retains its kinematic character in the presence of large mean stresses -- a point that requires further study. It should be noted that the elimination of forward flow by ELKP-behavior has been confirmed for pure rolling. Another complication arises from the fact that the residual stresses are determined by the first one or two contacts and depend on the shape of the hysteresis loop at the onset of cycling when the material progressively hardens. The values obtained here probably understate the actual values since they are derived from the end-of-life ELKP properties. This issue is discussed more fully in Reference 7.

The cyclic strain peaks are obtained at relative depths of $y/w = 0.65$ which correspond with the depths of spall initiation in 2 cases[50]. While the cyclic plastic strains produced by contact are small in the absolute sense, they are relatively large considering that comparable equivalent strain ranges, $0.0005 \leq \Delta\bar{\varepsilon}^p/2 \leq 0.002$, produce very short cyclic lives, e.g., 300 N 600 cycles in cyclic torsion. The fact that rims subjected to the same cyclic strains under contact conditions survive $N = 10^6$ to $N = 10^7$ contact cycles (see Section 4) suggests that crack initiation and growth are inhibited by the high hydrostatic pressures accompanying the contact. The finite element model described in Section 6 fails to treat two consequences of the high heat generation rates encountered in service: (1) high thermal stresses and (2) the degrading of the cyclic strength in the high temperature regions. These effects are dealt with in a preliminary way by the steady state finite element model described in Section 7. However, the thermal effects need to be incorporated into the transient model.

Finally, it should be noted that 2 deformed layers are produced by rolling-plus-sliding contact. These are shown schematically in Figure 67. One involves the macro contact width and extends to a depth $2w_m \sim 10^3$ μm; the other involves the asperity contact width and extends to a depth $2w_a \sim 10$ μm. Strains will be more intense in the latter case if the asperity peak pressure is greater than p_o, the macrovalue. The shallow asperity layer may be important in the case of the 440C steel where cracks have been observed to initiate very close to the rim surface.

8.5 Finite Element Model of Frictional Heating

The temperature-displacement-coupled finite element model of the frictionally heated contact has many deficiencies. It is more properly viewed as a model of a stationary, heat generating indent. However, the finding that

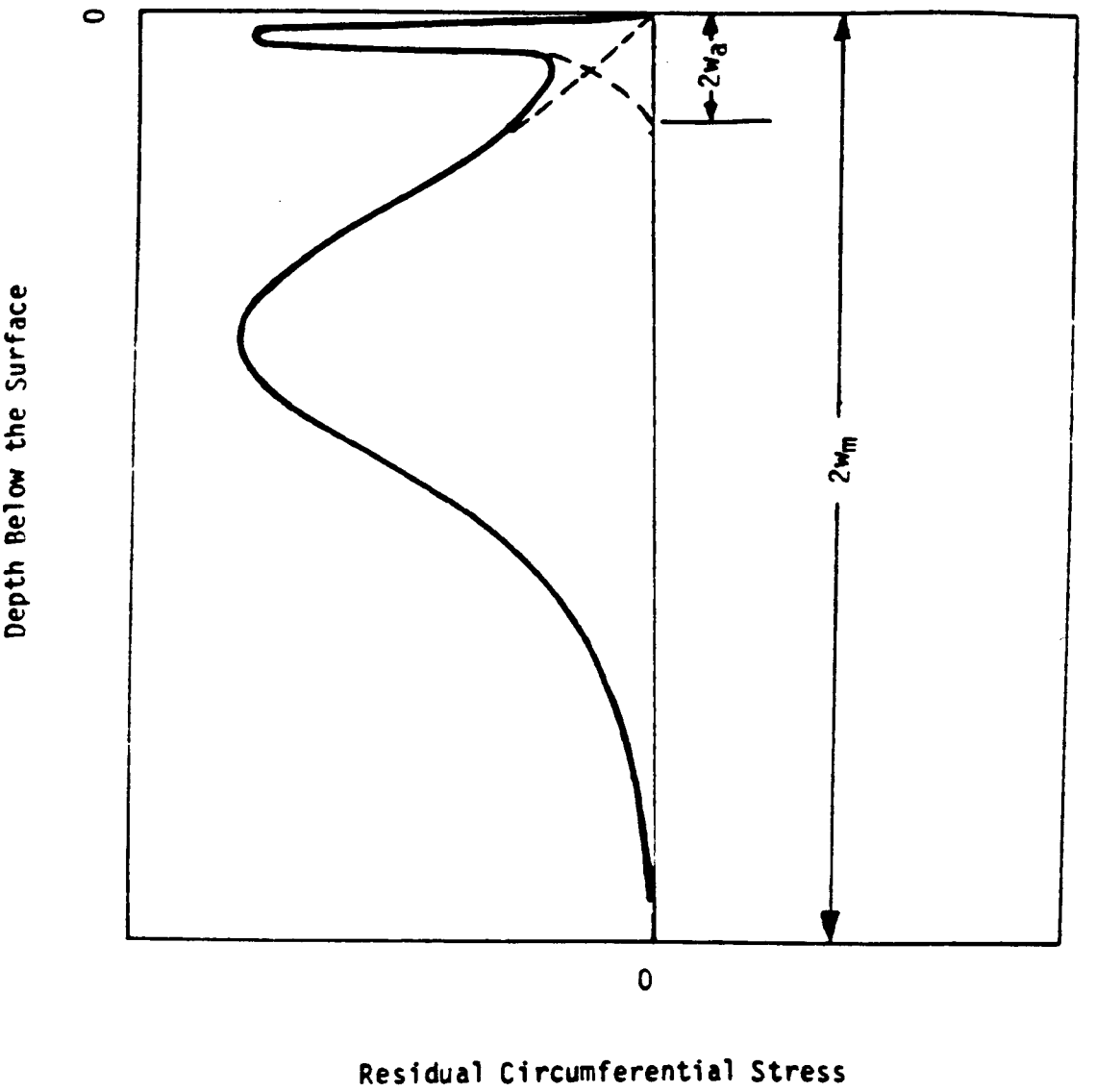

Figure 67. Schematic representation of the contributions of the asperity and macro contact to the residual stress distribution in the rim. The quantities $2w_a$ and $2w_m$ are the asperity and the macro contact widths, respectively.

very large residual tensile stresses: σ_x^R = 345 MPa and σ_z^R = 1200 MPa are generated at the surface is undoubtedly valid for the translating contact as well. The residual tensile stresses are a consequence of the steep temperature gradient and attending compressive thermal stresses under the contact that produce plastic compression in the x- and z-directions. On cooling, elastic, and possibly plastic, tension compensate for the thermal contraction. The cyclic superposition of compression by the translating contact can then produce a fluctuating tension and potential Mode I crack driving force that accelerate crack initiation and cyclic crack growth. The effects may be accentuated by the softening of the material at the elevated temperatures. More realistic calculations of this type employing the translating finite element contact model of Section 6 are possible and may be helpful in setting limits on the allowable levels of heat generation.

9. CONCLUSIONS

(i) The room temperature, cyclic stress-strain hysteresis loops of hardened 440C steel subjected to constant plastic strain amplitude cyclic torsion have been examined for the plastic strain amplitudes: $0.0005 \leq \Delta\bar{\varepsilon}^P/2 \leq 0.002$ produced by rolling-plus-sliding-contact. The characteristics and shapes of the loops are well represented by the elastic-linear-kinematic-hardening-plastic (ELKP) idealization.

(ii) The 440C steel undergoes substantial cyclic hardening under these conditions and fractures after from $N \simeq 300$ cycles to $N \simeq 600$ cycles. The values of the 3 ELKP material parameters that describe the near end-of-life cyclic stress-strain behavior are: (a) the elastic tension modulus ($E = 207$ GPa), (b) the kinematic yield strength $\sigma_k = 1050$ MPa (or shear yield strength $k_k = \sigma_k/\sqrt{3}$), and the plastic modulus $M = 188$ GPa.

(iii) Elasto-plastic finite element analyses of repeated rolling-plus-sliding contact have been performed for the room temperature ELKP-properties of 440C steel. The calculations treat Hertzian pressures in the range $2.5 \text{ GPa} \leq p_o \leq 3.64 \text{ GPa}$ and full slip with a coefficient of friction $\mu = 0.2$. The results show that the contacts produce peak cyclic strain ranges and residual stresses of $0.00025 \leq \Delta\varepsilon^{P'}/2 \leq 0.001$ and $-20 \text{ MPa} \leq \sigma^R \leq -35 \text{ MPa}$ that are similar to the values calculated for pure rolling, but much smaller than the strains and stresses calculated for rolling-plus-sliding with elastic-perfectly-plastic (EPP) material behavior.

(iv) The analysis locates the peak strain activity at the relative depth, $y/w = 0.65$ ($2w$ is the contact width), where spall initiation has been observed.

(v) In the cases treated, the energy dissipated as heat by plastic deformation is from 3% to 15% of the energy dissipated at the surface by friction.

(vi) A coupled, temperature-displacement, elasto-plastic finite element analysis of the effects of frictional heating under the contact was performed. The calculations reveal that the local heating produces high levels of residual tension: $\sigma_x^R \simeq 350$ MPa and $\sigma_z^R \simeq 1200$ MPa after the contact is unloaded and cooled. The superposition of compression by the translating contact can then produce a fluctuating tension and Mode I crack driving force that can promote crack initiation and crack growth.

(vii) The spalls generated in 440C steel bearing surfaces in a 3 ball/rod testing machine display the classical, V-shaped, loose flap produced by a small inclination, near surface crack growing into the rim.

(viii) It appears that the spalls observed in uncoated samples are initiated at the surface by surface imperfections. The spalls in longer-lived copper coated samples initiate below the surface.

(ix) The task of measuring the Mode II/Mode III cyclic crack growth resistance of hardened 440C steel is complicated by a relatively low Mode I crack growth resistance. Cracks from defects subjected to Mode II/Mode III in cyclic torsion prefer to extend in Mode I in spite of the low Mode I driving force.

ACKNOWLEDGEMENTS

The authors wish to thank B. Bhat and R. Parr of the NASA Marshall Space Flight Center for their support and encouragement. They also wish to thank Mr. R. Thom of the NASA Marshall Space Flight Center for providing the spalled samples for examination. They also wish to acknowledge the assistance of Q. Chen and K. Kim with the torsion tests. They are grateful for the permission to use the finite element code ABAQUS provided by Hibbitt, Karlsson and Sorensen, Inc. Finally they wish to thank C. Thompson for her contributions to the manuscript.

REFERENCES

1. B. N. Bhat and F. J. Dolan, "Past Performance Analysis of HPOTP Bearings," NASA TM-82470, March 1982.

2. B. N. Bhat and F. J. Dolan, "Analysis of Cryogenic Turbopump Bearing Service Life," Proc. Structures, Structural Dynamics and Materials Conference, May 1983.

3. R. E. Maurer and R. A. Pallini, "Computer-Aided Selection of Materials for Cryogenic Turbopump Bearings," ASLE Preprint '85 AM4E-1.

4. D. K. Chaudhuri and Ravi Verma, "A Study of Wear Processes in 440C Ball Bearings Used in the HPOTP of the SSME," Oct. 31, 1986.

5. H. K. Lorosch, "The Life of the Rolling Bearing under Varying Loads and Environmental Conditions," Ball and Roller Bearing Eng'g, 1981, Vol. 1, p. 17.

6. V. Bhargava, G. T. Hahn, G. Ham, S. Kulkarni, and C. A. Rubin: "Influence of Kinematic Hardening on Rolling Contact Deformation," Proc. 2nd Int. Symp. on Contact Mechanics and Rail/Wheel Systems, Kingston, RI, July, 1986.

7. G. T. Hahn, V. Bhargava, C. A. Rubin, Q. Chen and K. Kim: "Analysis of the Rolling Contact Residual Stresses and Cyclic Plastic Deformation of an SAE 52100 Steel Ball Bearing," ASME J. of Tribology, (to be published).

8. J. E. Merwin and K. L. Johnson, "An Analysis of Plastic Deformation in Rolling Contact," Proc. Inst. Mech. Engs., Vol. 177, 1963, p. 667.

9. K. L. Johnson and J. A. Jefferis, "Plastic Flow and Residual Stresses in Rolling and Sliding Contact," Proc. Symp. on Fatigue in Rolling Contact, Inst. Mech. Engr., London, 1963, papers.

10. H. Ziegler, "A Modification of Prager's Hardening Rule," Quarterly App. Math, 1959, Vol. 17, p. 55.

11. V. Bhargava, G. T. Hahn and C. A. Rubin, "Analysis of Cyclic Crack Growth in High Strength Roller Bearings," Theory and App. Fracture Mechanics, Vol. 5, No. 1, 1986, pp. 31-38.

12. E. Shao, X. Huang, C. Wang, Y. Zhu and Q. Chen, "A Method of Detecting Rolling Contact Crack Initiation and the Establishment of Crack Propagation Curves," ASLE Preprint, 87-AM-4E-2, 1987.

13. S. D. O'Regan, G. T. Hahn, and C. A. Rubin, "The Driving Force for Mode II Crack Growth Under Rolling Contact," Wear, 101 (1985) pp. 333-346.

14. T. S. Lei, V. Bhargava, G. T. Hahn and C. A. Rubin, "Stress Intensity Values for Small Cracks in the Rim of Disks and Rings Subjected to Rolling Contact," ASME J. of Tribology, Vol. 108, pp. 540-544, Oct., 1986.

15. Q. Chen, G. T. Hahn, C. A. Rubin and V. Bhargava, "Influence of Residual Stresses on the Rolling Contact K_{II} Crack Growth Driving Force for High Strength Bearing Steel," (to be published).

16. N. Soda and T. Yamamoto, "Effect of Tangential Traction and Roughness on Crack Initiation/Propagation During Rolling Contact," ASLE Trans., 1981 Vol. 25, pp. 198-206.

17. A. P. Voskamp, "Material Response to Rolling Contact," J. Tribology, 1988, Vol. 107, pp. 359-366.

18. V. Bhargava, G. T. Hahn, and C. A. Rubin, "An Elastic-Plastic Finite Element Model of Rolling Contact, Part I: Analysis of Single Contacts," ASME J. Applied Mechanics, Vol. 52, 1985, p. 67.

19. V. Bhargava, G. T. Hahn, and C. A. Rubin, "An Elastic-Plastic Finite Element Model of Rolling Contact, Part II: Analysis of Repeated Contacts," ASME J. Applied Mechanics, Vol. 41, 1985, p. 75.

20. G. Ham, G. T. Hahn, and C. A. Rubin, "Finite Element Analysis of Repeated Two Dimensional Rolling-Sliding Contacts," J. of Tribology, to be published.

21. S. Kulkarni, G. Hahn, C. Rubin and V. Bhargava, (unpublished research).

22. J. R. Barber, "Some Thermoelastic Contact Problems Involving Frictional Heating," The Quarterly Journal of Mechanics and Applied Mathematics, 1976, p. 7.

23. J. R. Barber, "The Solution of Heated Punch Problems by Point Source Methods," Int. J. Engng. Sci., Vol. 9, 1971, pp. 1165-1170.

24. B. B. Mikic, "Thermal Contact Conductance: Theoretical Considerations," Int. J. Heat Mass Transfer, Vol. 17, 1974, pp. 205-214.

25. J. R. Barber, "The Effect of Thermal Distortion on Constriction Resistance," Int. J. Heat Mass Transfer, Vol. 14, 1969, pp. 751-766.

26. J. R. Barber, "Thermoelastic Instabilities in the Sliding of Conforming Solids," Proc. Roy. Soc., A-312, 1969, pp. 321-394.

27. J. R. Barber, "Distortion of the Semi-Infinite Solid due to Transient Surface Heating," Int. J. Mech. Sci., Vol. 14, 1972, pp. 377-393.

28. C. Panek and J. Dundurs, "Thermoelastic Contact Between Bodies with Wavy Surfaces," Transactions of the ASME, Vol. 46, Dec., 1979, p. 854.

29. J. R. Barber, "Some Implications of Dundurs' Theorem for Thermoelastic Contact and Crack Problems," Journal Mechanical Engineering Science, Vol. 22, No. 5, 1980, p. 229.

30. M. Comninou and J. Dundurs, "On the Barber Boundary Conditions for Thermoelastic Contact," J. of App. Mech., Vol. 46, Dec., 1979, p. 849.

31. M. Comminou, M. Dundurs, and J. R. Barber, "Planar Hertz Contact with Heat Conduction," J. of App. Mech., Vol. 48, Sept. 1981, p. 549.

32. J. R. Barber, "Indentation of the Semi-Infinite Elastic Solid by a Hot Sphere," Int. J. Mech. Sci., Vol. 15, 1973, p. 813-819.

33. F. F. Ling and V. C. Mow, "Surface Displacement of a Convective Elastic Half-Space Under an Arbitrarily Distributed Fast-Moving Heat Source," J. of Basic Engineering, Sept. 1965, p. 729.

34. D. A. Hills and J. R. Barber, "Steady Sliding of A Circular Cylinder over a Dissimilar Thermally Conducting Half-Plane," Int. J. Mech. Sci., Vol. 28, No. 9, 1986, p. 613-622.

35. M. V. Korovchinski, "Plane-Contact Problem of Thermoelasticity During Quasi-Stationary Heat Generation on the Contact Surfaces," J. of Basic Engineering, Dec., 1965, p. 811.

36. V. C. Mow and H. S. Cheng, "Thermal Stresses in an Elastic Half Space Associated with an Arbitrarily Distributed Moving Heat Source," Z.A.M.P., Vol. 18, 1967, p. 501.

37. M. R. Johnson, R. E. Welch, and K. S. Yeung, "Analysis of Thermal Stresses and Residual Stress Changes in Railroad Wheels caused by Severe Drag Braking," J. of Engineering for Industry, Feb. 1977, p. 19.

38. H. R. Wetenkamp and R. M. Kipp, "Thermal Damage and Railraod Stresses in a 33-Inch Railroad Car Wheel," J. of Engineering for Industry, August, 1978, Vol. 100, p. 363.

39. A. T. Hopper, S. G. Sampath, and R. B. Stonesiper, "The Elastic Finite Element Analysis of a CH-36 Railcar Wheel Under Mechanical and Thermal Loads," Track/Train Dynamics and Design, Pergamon Press, Eds. G. J. Moyar, W. D. Pilkey, and B. F. Pilkey, 1978.

40. H. R. Wetenkamp and R. M. Kipp, "Safe Thermal Loads,"

41. H. R. Larson, J. M. Coughlin, M. R. Halsy and T. M. Rusin, "Experimental Verification of Computer-Predicted Temperatures and Elastic Thermal Strains in Railroad Wheels,"

42. B. N. Bhat and P. J. Dolan, "Analysis of Cryogenic Turbopump Bearing Service Life," 24th Structures, Structural Dynamics and Materials Conference, May 1983, Lake Tahoe, Nevada.

43. R. P. Mavris and R. A. Pallini, "Computer-Aided Selection of Materials for Cryogenic Turbopump Bearings," 40th ASLE Annual Meeting, May 1985, Las Vega, Nevada.

44. S. Z. Newman, "FEM Model of 3-D Transient Temperature and Stress Fields in Welded Plates," Ph.D. Dissertation, Carnegie-Mellon university, April, 1986.

45. G. Dumas and C. N. Baronet, "Elastic-plsatic Indentation of a Half-Space by an Infinitely Long Rigid Circular Cylinder," Int. J. Mech. Sci., Vol. 13, 1971, pp. 519-530.

46. G. Rydholm, "On Inequalities and Shakedown in Contact Problems," Linkoping Studies in Science and Technology, 1981.

47. Douglas Grover, "A Ball-Rod Rolling Contact Fatigue Tester," ASTM STP 711, 1982, pp. 107-124.

48. S. M. Kulkarni, M.S. Dissertation, Vanderbilt University, 1986.

49. H. K. Lorosch, "Influence of Load on the Magnitude of the Life Exponent for Roller Bearings," ASTM STP 771, 1982, pp. 275-292.

50. Q. Chen, G. T. Hahn, C. A. Rubin and V. Bhargava, "The Driving Force for Rolling Contact Induced, Mode II, Cyclic Crack Growth in High Strength Bearing Steels," to be published.